APPLICATION OF LAND-BASED CONTROLLED SOURCE EM METHOD TO HYDRAULIC FRACTURE MONITORING

A Dissertation

by

MARK STEVEN HICKEY

Submitted to the Office of Graduate and Professional Studies of
Texas A&M University
in partial fulfillment of the requirements for the degree of

DOCTOR OF PHILOSOPHY

Chair of Committee,	Mark Everett
Committee Members,	Richard Gibson
	David Sparks
	Igor Lyuksyutov
Head of Department,	Julie Newman

December 2019

Major Subject: Geophysics

ABSTRACT

Hydraulic fracturing allows improved hydrocarbon production in low permeability formations. Imaging the distribution of fluid used to create a hydraulic fracture can aid in the characterization of fracture properties such as extent of fluid penetration as well as fracture azimuth and symmetry. This could contribute to improving the efficiency of an operation, for example, in helping to determine ideal well spacing or the need to refracture a zone. A ground-based controlled-source electromagnetics (CSEM) technique shows promise for imaging the fluid due to the change in field caused by the difference in the conductive properties of the fluid when compared to the background. With sufficient advances in high signal to noise recording equipment, coupled with a high-power, broadband transmitter one could potentially detect hydraulic fracture extent and azimuth with minimal processing. In this study, a 3D finite element code is used to model the complete well casing along with the layered subsurface. The forward modeling is used to optimize survey designs and identify the band of frequencies that best capture the desired subsurface response. In the field, the results of the modeling are also used to create a custom pseudorandom numeric (PRN) code to control the frequency content of transmission through a grounded dipole source. Receivers record the surface voltage across two grounded dipoles, one parallel and one perpendicular to the transmitter. The data are presented as the displays of amplitude ratios across several frequencies at the various receiver locations. I show field results in multiple basins in the United States along with the CSEM theory used to create the survey designs.

Interpretations of CSEM responses in terms of subsurface changes in electrical conductivity presented in this dissertation are regarded as tentative awaiting further tests from detailed numerical simulations and a better understanding of noise. Oilfield operations are exceedingly complex systems and the CSEM technology for hydraulic fracture monitoring, while showing promise, is still under development.

DEDICATION

For Zach & Hannah

ACKNOWLEDGEMENTS

I would like to thank Dr. Mark Everett and the rest of my committee for their extreme patience and wonderful guidance.

I would also like to thank Deep Imaging for the ability to apply CSEM in real world situations, no matter how grueling, and for the data used in completing this study.

CONTRIBUTORS AND FUNDING SOURCES

Contributors

This work was supervised by a dissertation committee consisting of Dr. Mark Everett, Dr. David Sparks, and Dr. Richard Gibson of the Department of Geology & Geophysics and Dr. Igor Lyuksyutov of the Department of Physics & Astronomy.

Derivation and initial programing of the grounded dipole source for modeling data provided in Chapter II was provided by Dr. Stephan Helwig. Derivation and programing for the grounded dipole source used for modeling results in Chapters III, IV, and V were done at my direction and under my supervision by Dr. Santiago Trevino III.

All other work conducted for the dissertation was completed by the student independently.

Funding Sources

None.

TABLE OF CONTENTS

Page

LIST OF FIGURES

Page

CHAPTER I

INTRODUCTION

The geological interpretation of exploration geophysics data can be a costly and time-consuming process. New algorithms that enhance the reliability of the process, the resolution of the subsurface images, or lower the cost or time are advantageous. Electromagnetic (EM) methods can be added to an exploration geophysical program to enhance interpretation, or can be used as a stand-alone reconnaissance tool, or can be used to determine an appropriate amount of resources to allocate to a prospect. EM exploration, using either a controlled source or a natural source such as in magnetotellurics, is a non-invasive technique widely used for characterizing mineral resources, groundwater, and oil and gas reservoirs. EM exploration requires a contrast between the electrical conductivity of the target and that of the surrounding medium. The sensitivity of the recording equipment and the methods used for processing of the noisy data help to determine the minimum required conductivity contrast at the exploration depth.

Forward modeling has been developed to use known parameters describing the subsurface geoelectrical structure, along with the governing physics connecting the source with the receiver response, to predict the results of a planned exploration geophysics project. Using forward modeling allows the interpretation of likely results to be made prior to conducting fieldwork. Forward modeling also allows one to vary the geoelectrical parameters of the subsurface until the modeled responses closely match the

acquired field data. Simple forward modeling permits variation of geoelectrical parameters in one dimension (1D), such as layer electrical conductivities and thicknesses, but more complex modeling software allows for parameter variations in multiple spatial dimensions. Forward modeling approaches take advantage of advances in computational science procedures such as parallelization, memory management, and cloud computing. Using a three dimensional (3D) forward modeling approach allows inclusion of various infrastructure commonly found in oil fields, since the EM response is susceptible, for example, to metal wellbore casing.

There is no immediate use for a new tool if there is no viable way to apply it. As already mentioned, EM exploration requires a significant electrical conductivity contrast between the target and the surrounding medium. One application for which controlled source electromagnetics (CSEM) has made an important contribution is hydrocarbon exploration. CSEM is currently used offshore for hydrocarbon reservoir characterization. It is of interest to transfer some of the concepts and successes of marine CSEM to reservoir characterization in a land-based setting. An emerging, not yet proven, application for terrestrial CSEM is hydraulic fracturing monitoring. Since hydraulic fracturing involves injecting water into a source rock, the apparent conductivity of the fractured volume will change over time. If sensitive enough, and if noise levels are sufficiently low, the field data from a CSEM survey should show variations in signal due to the changing conductivity of the injection volume. The field responses could then be interpreted directly in a qualitative sense, without forward modeling, or used with an

inversion program to generate a subsurface model that images the resulting fracture extent.

My research applies surface-based terrestrial CSEM to an investigation of hydraulic fracture monitoring. Since the well completion process changes the subsurface physical properties over time, the resulting CSEM response should also change over time. Where signal-to-noise ratio permits, this would allow each “frac” stage to be monitored in time steps. The resulting change in signal would then be diagnostic of the change in fracture complexity due to the injection of the hydraulic fracturing fluid. In particular, the change in signal may be interpreted as the change in the complex fluid network geometry. This allows the geophysicist to calculate vital metrics such as final frac half-length, asymmetry, and azimuth. These metrics would be given to the well completion engineer for critical decision making. The decisions can influence well spacing, stage spacing, pump times, and many other engineering parameters that affect the total cost of a hydraulic fracture operation.

EM geophysical exploration utilizes different methods depending on the target. Natural sources can be used for deep exploration within the Earth's crust. In shallower applications, the controlled-source EM (CSEM) method deploys an active source which produces a known primary electromagnetic field. A secondary field is generated by the diffusion of eddy currents into the subsurface in response to time variations in the primary field (Nabighian, 1988). In the frequency domain, the source current oscillates in time at a fixed angular frequency. A receiver measures the amplitude and phase of the response from the subsurface at that frequency. For the transient case, the source is

energized by a time-varying current, typically characterized by a slow rise followed by a rapid cut-off. A receiver measures the time-averaged response at the centers of a set of logarithmically-spaced time windows, or gates. Placement of the receiver enables measurement of different aspects of the secondary field. The source-receiver distance can be fixed with respect to the transmitter or a variable source-receiver offset can be utilized. An overview of the CSEM exploration technique with an emphasis on water resource investigations is provided by Everett and Meju (2005).

CSEM can be divided into two source modes, galvanic and inductive. The galvanic mode is characterized by electric currents that are forced to flow vertically across resistive layer interfaces. The inductive mode is generated by the mutual inductance between the transmitter and the subsurface. The induced currents flow largely in horizontal planes in that case. A loop source is a purely inductive source that creates a signal by changing the current in the loop. A grounded electric dipole generates both galvanic and inductive modes.

An essential requirement for proper interpretation is the implementation of an accurate forward modeling algorithm that computes the CSEM response of a given subsurface conductivity distribution. Forward modeling in EM has traditionally favored three techniques: finite difference (FD), finite element (FE), and integral equation (IE). The three methods have strengths and weaknesses, as reviewed by Avdeev (2005). For example, a staggered-grid finite difference technique (Mackie et al., 1988) has been used in magnetotellurics.

My method for CSEM-3D interpretation requires a forward algorithm that can accurately compute the induction response for arbitrary (loop or grounded dipole) source excitation of an arbitrary 3D subsurface. An FE code using an unstructured mesh that conforms to rugged topography and complex subsurface structure is ideal. For the forward calculations I use a code first developed by Badea et al. (2001) for a borehole logging application in cylindrical coordinates. The code was later modified (Stalnaker et al., 2006) to Cartesian coordinates and incorporated simple topography.

Some forward calculations used to characterize subsurface geological structures, such as the one used to explore heterogeneity in aquiferous fractured rocks by Sasaki & Meju (2006), are based on a frequency-domain FD technique to determine the response of a 2D subsurface. The combination of 3D source excitation of a 2D subsurface structure is termed a 2.5D problem. The source used by Sasaki and Meju (2006) was a horizontal loop-loop system (HLEM) at fixed transmitter-receiver offset operating at a definite frequency or set of frequencies.

Haber et al. (2002) used the finite volume (FV) method, a variant of the FD method, to solve for Coulomb-gauged potentials in their 3D CSEM frequency-domain CSEM algorithm.

A recent review of land-based CSEM applications (Streich, 2016) explains the history and challenges of land-based CSEM and its application to the oil and gas industry. A review of computational methods for CSEM (Newman, 2014) highlights recent computational methods for EM including modeling, inversion and high-performance computing. Another overview paper (Constable, 2016) covers natural

source methods. Natural sources are important to my study since they contribute one of the sources of noise in CSEM data. A review paper specifically covers hydraulic fracture monitoring (Thiel, 2017) with a focus on geothermal applications and MT exploration methods. An in-depth review of 3D inversion in practice is provided by Miensopust (2017). The comprehensive paper covers specific topics from data acquisition and preparation to mesh design.

In order to place into historical context the use of CSEM for hydraulic fracture monitoring, a brief review of the background of completion operations is provided here. Commercial hydraulic fracturing started in 1949 when Halliburton Oil Well Cementing Company (Howco) performed the first two commercial fracturing treatments using a blend of crude oil, gasoline, and sand (Montgomery & Smith, 2010). The main objectives for using hydraulic fracturing are to increase the productivity or injectivity of a well (Lake et al., 2007). Hydraulic fracturing pumps a fluid into a formation at a pressure that exceeds the strength of the formation causing the formation to fracture. These new fractures can connect with previous natural fractures, thereby increasing the permeability. The combination of horizontal drilling with hydraulic fracturing helped start the “shale boom”. An example of a single well hydraulic fracturing operation can be seen in figure 1.

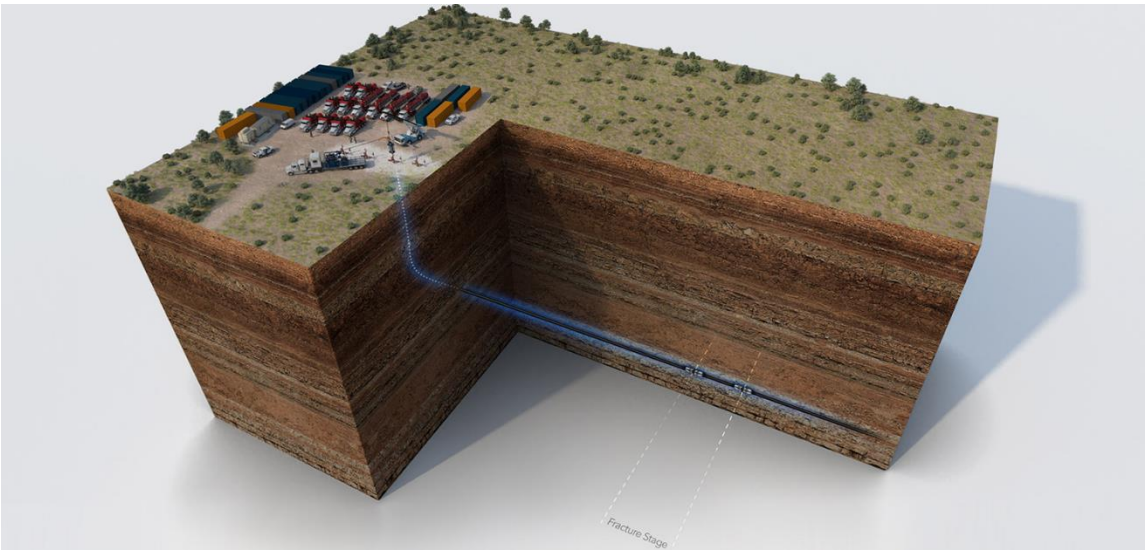

Figure I-1 Typical horizontal hydraulic fracture operation (Not to scale). A fracture stage is labeled.

Chapters 2-5 of this dissertation are based on a series of papers that I have presented at SEG (Society of Exploration Geophysicists) and SPE (Society of Petroleum Engineers) conferences attended by oil and gas professionals as well as academic geophysicists. The following is a brief synopsis of these publications, for which I was the primary author, including a discussion of my primary scientific input and the potential significance of the results. There is some overlap in chapters 3 and 4 due to the different intended audiences of the papers. Chapter 3 was written to be more informative to engineers and persons responsible for making decisions in a hydraulic fracturing operation. It focuses more on CSEM as it applies to hydraulic fracturing operations and is intended to give engineers insight into how they can apply CEM in their own operations. Scientists are the primary audience for chapter 4 and are expected to have a better understanding of the signal response on the surface after reading. It must be

carefully noted that all of the interpretations of CSEM responses presented in this dissertation should be regarded as tentative as they have not yet been supported by detailed numerical simulations and that the effects of noise not related to subsurface changes in electrical conductivity have not been fully quantified. Once improved numerical simulations and a better understanding of noise are available, the capabilities of terrestrial CSEM to image fluid distributions at depth will become much better understood than at the present time. Some background information about PRBS signal analysis, fracture network geometries, and oilfield electromagnetic noise are provided in Appendices A,B and C respectively.

In Hickey et al (2010), some critical aspects concerning the adaptation of the marine CSEM method to land are investigated. One important factor to consider is the effect of topography. It is uncertain how rough terrain affects terrestrial CSEM responses. An additional problem is the lack of visualization tools to explore CSEM responses in order to qualitatively interpret forward modeling results. These problems are important because topographic effects could be misinterpreted as being caused by subsurface bodies, in which case the interpretation of the secondary response will be incorrect. Further, an intuitive visualization of the CSEM response allows for better qualitative interpretations. I solved these problems by adapting the CSEM forward modeling code described in Stalnaker et al. (2006) to include irregular topography. Dr. Stephan Helwig helped me adapt the FE modeling algorithm for common terrestrial CSEM layouts by supplying a forward code for the analytic solution of long-dipole excitation of a layered Earth. I then created subroutines to output the secondary

responses from irregular terrain overlying 3D structures at depth. I also adapted the new code to output files in the visualization tool kit (VTK) format. This allows the use of 3D graphics applications such as ParaView to visualize and manipulate the structure and the response. I found that the response of the topography changes with the type of source used. Depending on the source-receiver offset and geometry of the topographic anomaly, I concluded that topographic effects should be taken into account, otherwise the interpretation of field data could be incorrect. In the oil and gas industry, an incorrect interpretation can lead to extensive economic losses. Future work should be to include hydrocarbon targets along with actual digital elevation models and to determine the relative error on CSEM responses introduced by not including the topography. This should be done for different production basins of interest. Simulations should also be developed to further investigate topography effects for scenarios wherein the source is deployed directly on top of a topographic anomaly.

In Hickey et al (2015) I address these two questions: Where does the injected fluid go during a hydraulic fracture operation? Can fluid migration at depth during a stage of a hydraulic fracturing operation be monitored and imaged? Imaging the fluid migration into the geological formation during a hydraulic fracturing operation would provide physical insight that should allow better engineering designs for well placement and frac operations. Optimizing frac operations increases profitability of the field. To monitor and image subsurface fluids, the CSEM hardware used during the hydraulic fracture operation must have sufficient sensitivity. Since the source of the primary field is a grounded dipole, the analytic solution for such a source in a conductive half space

was derived and coded, at my direction, by Santiago Trevino III. We debugged the code together and ran tests against published analytical results. I then designed a layout that optimized the inductive coupling of the surface-based transmitter to a lateral wellbore casing within a target shale formation, and used the parameters from available receiver equipment to simulate the total response that should be recorded during an actual experiment. I applied this design to analyze two case studies. The modeling results show however a much broader secondary field response than those that were observed in the field, i.e. the spatial localization of the secondary response is much greater in the field data. The modeling results do indicate a signal response across a large frequency bandwidth, wherein certain frequencies display a larger secondary response. This effect is also seen in the field data. The field data further show that as the hydraulic fracture operation adds more fluid under pressure to the formation, changes in the CSEM responses appear to correlate with the stage location along the lateral wellbore. The results of this study identify a preferred frequency bandwidth that depends on the well casing design, geology, and depth. It also indicates that terrestrial CSEM could become a viable tool for hydraulic fracture monitoring. In future, data from more stages should be gathered and compared with the results found at the two field sites considered here. Data from more petroleum-bearing sedimentary basins should be included for further study. Since the field data are analyzed in terms of an amplitude ratio, further study should investigate information contained in the phase data. Also, there should be an optimization of the field design so that, for example, any deleterious effects on the CSEM response of the large spatial gradients in the primary field near the dipole

grounding points can be taken into account. The forward modeling code should also be improved to include the vertical portion of the well casing.

Further analysis of terrestrial CSEM responses for purposes of hydraulic fracture monitoring was investigated in Hickey et al (2015b). It is desired that forward-modeled responses using CSEM with a grounded dipole at the surface should match, within tolerance, the field data recorded during hydraulic fracture monitoring. Further, the field equipment should be sensitive enough to record signals due to subsurface fluid migration. In addition, signals levels must rise above the noise level. The transmitted signal should be designed to optimize the secondary signal response due to fluid-induced conductivity changes at depth. These considerations are important to ensure the highest possible signal to noise ratio. Since the source of the transmitted signal is a grounded dipole, the analytic solution of a grounded electric dipole in a conductive half space is again used. I used formulas found in Ward & Hohmann(1974) as the starting point for the derivations. The modeling results indicated that the strength of the secondary returned signal lies within the sensitivity of typical field systems that are currently available. These findings are important because, as shown in an accompanying case study, it is possible that fracture extent could be imaged, provided the signal can be properly discriminated from noise. Fracture extent is the type of subsurface information that could be used to optimize future well completion operations. Additional projects should focus on improving the forward modeling code to provide higher-resolution discretization of the subsurface geoelectric structure.

In Hickey et al (2017) the following scientific question is addressed: for a given geological formation, well type, and lateral wellbore depth, where does the injected fluid migrate during a hydraulic fracturing operation? It is envisioned that optimized well spacing and well completion techniques can be applied with the additional information provided by terrestrial CSEM constraints. Using surface-based CSEM, in this paper images are created of the signal response acquired during intervals in which there is a change of the conductivity distribution at depth due to the injection of fracturing fluids. I first modeled the expected response of a given field layout in order to gain insight into the ideal frequency bandwidth required for subsurface fluid imaging. This permits a first design of the survey layout. Then, I processed the data and imaged the extracted information from field data at two sedimentary basins. In the Anadarko basin, subject to the proviso that the signal rises above the noise level which cannot be ascertained with surety (see Appendix C), the CSEM responses appear to indicate that the azimuth of the fluid migration pathway changed as the frac stages progressed towards the heel end of the well. The heel end is the end closest to the vertical well section while the toe end is the end farthest from the vertical section. However, as noted above, forward modeling suggests broader-scale anomalies than those found in the field data. In the Delaware Basin, involving a vertical wellbore, I made two primary discoveries. First, the electronic noise detected by the receivers from the oilfield operations on the pad is too large to allow for subsurface-diagnostic data to be recorded there. Second, due the high porosity, and hence high electrical resistivity, of the carbonate formation being treated, the size of the receiver array for monitoring these operations should be increased beyond

the original layout. The results at Anadarko basin are important because they probe conditions under which stress shadowing may be taking place which, if further substantiated by additional data, would allow operators to design well completions to mitigate its effects. The information from the vertical well case study will help future CSEM array designs for operations using these types of wells in carbonate geology. The next steps should explore further improvements to mitigate electromagnetic noise in the field and to quantitatively estimate the change in conductivity due to the filling of fractures with conductive fluid.

CHAPTER II

THE EFFECTS OF ROUGH TERRAIN ON LAND-BASED CONTROLLED-SOURCE ELECTROMAGNETIC EXPLORATION USING A LONG HORIZONTAL DIPOLE SOURCE*

Controlled source electromagnetics (CSEM) is an important tool for hydrocarbon exploration. It is of significant economic interest to transfer some of the concepts and recent successes of marine CSEM to a land-based setting. However, modeling CSEM responses with a grounded source on land requires several adaptations to existing software. The long-term purpose of our work is to develop a reliable forward model for land-based controlled-source electromagnetics which can be used to explore deep resistive hydrocarbon reservoirs in potentially rugged terrain in the presence of oilfield infrastructure and other cultural noise. At the current stage of development, we have adapted an existing finite element algorithm to calculate responses to long dipole excitation of a conducting subsurface with rough topography.

Introduction

Recent fundamental work in offshore petroleum exploration geophysics has demonstrated a sensitivity of marine CSEM data to the presence of deep hydrocarbon reservoir fluids (Sinha, 1999; Edwards, 2005; Constable and Srnka, 2007; Chave 2009). A grounded horizontal electric dipole (HED) source is typically towed by a ship over a

* Part of this chapter is modified with permission from "The Effects of Rough Terrain on Land-Based Controlled-Source Electromagnetic Exploration Using a Long Horizontal Dipole Source" by Hickey, M. S., Everett, M. E., Helwig, S. L., & Mogilatov, V. S., 2015. SEG Technical Program Expanded Abstracts, 2010, pp. 3914-3918, Copyright [2010] by Society of Exploration Geophysicists.

known or putative hydrocarbon reservoir in order to excite it with a strong galvanic mode. This mode is characterized by vertical electric currents that are forced to flow across the resistive layer interfaces. The complementary inductive mode, also generated by an HED source, provides valuable further constraints on the background geoelectrical structure. The dual—mode marine CSEM response provides information to the explorationist which can reduce the uncertainty of estimates of hydrocarbon saturation within a pay zone.

Herein we have adapted CSEM forward modeling software previously presented by Badea et al. (2001) and Stalnaker et al. (2006) to compute the response of topography excited by a land—based controlled electromagnetic source. This is done to help evaluate the utility of terrestrial CSEM for characterizing deep hydrocarbon reservoirs located beneath potentially rugged terrain. To demonstrate our capabilities, we have modeled the response of a single 60 m high topographic pedestal due to two different sources: a loop source and a horizontal grounded dipole source. Responses are calculated for different pedestal offsets relative to the source location.

The calculations are based on a finite element method that solves for Coulomb—gauged scalar and vector potentials at each node of an unstructured tetrahedral mesh (Badea et al., 2001; Stalnaker et al., 2006). Since our goal is the secondary response due to a target in a known background, we solve for the secondary Coulomb—gauged scalar and vector potentials. The governing Maxwell equations expressed in terms of secondary potentials $(\boldsymbol{A}_S, \psi_S)$ are:

(1) $\boldsymbol{\nabla}^2 \boldsymbol{A}_S + i\omega\mu_0\sigma(\boldsymbol{r})(\boldsymbol{A}_S + \boldsymbol{\nabla}\psi_S) = -\mu_0\Delta\sigma\boldsymbol{E}_P;$

(2) $i\omega\mu_0\boldsymbol{\nabla}\cdot[\,\sigma(\boldsymbol{r})(\boldsymbol{A}_S + \boldsymbol{\nabla}\psi_S)] = -\boldsymbol{\nabla}\cdot\mu_0\Delta\sigma\boldsymbol{E}_P;$

where $\Delta\sigma = \sigma(\boldsymbol{r}) - \sigma_P$is the difference between a background conductivity model σ_P and the 3—D conductivity distribution $\sigma(\boldsymbol{r})$ whose CSEM response is required. The vector field $\boldsymbol{E}_P$ is the known CSEM response of the background conductivity σ_P and appears as a source term on the right—side of equations (1) and (2). The frequency is ω and the magnetic permeability of free space is μ_0. Equation (1) is the vector electromagnetic diffusion equation while equation (2) is a statement of divergence—free current density, $\nabla\cdot\boldsymbol{J} = 0$. The finite element system of equations generated by discretizing the weak formulation of (1) and (2) is solved using the quasi-minimal residual method (QMR) described by Freund (1992). A more in-depth derivation of the central equations can be found in appendix D.

Finite element analysis has an advantage over more widely—used finite difference modeling in that it permits use of an unstructured mesh, at the cost of increased programming complexity. Unstructured meshing allows the solution domain to be discretized more finely in localized regions of interest such as sharp conductivity interfaces and near the source. Additional nodes can also be added according to a posteriori error estimation, as demonstrated for 2—D plane—wave excitation by Key and Weiss (2006).

An unstructured mesh also enables the topography of the survey area to be accurately modeled. The mesh generation algorithm we use was originally based on a

cylindrical well—logging geometry, as explained in Badea et al. (2001); herein the same strategy is adopted except with an underlying rectangular mesh geometry.

The sources used in this work are a conventional loop source of finite radius and a grounded dipole source of finite length. The loop source is of limited value for hydrocarbon exploration since in a layered medium it generates only the inductive mode consisting of horizontal loops of current. A resistive hydrocarbon—bearing layer is likely to be poorly flux—linked to the surrounding, conductive strata and hence generates a weak inductive—mode response. The grounded dipole source is of greater importance since it generates the galvanic mode which is more sensitive to the presence and the resistivity of resistive layers (e.g. Passalacqua, 1983) The primary field EP for both sources is taken to be the analytic response of a conductive half space (Ward and Hohmann, 1988).

Once the secondary potentials $(\boldsymbol{A}_S, \psi_S)$ are computed by finite element analysis, the secondary electromagnetic field vectors $(\boldsymbol{E}_S, \boldsymbol{B}_S)$ defined by

$$\boldsymbol{B}_S = \boldsymbol{\nabla} \times \boldsymbol{A}_S; \tag{3}$$

$$\boldsymbol{E}_S = i\omega(\boldsymbol{A}_S + \boldsymbol{\nabla}\psi_S); \tag{4}$$

are found in a post—processing step using the moving least squares interpolation (MLSI) approach of Tabbara (1994). MLSI is used for numerical differentiation but it contains smoothing characteristics and consequently its accuracy will degrade in the vicinity of sharp conductivity contrasts such as the air—Earth interface. Therefore the

numerical differentiation of the secondary potentials $(\boldsymbol{A}_S, \psi_S)$ is performed using only those nodes located wholly inside the Earth or within the air layer, depending on which of these two regions the field $(\boldsymbol{E}_S, \boldsymbol{B}_S)$ is being evaluated. For calculation of $(\boldsymbol{E}_S, \boldsymbol{B}_S)$ on the air—Earth interface, the average of the MLSI interpolants in each region is used. Numerical differentiation using this partitioned MLSI scheme is easier to perform on an irregular mesh than are conventional difference approximations of spatial derivatives. Both methods yield similar accuracy at the air—Earth interface on a rectilinear mesh.

Method

The finite element analysis of land—based CSEM is broken down into several steps: model specification; mesh generation including topographic adjustment; matrix and source vector assembly; solution of the linear system for the Coulomb-gauge secondary potentials; post processing to obtain the secondary electromagnetic field components; graphical output.

The topographic modeling capabilities of our FE approach are quite general inasmuch as a digital terrain map of the survey area is readily incorporated into the mesh generation algorithm. However, a limitation of the present version of the software is that the source is required to be located on flat terrain since the derivation of the source term does not consider any vertical components. Calculations for multi-component sources like those needed to represent sources not on flat topography are non-trivial and outside the scope of the current study. Receivers are permitted to be located in areas of rugged terrain.

The input terrain map may be defined on a denser, or a sparser, set of points than the air—Earth interface nodes of the original mesh prior to topographic adjustment or local refinement. In the adjustment procedure, each surface node is shifted upward or downward to the average of the elevation values of all terrain points located within a certain radius of the surface node.

In areas of high topographic relief, if the vertical shifting of the surface node would result in a tangling of the mesh, the node closest in elevation to the terrain point becomes a new surface node and it is shifted to the terrain elevation. Every node directly above the new surface node is labeled as an air node while every node directly below it is labeled as a subsurface node.

In the case of a sparsely sampled terrain file, those surface nodes which do not enclose a terrain point within the specified radius are shifted up or down to the average elevation of the surrounding, shifted nodes.

After all nodes have been shifted and labeled as air, surface or subsurface, the topographic adjustment procedure is complete. The conductivity of the mesh tetrahedra are then assigned to air or subsurface values as appropriate.

For this paper we demonstrate CSEM finite element analysis using a loop source and a grounded dipole source for a steep—sloped, but otherwise simple terrain variation. The model is a pedestal—like protrusion that projects above the air—Earth interface with height 60 m and widths 20 m in the x direction and 50 m in the y direction. To explore how such terrain variations can shape the CSEM response, finite element analysis is performed as the pedestal is systematically moved along the x—axis from its

nominal location centered on (x,y)=(110,0) m toward or away from the source located at the coordinate origin.

Along with the numerical values of the complex field components, a Visualization Toolkit (VTK) graphic file is also output which is used with the Paraview freeware package to visualize **H** field vector streamlines in three dimensions.

Results

For this paper, the secondary conductivity $\Delta\sigma$ is defined as the change in conductivity, with respect to a double—half space background model with perfectly flat terrain, that is generated by the pedestal—like terrain variation. The governing equations (1) and (2) are solved for each type of primary excitation, i.e. the finite—radius loop and the long-grounded dipole. The topographic pedestal acts as a secondary electromagnetic source which generates the secondary scalar and vector potentials on every node in the mesh. The electrical conductivity of the terrain and the underlying subsurface is set to σ_P=0.03 S/m. The frequency f=$\omega/2\pi$ is 3 kHz. The mesh is composed of 60 x 61 x 61 nodes and the dimensions of the solution domain are 0.6 km in all three directions. The dipole moments of the loop and the long dipole source are IA [$A \cdot m^2$] and IL [$A \cdot m$], respectively, where A is the area of the loop and L is the length of the grounded dipole. The loop radius is 5 m and the dipole length is 10 m. Although the dipole length and model size are unrealistic for hydrocarbon exploration, these values are scalable up or down to any size needed. After computation, the field amplitudes are scaled, in each case, by the appropriate dipole moment.

Figures 1—4 show streamlines of the complex secondary vector magnetic field $\mathbf{H}_S$ that is generated by the interaction of the primary sources with the pedestal terrain variation. The divergence of the streamlines clearly reveal that the pedestal behaves as a secondary source of electromagnetic field for both types of source.

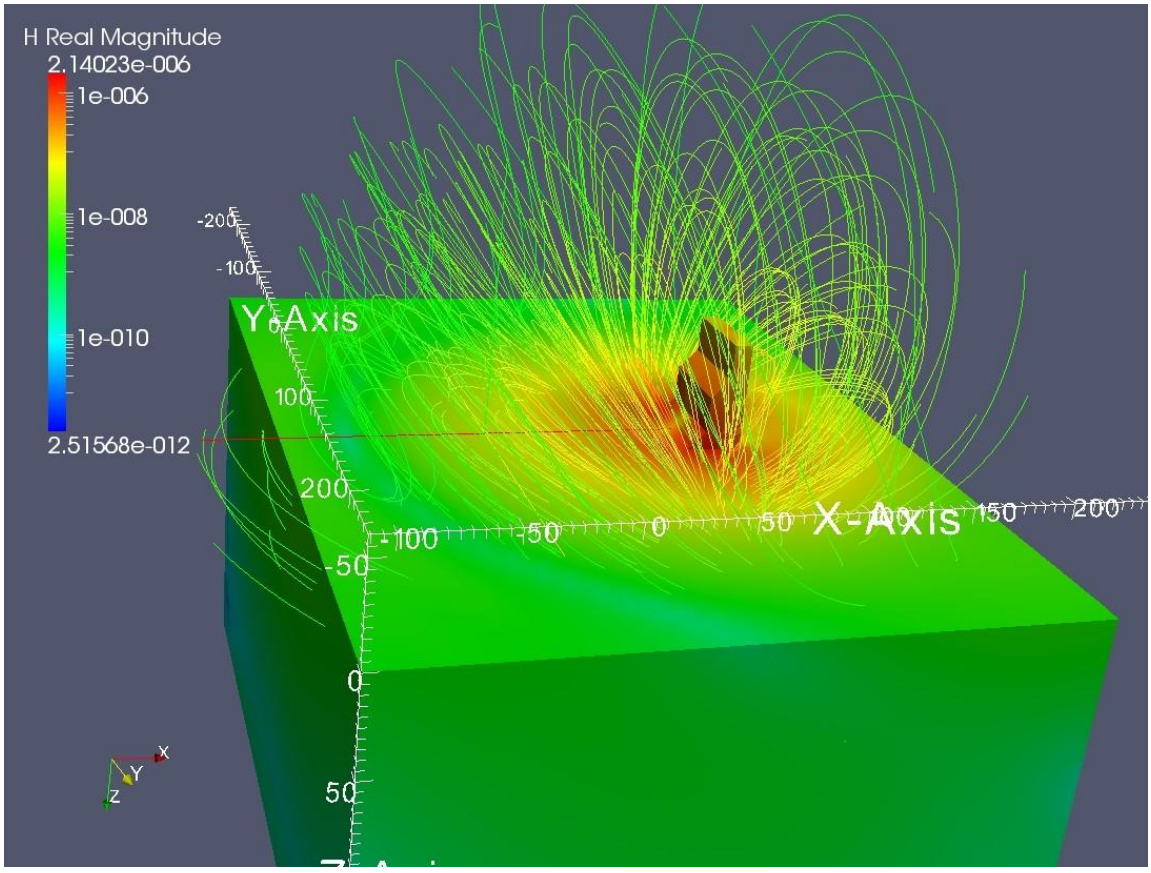

Figure II-1 3—D streamlines of the real part of the secondary $\mathbf{H}_S$ field with the x—directed grounded long dipole source located at the coordinate origin. Amplitudes |Re $\mathbf{H}_S$| [T] are contoured on the air—Earth interface z=0. Reprinted with permission from Hickey et al. (2010).

The magnetic streamlines shown in Figures 1 and 2 resemble those of a horizontal magnetic dipole located within the pedestal and oriented in the y—direction. The pattern is therefore consistent with vertical electric current loops circulating inside the pedestal in the x/z—plane. The primary excitation in this case is the long dipole source which excites a strong galvanic mode containing vertical current flow in the subsurface, as mentioned earlier. In this way, the streamline and contour patterns in Figures 1 and 2 can be understood qualitatively.

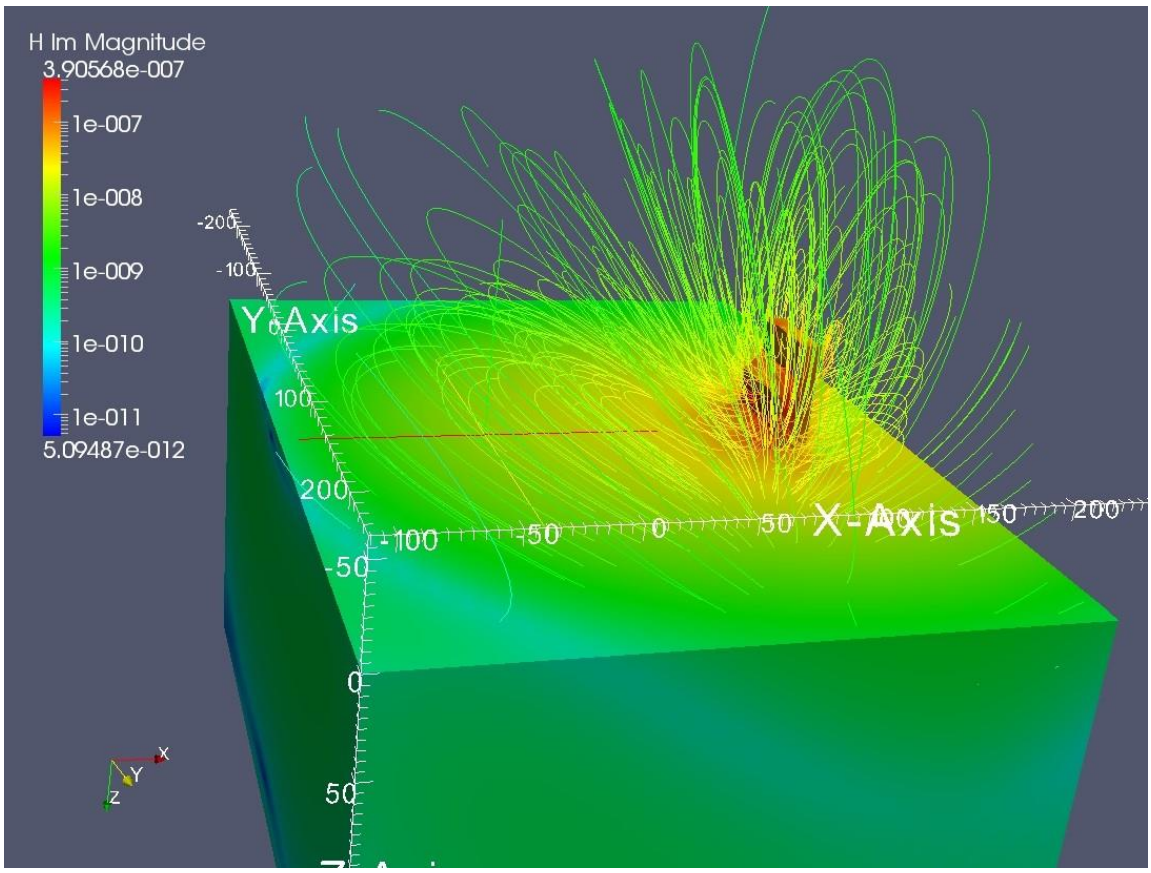

Figure II-2 3—D streamlines of the imaginary part of the secondary $\mathbf{H}_S$ field with the x—directed grounded long dipole source located at the coordinate origin. Amplitudes $|\text{Im } \mathbf{H}_S|$ [T] are contoured on the air—Earth interface z=0. Reprinted with permission from Hickey et al. (2010).

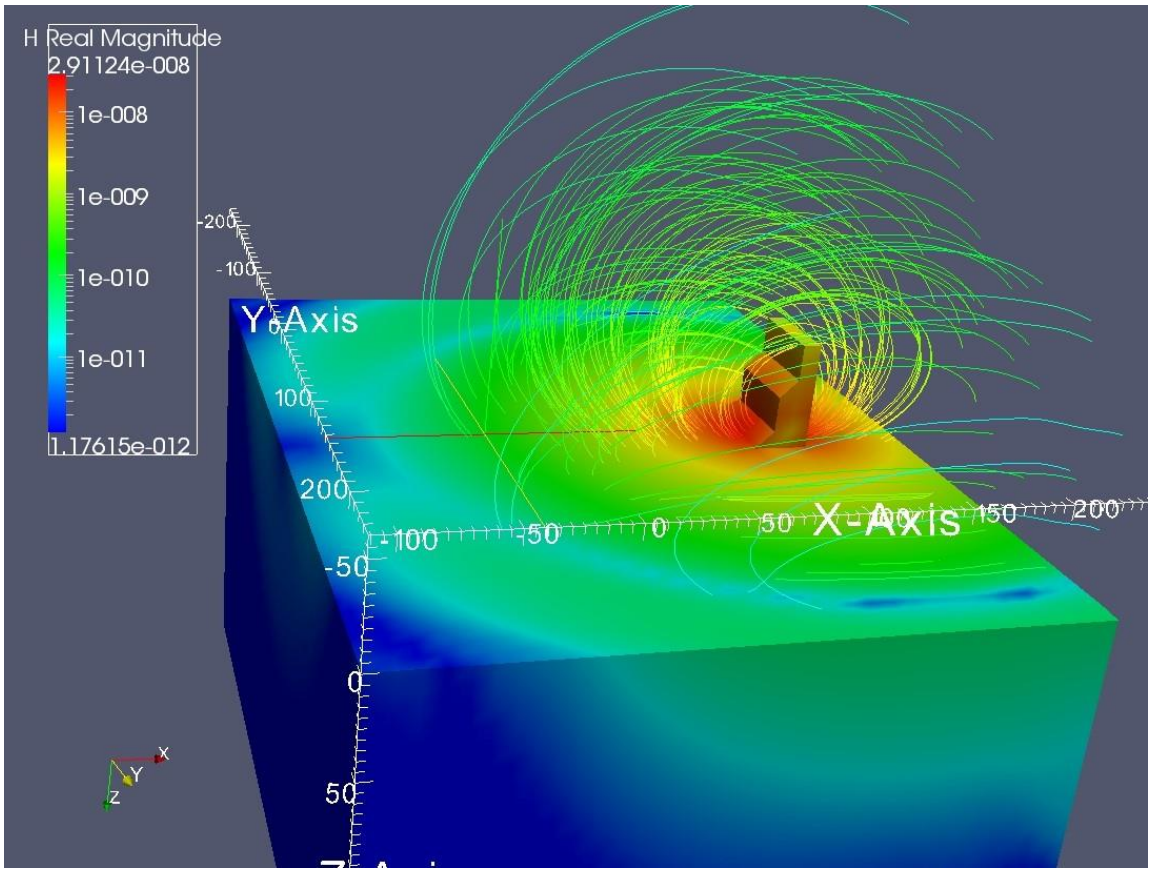

Figure II-3 3—D streamlines of the real part of the secondary $\mathbf{H}_S$ field with the finite—sized horizontal loop source located at the coordinate origin. Amplitudes $|\mathrm{Re}\ \mathbf{H}_S|$ [T] are contoured on the air—Earth interface z=0. Reprinted with permission from Hickey et al. (2010).

The magnetic streamlines shown in Figures 3 and 4 resemble those of a vertical magnetic dipole located within the pedestal with is axis in the z—direction. The pattern is therefore consistent with horizontal electric current loops circulating inside the pedestal. The primary excitation in this case is the finite—radius loop source which excites a strong mode consisting of horizontal current flow in the subsurface, as mentioned earlier. In this way, the streamline and contour patterns in Figures 3 and 4 can

be understood qualitatively.

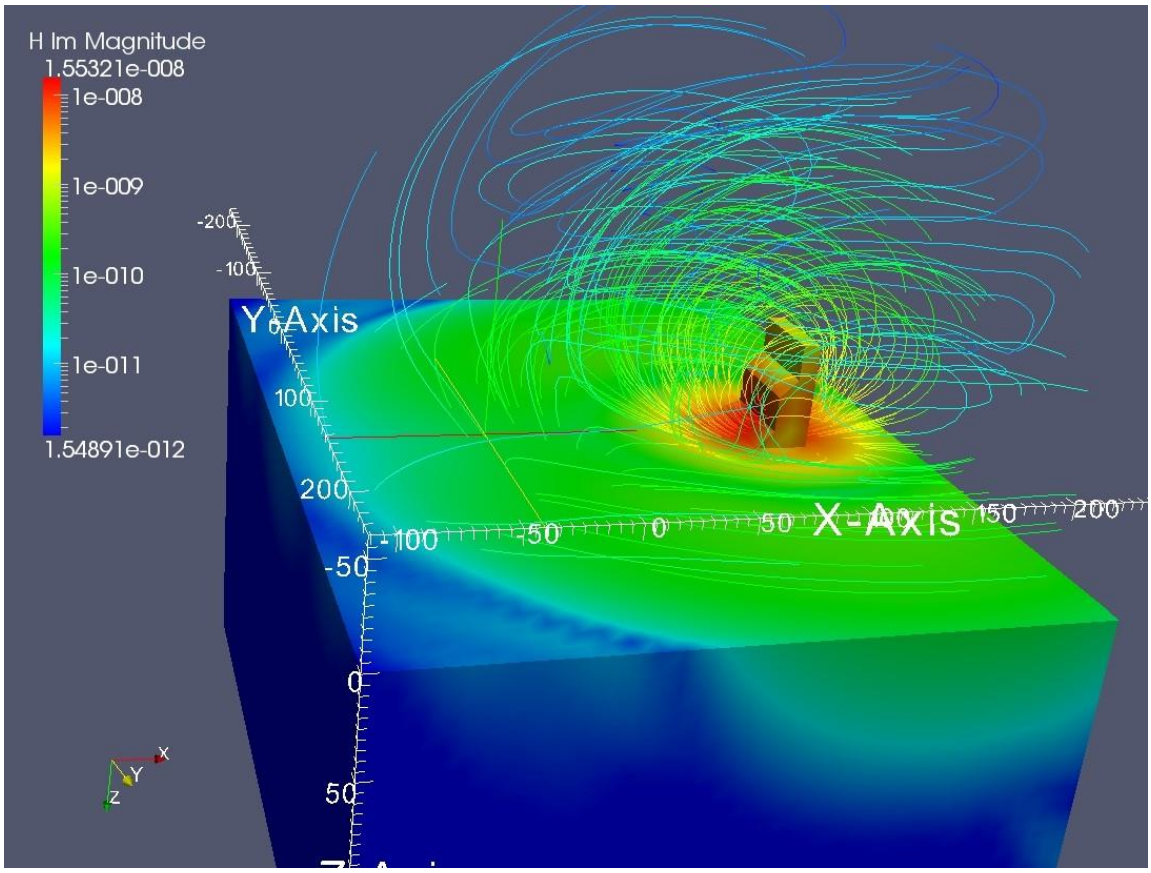

Figure II-4 3—D streamlines of the imaginary part of the secondary $\mathbf{H}_S$ field with the finite—sized horizontal loop source located at the coordinate origin. Amplitudes |Im $\mathbf{H}_S$| [T] are contoured on the air—Earth interface z=0. Reprinted with permission from Hickey et al. (2010).

The output of the CSEM finite element analysis includes all five significant complex, secondary electromagnetic field components, E_x, E_y, H_x, H_y, and Hz evaluated on all nodes of the mesh. The component E_z=0 on the air—Earth interface where measurements are likely to be made, so this component is not computed in the post—

processing stage.

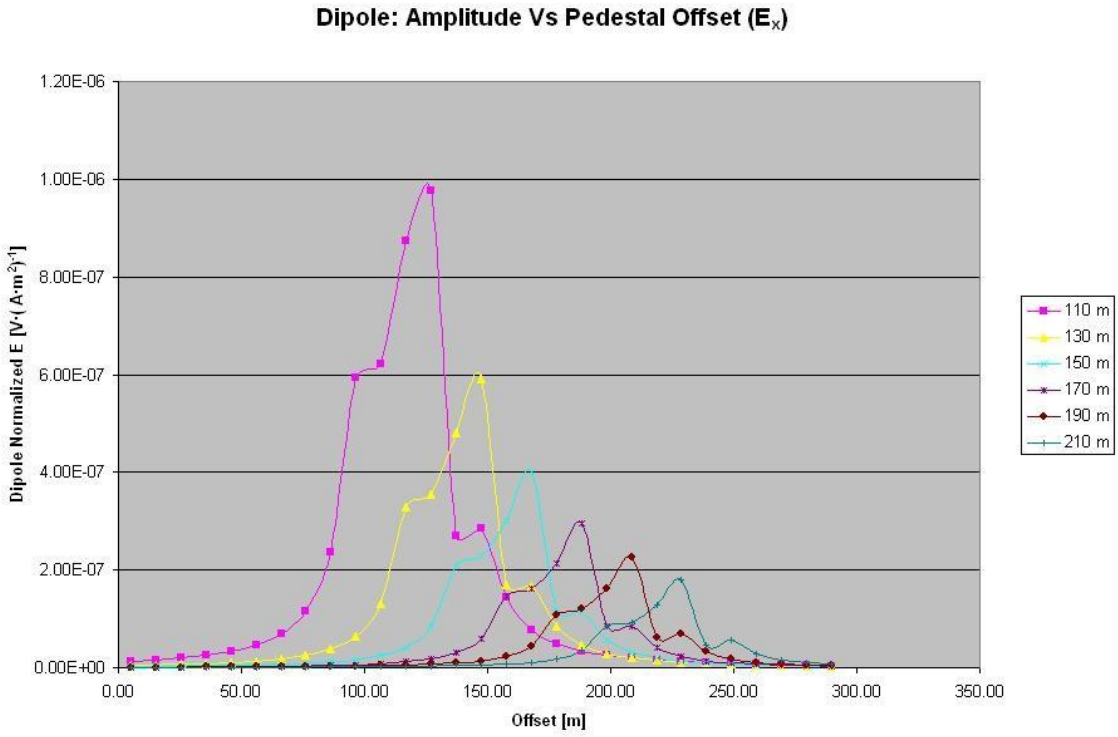

Figure II-5 The amplitude of secondary electric field $|E_x|$ as a function of distance from the long dipole source. The various curves are for different pedestal locations from x=110 m to x=200 m, as indicated in the legend. Reprinted with permission from Hickey et al. (2010).

As an early demonstration of the software, the effects of varying the position along the x—axis of the topographic pedestal on the $|E_x|$ CSEM response components are shown, for the two sources. A more systematic investigation of topographic effects, in the presence of subsurface resistive zones representative of hydrocarbon reservoirs, will be undertaken as this research project develops further.

In Figure 5, the secondary $|E_x|$ amplitude is shown as a function of distance from the long dipole source, for various pedestal positions. It is clearly seen that the secondary response curves peak at the pedestal location. At the peak of the 110 m pedestal position the secondary field amplitude is 3.79% of the primary field amplitude. Furthermore, the peak secondary response is diminished as the pedestal is located further from the source. The curves are asymmetric, with a shoulder located toward the source. The asymmetry reflects the asymmetric geometry of the pedestal, as shown in Figures 1—4.

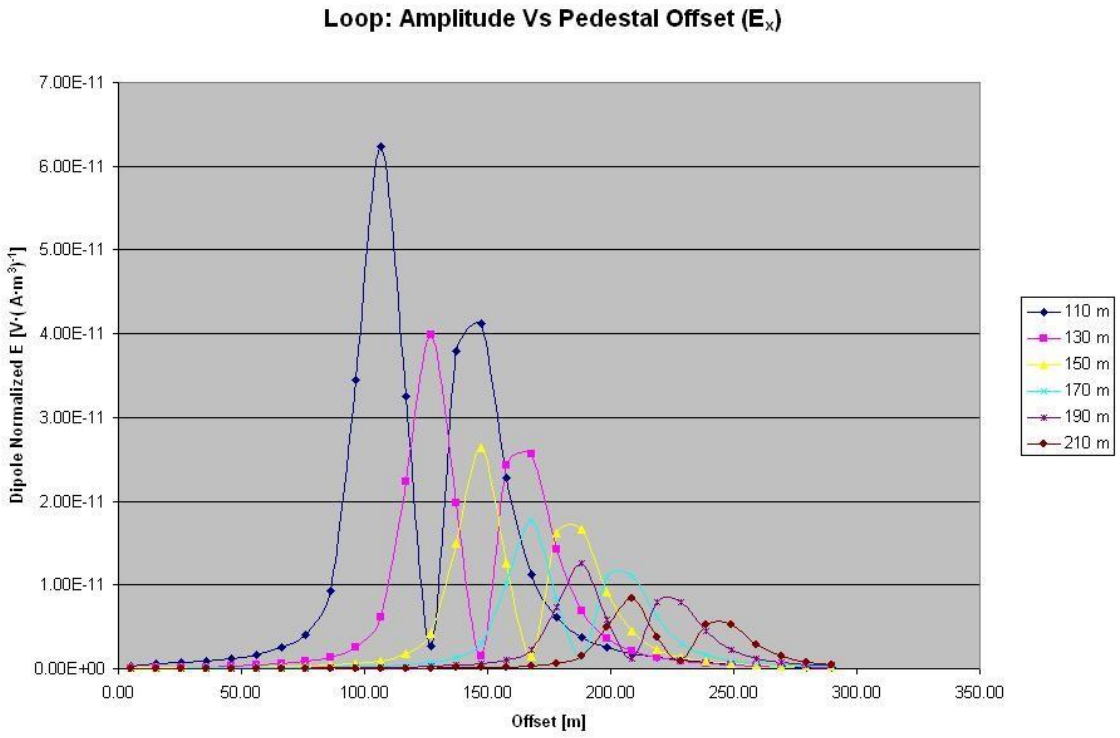

Figure II-6 The amplitude of secondary electric field |Ex| as a function of distance from the loop source. The various curves are for different pedestal locations from x=110 m to x=200 m, as indicated in the legend. Reprinted with permission from Hickey et al. (2010).

In Figure 6, the secondary $|E_x|$ amplitude is shown as a function of distance from the finite—radius loop source, for various pedestal positions. The secondary response curves are double—peaked, and centered at the pedestal location. Furthermore, the amplitude of the peaks diminishes as the pedestal is located further from the source. The central minimum in each secondary response curve is caused by the absence of electric field in the center of the horizontal current vortex flowing in the pedestal.

We have qualitatively explained the behavior of the secondary $|E_x|$ responses generated by the pedestal terrain. The other field components have also been computed but due to space limitations they are not shown here.

Conclusion

The early results from a new Coulomb—gauged finite element analysis of land—based CSEM exploration of terrestrial hydrocarbon reservoirs beneath rugged terrain have been presented and qualitatively explained. The topographic effect is highlighted here. Further development of the project shall involve analysis of grounded source arrays deployed over resistive hydrocarbon zones in the presence of rough terrain and oilfield cultural noise.

CHAPTER III

MONITORING AND IMAGING THE DYNAMICS AND EXTENT OF HYDRAULIC FRACTURING FLUID MOVEMENT USING GROUND-BASED ELECTROMAGNETICS, WITH APPLICATION TO THE EAGLE FORD SHALE*

Overview

Hydraulic fracturing enables more effective production of hydrocarbons from poorly- or non-producing, low-permeability formations. An important property in hydraulic fracturing, that directly affects well performance, is the distribution of proppant within the formation along the well path. Sufficiently sensitive controlled-source electromagnetic (CSEM) induction techniques may be able to image this distribution due to the conductivity of the fracturing fluid which carries the proppant, and its contrast with that of the surrounding geological medium. We present both modeling and real-world data from the application of CSEM to the monitoring of fluid migration during hydraulic fracturing. First, to predict the expected response using CSEM exploration techniques, we present results from a 1-D numerical model and a 3-D finite element model. The 1-D and 3-D models generate frequency domain responses using Lorentz and Coulomb-gauged potentials, respectively, to solve Maxwell's equations. We have run multiple scenarios for the 1-D and 3-D cases and show that with current technology it may be possible to detect the movement and extent of hydraulic

*Part of this chapter is modified with permission from "Monitoring and Imaging the Dynamics and Extent of Hydraulic Fracturing Fluid Movement Using Ground-Based Electromagnetics, with Application to the Eagle Ford Shale" by Hickey, M. S., Treviño, S., & Everett, M., 2015. Proceedings of the 3rd Unconventional Resources Technology Conference, 2015, pp. 2417-2429, Copyright [2015] by Unconventional Resources Technology Conference (URTeC).

fracturing fluid at practical depths. Finally, real-world data from the Eagle Ford formation in Texas are presented which explore CSEM imaging of migration of hydraulic fracturing fluid into the formation. The transmitter and receivers are located on the surface, eliminating the possibility of interference with fracturing operations due to down-hole instrumentation. The ability to image the areal extent and movement of hydraulic fracture fluid would make high-resolution CSEM an efficient tool to directly assess the effectiveness of a hydraulic fracture stage. Near-real-time processing and delivery of results in the field enables data-informed decision-making before the remaining well stages are fractured.

Introduction

The controlled-source electromagnetic (CSEM) method has a long history in geophysical exploration. It has been used in its inductive mode for application including ore detection in mining and discrimination and classification of unexploded ordnance in munitions response. Much of the CSEM now routinely used in hydrocarbon detection is performed offshore to detect and monitor resistive reservoirs based on galvanic mode excitation. Adapting CSEM technology for onshore oilfield applications presents new challenges.

CSEM works best when there are large conductivity or resistivity contrasts between the target and the surrounding medium. Hydraulic fracturing presents a promising area for CSEM technology. There is a known depth interval and a confined volume into which conductive fluids are injected into the surrounding rock. The

resulting fluid invasion changes the bulk conductivity of the volume, producing a change in the CSEM response at the surface. It is desirable to model the change in CSEM response and thereby estimate the magnitude of signal change. After modeling, this knowledge is applied in the field and actual signal changes are recorded which, along with other datasets, can be used to interpret the extent of the fracture fluid invasion.

Modeling

To model the expected response measured by a CSEM system due to the injection of hydraulic fracturing fluid we use software developed at Texas A&M University called LandCSEM which is based on a finite-element forward modeling approach that solves the Coulomb-gauged Maxwell's equations in the frequency domain (Badea et al., 2001). By defining a set of known electromagnetic (EM) primary potentials ($\mathbf{A}_p$, ψ_p) as the response to a given conductivity structure $\sigma_p(\mathbf{r})$, in this case produced by the interaction of the transmitter, a grounded horizontal electric dipole, with the subsurface, Maxwell's equations are then solved for the secondary EM potentials ($\mathbf{A}_s$, ψ_s) due to the anomalous conductivity structure $\sigma_s(\mathbf{r})$ that represents the fracturing fluid. For the following discussion, we model fluid injection into a uniform half-space of conductivity 0.01 S/m. The vertical z-direction is positive downward and the transmitter is positioned at the surface (z = 0).

The fracturing stage to which we will compare our modeling data is presumed to have occurred near the toe end of an injection well. Additionally, to determine how the conductivity of the steel well casing affects the CSEM response of the injected fluid, a

finite element mesh is created that includes the well casing, as shown in Figure 1. Here, the horizontal casing is located at depth z = 3150 m, extending from x = 0 m to x = 1540 m. On the surface, the transmitter is centered near one end of the casing, at x = 1400 m, and aligned parallel to it. The node spacing at the surface around the transmitter is refined to a spacing of 4.375 m.

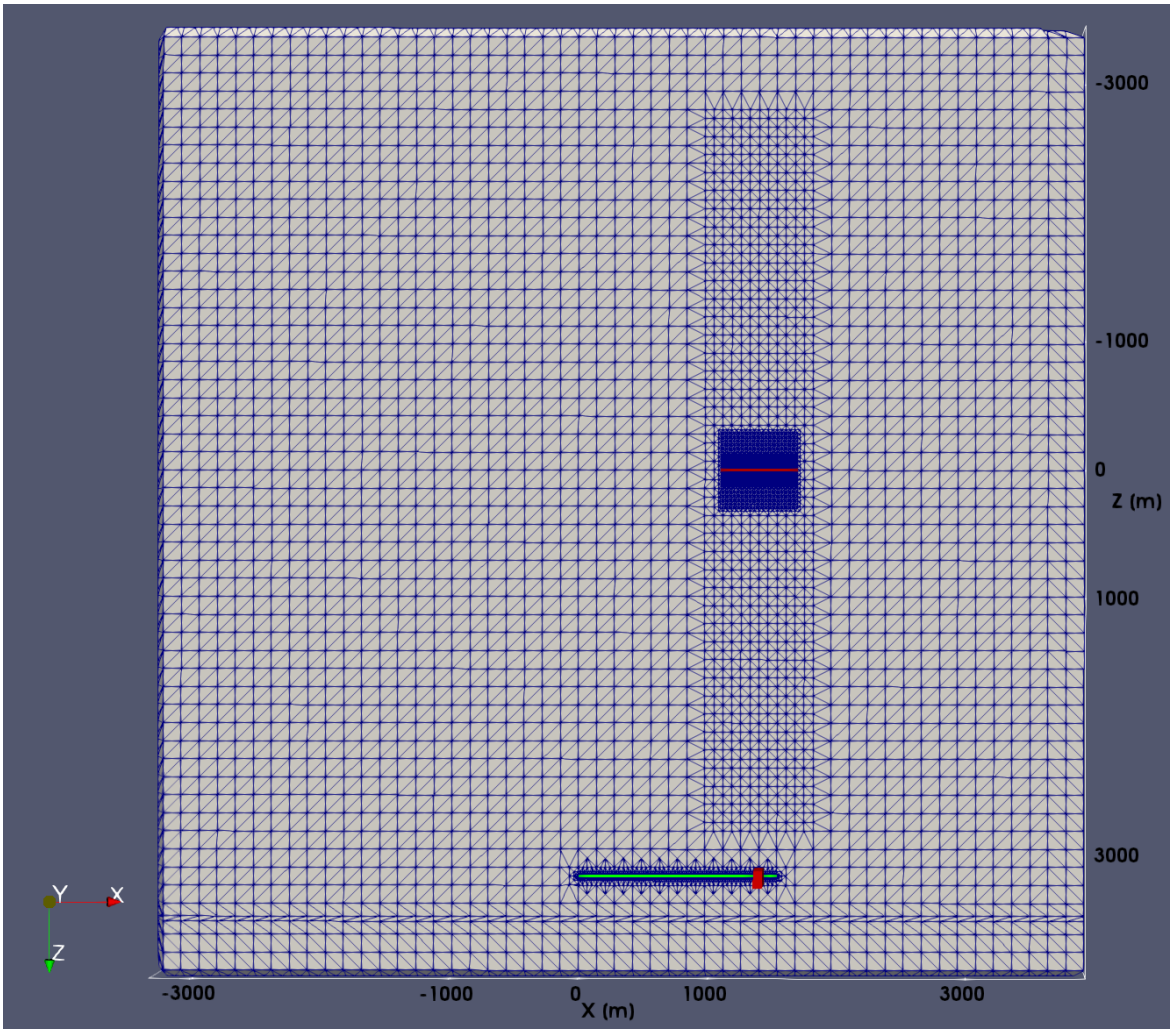

Figure III-1 Slice through the X-Z plane of a section of the 3D model space. The dark red line represents the transmitter location. The green line represents the casing. The red box represents the location of the fracture volume.

Using local refinement, the node spacing at the locations of the pipe is set to 0.55 m and the pipe cross section is centered on a node. Local refinement allows the mesh to conform to the pipe geometry, but there is a minimum limit on the spacing distance since the number of nodes corresponds to the memory requirement to run the mesh. If the model has too many nodes, it would not be able to run. Therefore, volume-averaging is used since the radius of the pipe is smaller than the dimensions of a tetrahedral mesh element. By volume-averaging the expected conductivity of the steel casing with the expected conductivities of the surrounding background and the enclosed proppant, the conductivity inside a tetrahedral mesh element containing the casing is estimated to be 9.2×10^4 S/m. Volume averaging has been proven effective for conductivity contrasts on the order of 10^3 or less, but the method breaks down for finite difference cells relatively larger than the size of the casing (Hoversten et al 2015). Since the conductivity contrasts for our model are on the order of 10^8, the model accuracy will not be as accurate. In order to increase the accuracy of the model, the casing should be represented as close to its actual size as possible (Puzyrev 2017); however, since the induced electrical currents will travel on the outside of the casing, it is accurate enough to represent the casing as solid with a weighted material average (Um et al 2015). There is no unique way to do the volume averaging and other methods should be explored.

Fracture Signal versus Background

To compare the strength of the fracture-fluid-generated signal against the background pre-fracturing (primary signal), with and without the effect of the casing, we first solve for the background CSEM response of the halfspace including the pipe. This response was found for 32 different frequencies stepping from 0.1 Hz to 56 Hz. The largest response, with an x-component E field amplitude of about 2.2×10^{-8} V/m at a location near the transmitter, was found at a frequency of about 17.78 Hz. The frequency reponse is dependent on casing length, depth, source receiver geometry, and host conductivity. Variation of these parameters can change the optimal frequency response. Thus, due to its sensitivity to structure at the depth of the pipe, 17.78 Hz is used as the transmitter frequency for remainder of the results in this section.

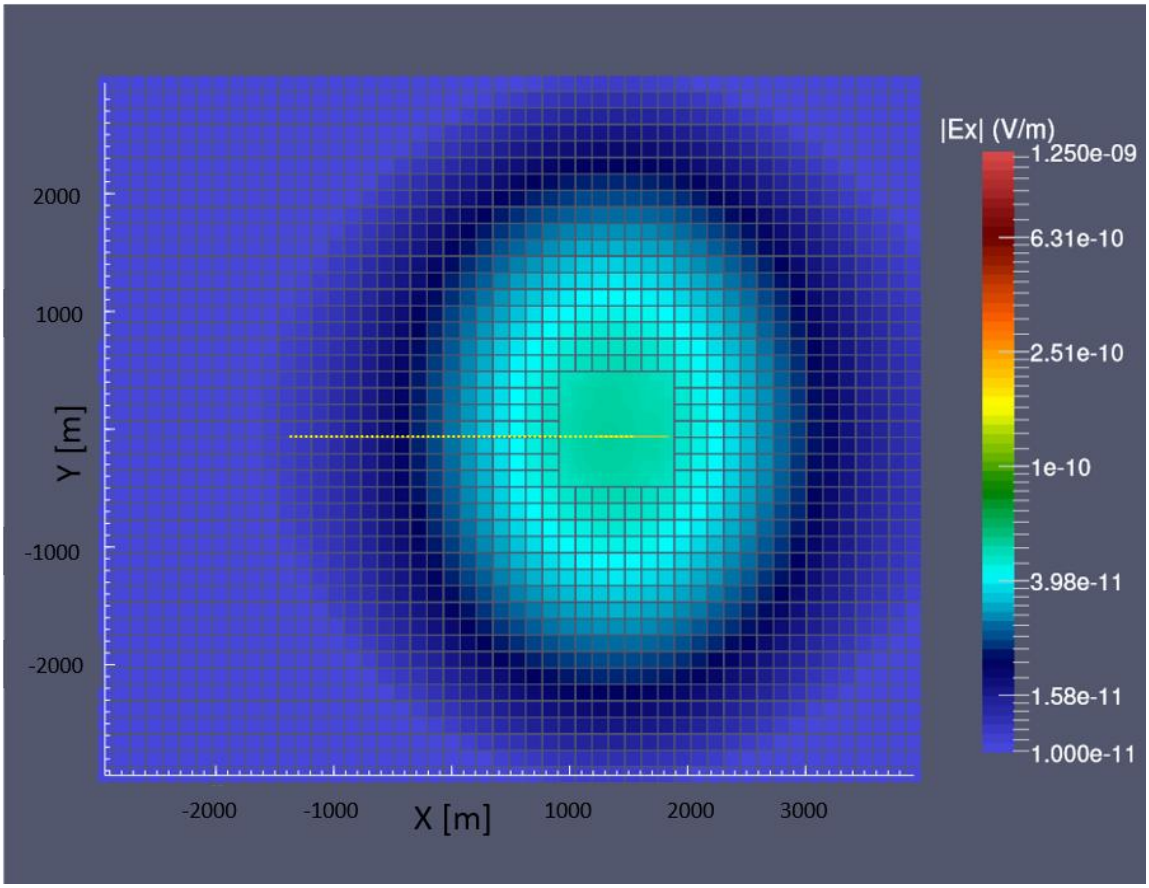

Figure III-2 Map view of the x-component Electric Field Amplitude at the surface with no casing. The yellow dotted line represents the casing at depth. The green solid line is the dipole source at the surface. Modified with permission from Hickey et al. (2015).

To simulate the CSEM response following injection of hydraulic fracture fluid, the secondary potentials are found for a slab (representing the invaded fluid) at a depth of 3150 m with a width of 70 m in the x-direction, a length of 280 m in the y-direction, a thickness of 35 m, and a conductivity of 1.0 S/m. This represents the full extent of fluid injection following a fracturing stage. The dimensions for the slab were set by using information from field operations: the length along the horizontal section of the well casing for one stage was set to be 70 meters; the estimated distance the fracture network

would grow away from the well casing was given to be 140 m in each direction; and the estimated height of the frac for the formation and area was estimated to be 35 meters. The slab represents the ideal fractured volume. In order to model the expected response from a field operation, the model must be built so that it represents the field setup as closely as possible. A smaller scale mesh would not have the correct parameters needed to show the needed interaction of the casing, target, and source. The mesh is already a smaller scale by sacrificing accuracy in the representation of the casing target. The resulting CSEM response at the surface is shown in Figure 2 and Figure 3, respectively with and without the effect of the pipe casing. At this frequency, it is seen that the casing increases the CSEM response of the injected fluid by about two orders of magnitude.

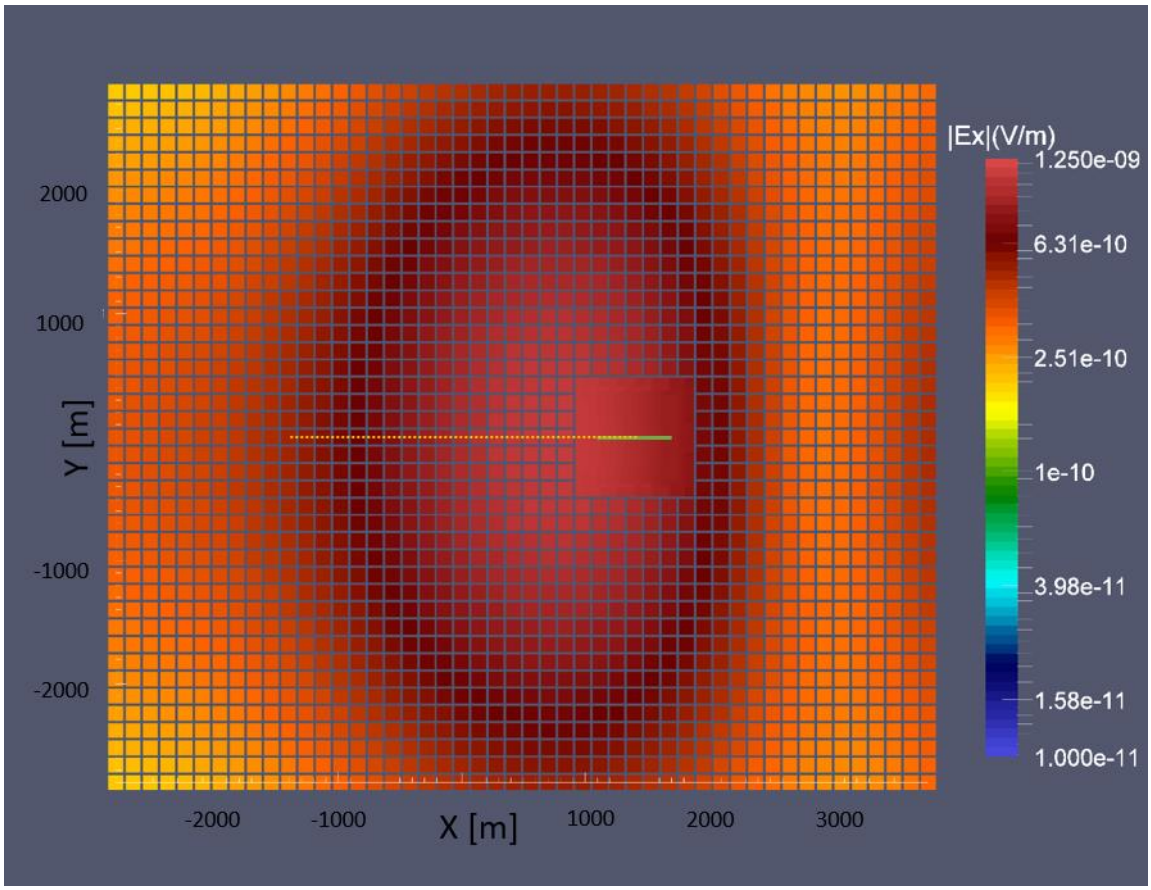

Figure III-3 Map view of the x-component Electric Field Amplitude at the surface with casing. The yellow dotted line represents the casing at depth. The green solid line is the dipole source at the surface. Modified with permission from Hickey et al. (2015).

The fracture versus background CSEM-response ratio is conveniently defined as:

$$\text{FvBR} = 100\% \left| \frac{\text{Secondary Field}}{\text{Primary Field}} \right|.$$

The corresponding FvBR plot for the response including the effect of the pipe casing is shown in Figure 4. In this figure the primary field is the summation of the field from the transmitter and the response of the pipe. At the location of receivers near the transmitter

the FvBR, including the effect of the casing, is of order 10^{-3} to 10^{-4} indicating the need for a receiver system with -120 dB of signal to noise ratio (SNR) and at least 120 dB of dynamic range.

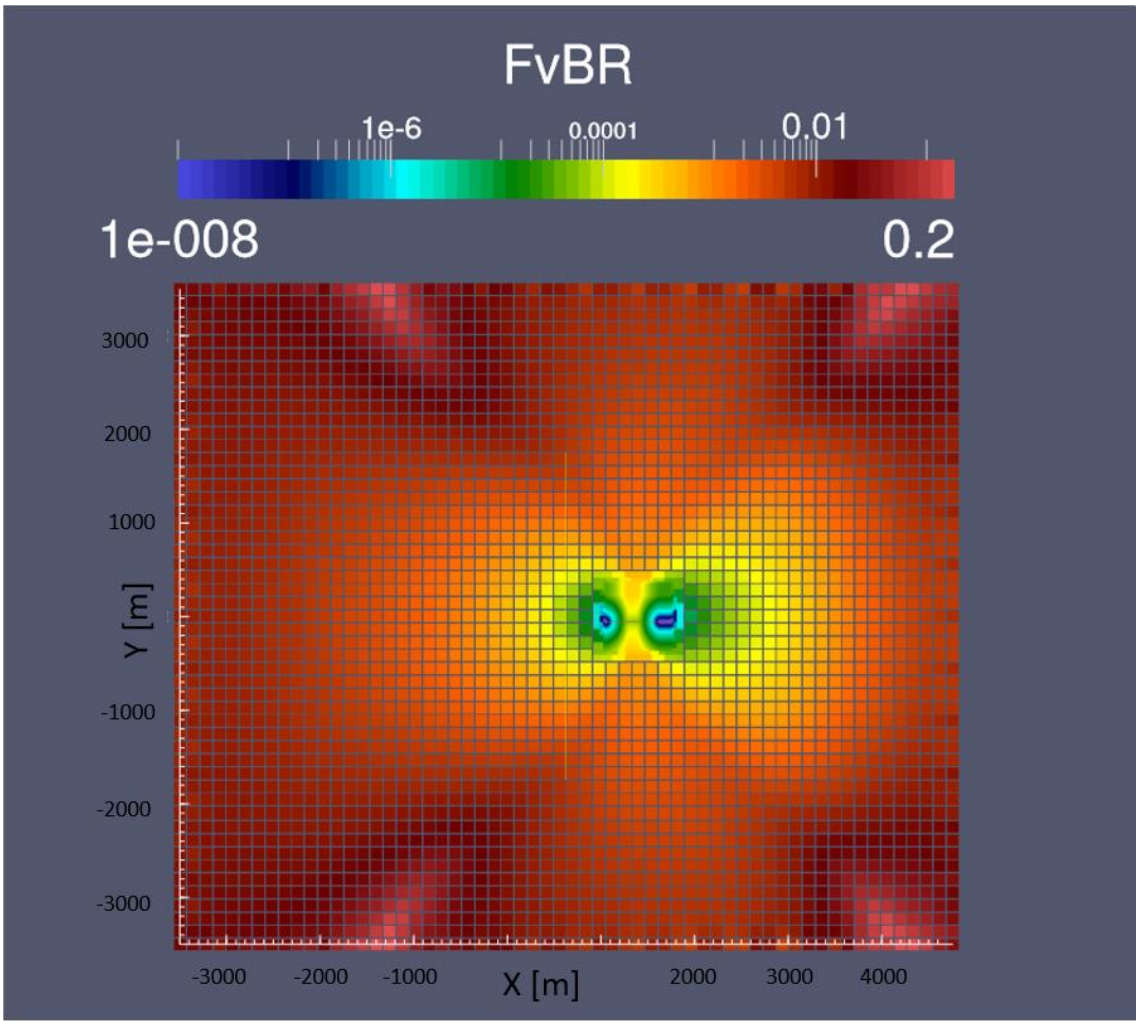

Figure III-4 Map view of fracture versus background at the surface. Modified with permission from Hickey et al. (2015).

Field Methodology

Setup of the transmitter and receivers follows a standard practice for every frac monitoring layout. The standard transmitter and receiver layout can be seen in figure 5. The transmitter line is arranged 1000 feet (about 300 meters) out from both sides of the transmitter console along the surface and directly above the lateral wellbore. This makes the total length of the transmitter 2000 feet (600 meters). To monitor the first stage, we extend the transmitter line beyond the end of the lateral and center the transmitter above the 1st stage.

The electric-dipole receivers have multiple channels and each channel can be arranged as either parallel or orthogonal to the transmitter dipole moment. The receiver dipoles are typically 200 feet long. The electric field recorded on each of these channels can be considered as a data point for interpretation. The configuration of the receivers may change to increase or decrease specific components of the electric field response. While the orthogonal RX-dipole orientation provides more information about the frac, the signal strength is typically two orders of magnitude lower than signals using the parallel RX-dipole orientation. The larger signal of the parallel orientation allows for easier processing and shorter stacking time. The offset of the receivers from the transmitter is determined by the strength of the transmitted signal. If the receivers are too close, the primary signal is too strong, saturates the equipment, and we cannot retrieve the secondary response from the subsurface. This problem can be solved and is discussed later in this paper.

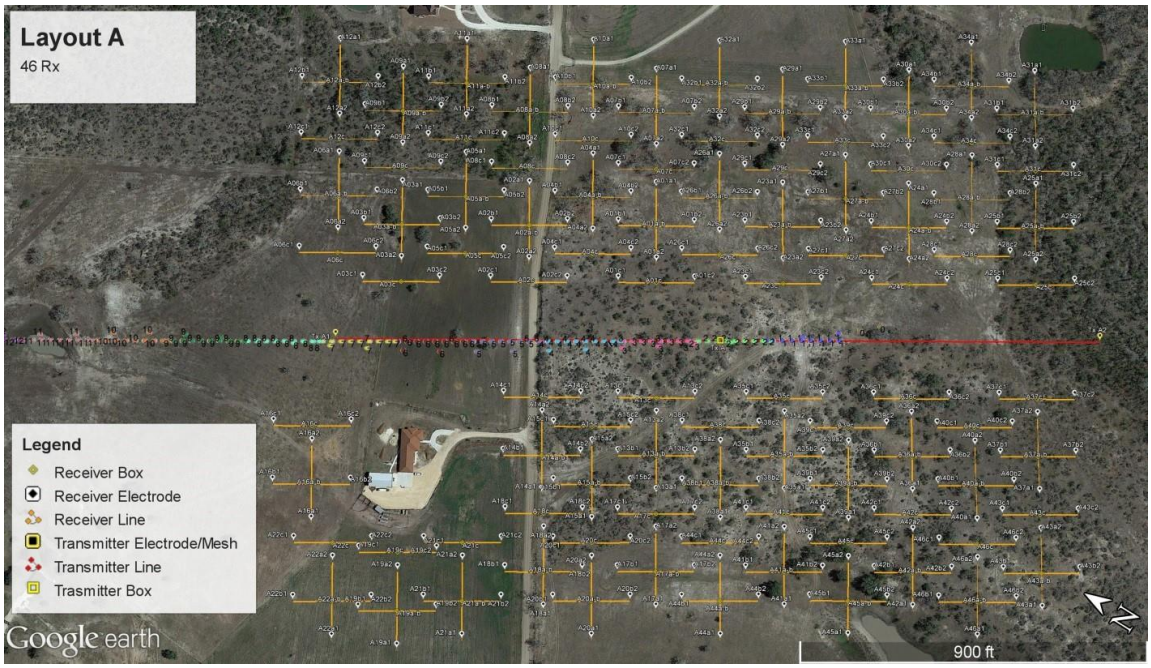

Figure III-5 Typical CSEM layout for hydraulic fracture monitoring. Reprinted with permission from Hickey et al. (2015).

A typical layout will cover about 3 to 5 stages of a frac job. After each stage is monitored, data are removed from the receiver boxes and sent off for processing. In order to follow the frac, the transmitter and half the receiver boxes are moved to the next stage section while the well perforation is being performed.

Data Processing

Data from each receiver channel are processed in the following manner. First, the transmitter signal is removed. This results, for a range of frequencies, in the secondary response due to the change in the subsurface conductivity. Depending on the depth and the extent of frac fluid injection, there is a different secondary response at each frequency. The data capture the amount of energy in the CSEM response for a specific

frequency over a specific time window. Having a dense frequency content allows for more robust exploration of the target. In the final processing step, we sum the responses across a pre-determined range of frequencies and display the resulting summation as images and videos that are intended to indicate the extent of the frac fluid. We show the images in two ways: as signal energies that change through time or as the temporal accumulation of signal energy. The latter would better show the overall extent of the fluid invasion while the former would show the location of fluids at a given time step. Imaging subsurface regions of non-accumulation is helpful in revealing locations where the fluids do not access the formation due to poor proppant placement. The accumulation view would show the total connection length of the frac.

Real-world Data: Atascosa County

Data were taken on select stages during a multi-well fracture job. The stages monitored were only on the second well of the job. Only the parallel electric-field component was measured. There are only two electric-field components per receiver box in this original version of the hardware. The proximal receiver lines are offset by 250 feet from the transmitter line while the distal receiver lines on each side are offset by 625 feet. The first well and the first 3 stages of the second well had already been subjected to fracturing and therefore there was fluid in the subsurface at the start of the CSEM measurements. The data therefore would provide an indication of fluid interconnectivity between the already completed stages on both wells. The layout for stages 4 and 5 can be seen below in Figure 6.

Figure III-6 Transmitter and receiver layout for Atascosa county. Reprinted with permission from Hickey et al. (2015).

The processed output in this case is a single electric field component per receiver location for multiple frequencies. Each frequency is assigned to a pseudo-depth with the higher frequencies closer to the surface and the lower frequencies deeper. In this case the frequency range is 35 Hz near the surface to 15 Hz near the bottom of the modeling domain. The CSEM response in areas between the receiver locations is interpolated using a nearest neighbor scheme. At the beginning of the processing the background response is subtracted from the data so that the displayed response is that of the electric field due to conductivity changes within the subsurface. These conductivity changes are presumed to be due to the injection of fluids into the surrounding rock. A larger value of the CSEM response, whether positive or negative, is interpreted as an increase in conductivity and therefore an increase in the amount of fluid in the rock. It is assumed

that all temporal changes in the CSEM response are due to migration of fracturing fluid and not due to extraneous environmental effects. It is important to note that this assumption has not been tested by detailed modeling studies.

The limitations of this case study are that it assigns only one frequency per depth, it assumes a single data point for a receiver line that is actually 200 feet long, and the interpolation assumes data are available within areas where they are not actually recorded. To help alleviate these limitations, improvements have been made to processing techniques. To overcome only displaying a single frequency we have summed the results from a range of frequencies that modeling has shown to be sensitive to fluid-injection-related conductivity changes. These frequencies are calculated on a site-specific basis. In order to bypass the problem of data being a single point, later visualizations are done using the entire receiver line as the data point. This is done because the data gathered is an average across the entire length of the receiver. And last, we have increased data density to show that interpolation can be used in relatively homogeneous overburdens that do not contain strong near surface 3D heterogeneities. All of these improvements can be seen in the second case study, described below.

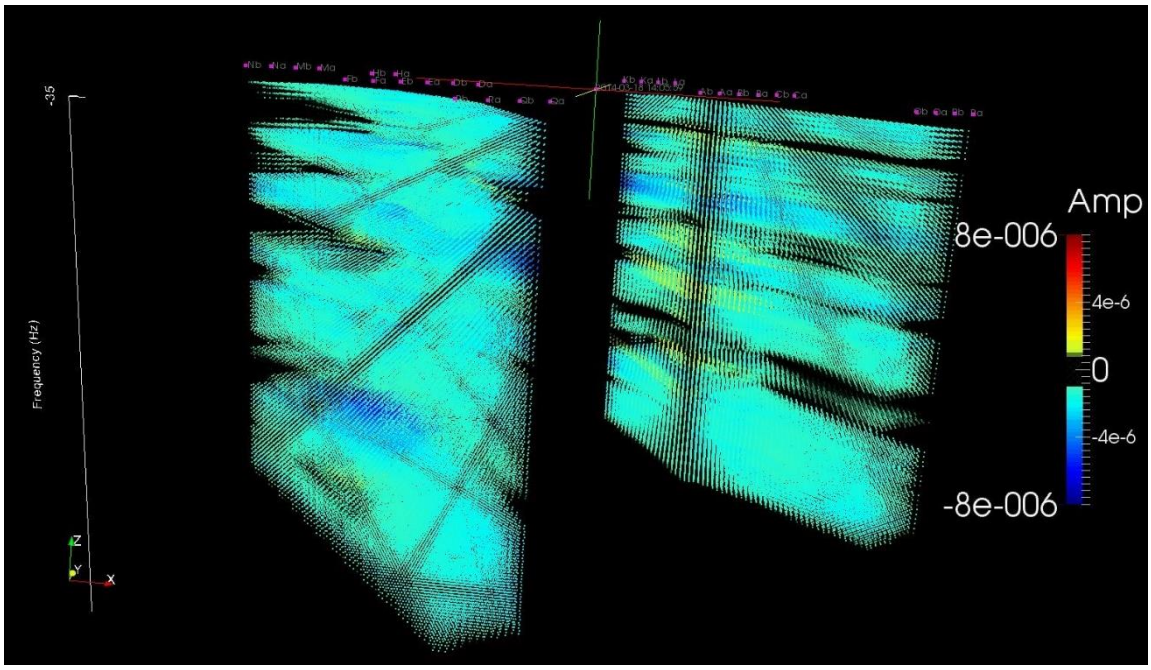

Figure III-7 Stage 5 time step 45/290. Change in amplitude over time for E_x. Interpolation for the group of receivers on either side of the transmitter. Reprinted with permission from Hickey et al. (2015).

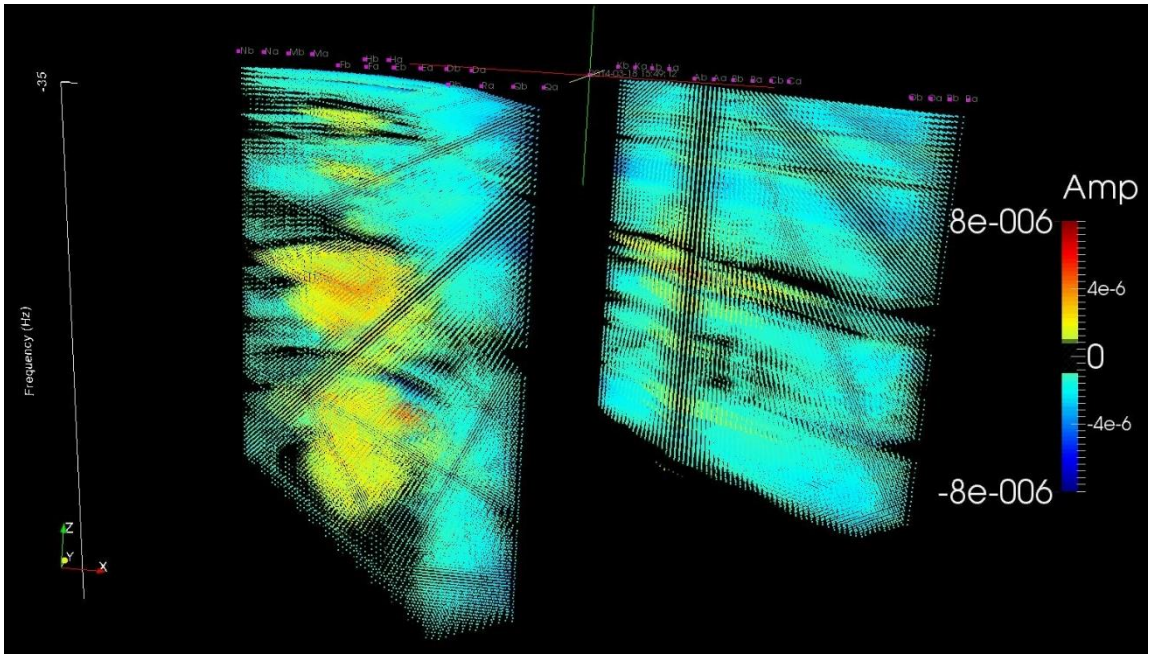

Figure III-8 Stage 5 time step 242/290. Change in amplitude over time for E_x. Interpolation for the group of receivers on either side of the transmitter. Reprinted with permission from Hickey et al. (2015).

In Figure 7, at the beginning of the frac job, we can see more localized change in amplitude over time to the area around stage 5. These responses were recorded before the pressure was increased and during an acid injection. The small changes in signal are interpreted to be associated with the change in conductivity due to injection of acid into the structure; however, forward modeling is needed to support the interpretation. We also see higher values on the right of the transmitter indicating, according to the interpretation, that acid infiltrated the rock there before the frac started. Most of the signal during stage 5 is very low until 2 hours into the frac when a large pressure increase produced the larger signals seen in Figure 8. The signal in this case is greater on the left side of the transmitter. The signal is also larger across a wider frequency range.

This can be interpreted as a larger fluid-injection volume in the vertical direction due to the relationship between conductivity and frequency and electromagnetic skin depth.

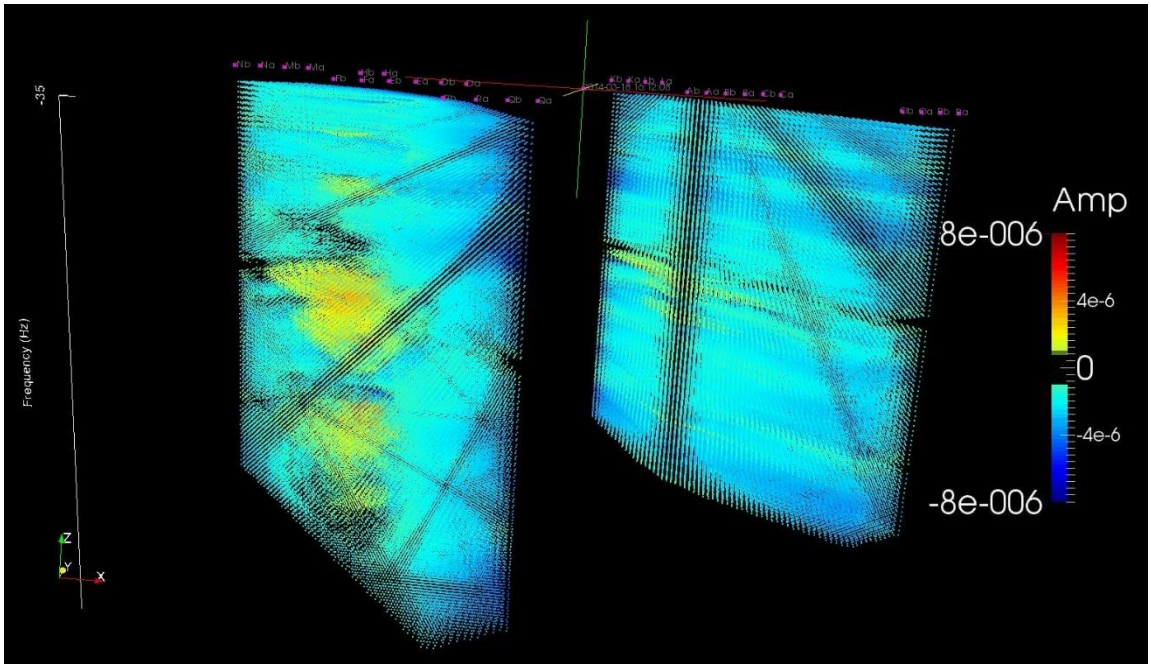

Figure III-9 Stage 5 time step 290/290. Change in amplitude over time for E_x. Interpolation for the group of receivers on either side of the transmitter. Reprinted with permission from Hickey et al. (2015).

Figure 9 shows the data at the end of stage 5, after the pumps have shut down. We see a decrease in CSEM signal, which according to the interpretation indicates that the fluid has recessed due to the absence of proppant. After the pumps are turned off, either there is insufficient pressure to keep the fractures open without proppant, or else the proppant did not keep the fractures open as much as it did at full pressure. The fluid moves to other locations as the fractures close and therefore the CSEM signal decreases.

Our final interpretation of stage 5 is that during the frac there was insufficient pressure to open up new fractures until 2 hours into the job when the pressure was increased. The proppant seemed to be distributed uniformly on the left of the transmitter line, but the right side seems to have had substantially less injection of proppant. For the optimization of our CSEM equipment for this stage, we should have increased the number of receivers and increased the overall transmitter-receiver offsets. It can be seen in Figure 9 that the frac effects went beyond the locations of the receivers, so larger receiver offsets could have captured the full extent of the fluid invasion. Again, it is important to note that the aforementioned interpretations should be rigorously tested against detailed numerical simulations.

Real-world Data: Karnes County

In this case study, CSEM data were acquired on most stages during a frac job. The transmitter and receiver boxes were moved every 5 stages while well perforation took place. No other laterals were located near this well. Two parallel components of electric field and one orthogonal electric-field component were measured. The proximal receiver lines are offset 150 feet from the transmitter line while the distal receiver lines on each side are offset at 675 feet. To reduce edge effects of the transmitter dipole, specifically the orthogonal component from the primary field on the receiver boxes, i.e. to simulate an infinite line source, we extended the transmitter to 4000 feet. This was

found to give an improved response on the receivers. The layout for stages 1 and 2 can be seen below in Figure 10.

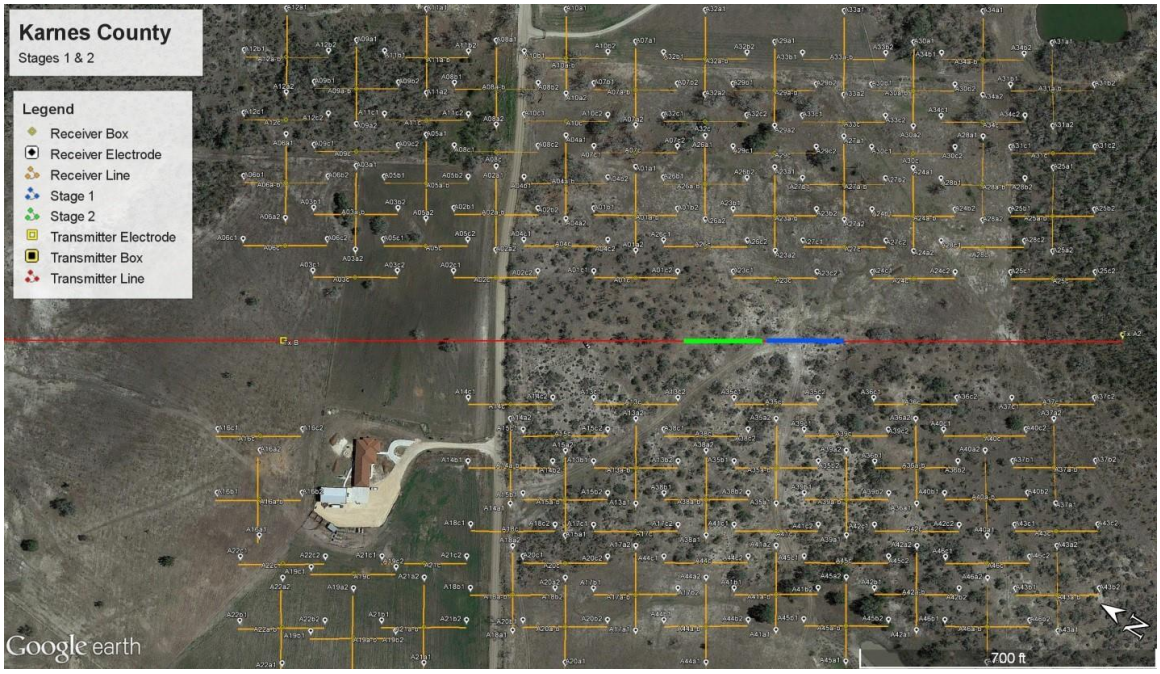

Figure III-10 Transmitter and receiver layout for Karnes county. Reprinted with permission from Hickey et al. (2015).

For the output of this data set we used the improvements learned from previous experience. We increased the data density, summed over the frequency range of 1 Hz to 20 Hz, and used responses from the entire receiver line. Another difference in this data set is the display of energy accumulation. Instead of attempting to showing the changing fluid locations as a sequence of snapshots, we attempt to show the total extent of the fracture fluid, summed over time. Figure 11 shows the location labels in order to help with interpretation.

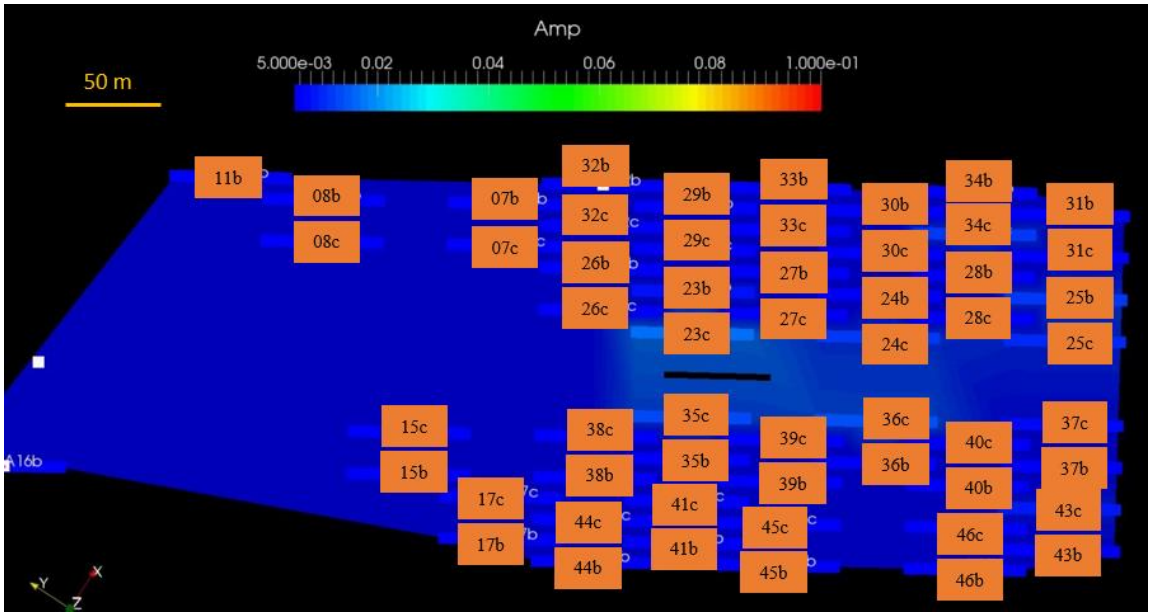

Figure III-11 Plan view of data results with location labels used for interpretation. Modified with permission from Hickey et al. (2015).

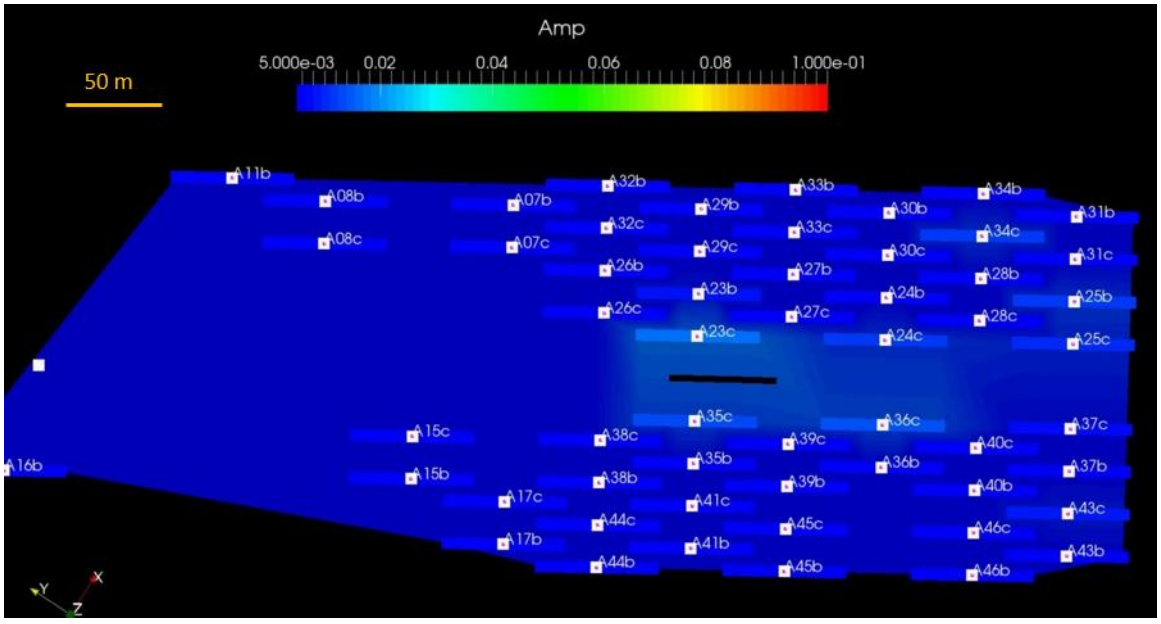

Figure III-12 Stage 1 time step 45/310 plan view. Change in amplitude over time for E_x. The black line is stage 1 and the toe end is to the right. Modified with permission from Hickey et al. (2015).

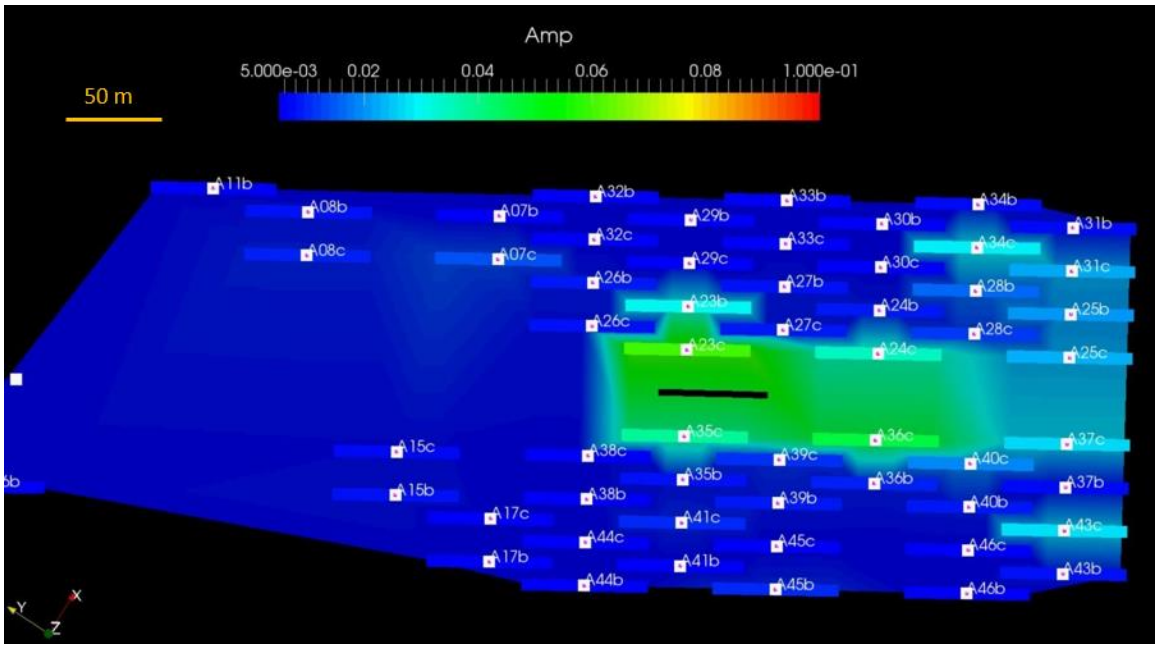

Figure III-13 Plan view of stage, 1 time step 242/310. Change in amplitude over time for E_x. The black line is stage 1 and the toe end is to the right. Modified with permission from Hickey et al. (2015).

In Figure 12 shows the CSEM response at the start of the frac. The initial interpretation shows a favorable fluid pathway towards the upper area around receiver 23c, but figure 12 also shows some energy appearing to the right and down around receiver 36c. According to the interpretation, Figure 13 shows a larger extent of fluid-invasion into the upper area, but with some signal energy to the bottom and to the right.

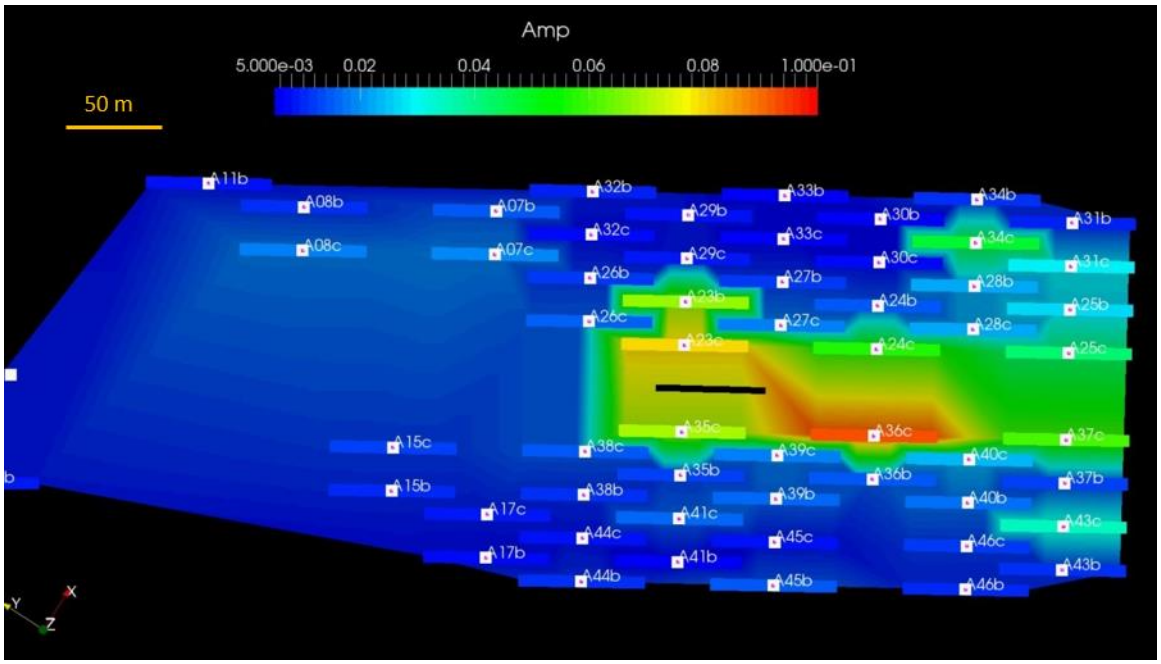

Figure III-14 Plan view of stage 1, time step 281/310. Change in amplitude over time for E_x. The black line is stage 1. Modified with permission from Hickey et al. (2015).

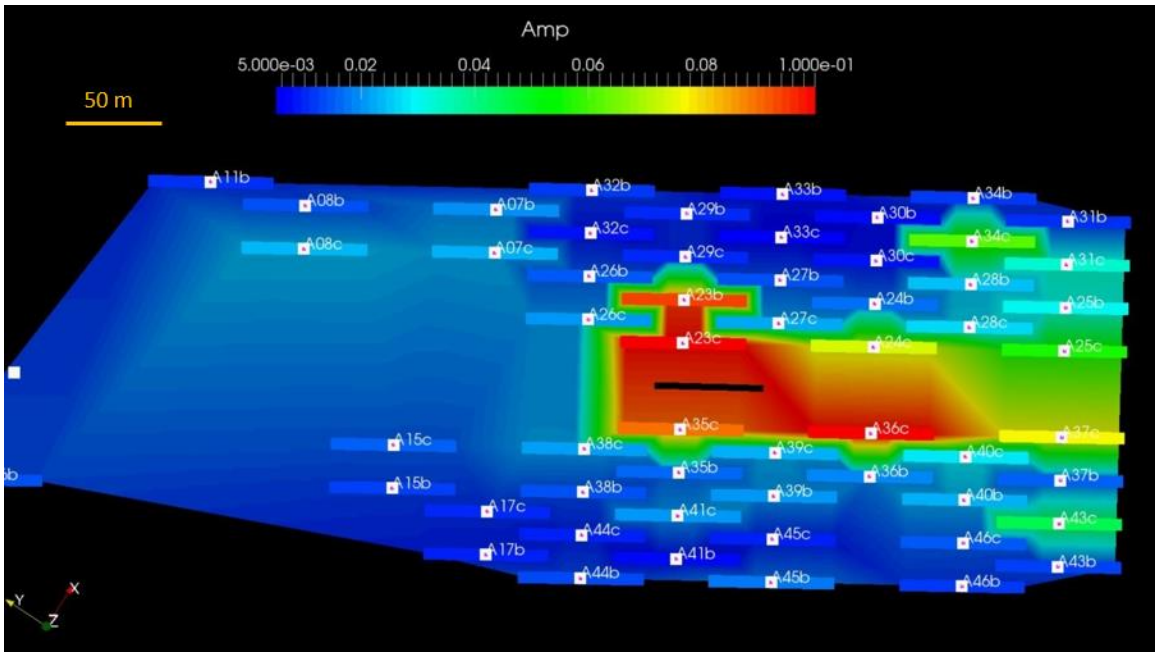

Figure III-15 Plan view of stage 1, time step 310/310. Change in amplitude over time for E_x. The black line is stage 1. Modified with permission from Hickey et al. (2015).

According to the interpretation, Figure 14 shows more fluid around receiver 36c. Since this is the toe end, we expect complicated fluid dynamics due to the presence of the end of the pipe. We also see higher signal energy around receiver 34c and slightly elevated values leading towards 36c in receiver locations 28b and 28c. This is interpreted as fluid migration along a fracture from 24c, 28c and 28b to 34c. Here, there is a larger volume of fluid indicated by a larger signal. In the final image of Figure 15 we see large signal in 23b and 23c, but not as much on the other side at 35c. Therefore, it is interpreted that most of the fluid migrated to the upper area and to the right.

Our final interpretation for stage 1 is that the frac fluid did not extend very far into the formation. The extent of most of the fluid is about 200 feet to the upper area towards 23b and the lower extent is about 100 feet near 35c. There is also a large amount of fluid that went to the right towards the toe end. This could be due to complex geology or the complication of stress fields near the end of the lateral. As in the previous case study, the aforementioned interpretations are not supported by detailed numerical simulations.

Also of note are the signal levels measured by the receivers to the far right. These receivers are near one of the transmitter grounding points. The transmitted field near the end of the transmitter has high spatial gradients. To alleviate this problem, we now extend the transmitter dipole beyond the last receiver location, or else not use the measurements if they contain this this edge effect. The use of a long transmitter centered directly above the lateral, with grounding points located far from the fluid migration

region, indicates that we are observing predominantly an inductive-mode response of a conductive target. This stands in contrast to traditional marine CSEM oil reservoir surveys which rely on galvanic-mode excitation of a thin resistive target.

Conclusions

In summary, we have shown that inductive-mode CSEM monitoring using a long grounded-dipole source and electric-field receivers could become a viable tool for hydraulic fracture monitoring of conductive fluid invasion into a geological formation. Even through these are initial case studies, with plenty of room for improvements to be made, CSEM has been demonstrated to provide potentially valuable information on fracture fluid injection and migration. The CSEM data can be used to optimize well spacing and determine possible regions to refracture.

CHAPTER IV

DETECTION AND CHARACTERIZATION OF THE INJECTION OF HYDRAULIC FRACTURING FLUID USING GROUND-BASED CONTROLLED-SOURCE ELECTROMAGNETICS*

Summary

A characterization of the expected response of the injection of hydraulic fracturing fluid detected using ground-based controlled-source electromagnetics (CSEM) is presented. The response of the injection fluid is modeled using a 3D finite element forward model. First, we study the strength of the fracture signal by calculating its percent ratio to the transmitted signal, defined as the FvBR. The FvBR indicates we need -120 dB of signal to noise ratio (SNR) and at least 120 dB of dynamic range for fracture signal detection. Modeling results are compared against field data measurements. Finally, a case study explores the potential of a ground-based CSEM system to detect changes in the subsurface due to hydraulic fluid injection and measure the extent of the fracture fluid.

Introduction

Hydraulic fracturing allows hydrocarbon production in low permeability formations. Imaging the distribution of fluid during a hydraulic fracture can aid in the characterization of fracture properties such as extent of plume penetration as well as

---

* Part of this chapter is modified with permission from "Detection and Characterization of the Injection of Hydraulic Fracturing Fluid using Ground-Based Controlled-Source Electromagnetics" by Hickey*, M. S., Treviño III, S., & Everett, M. E., 2015. SEG Technical Program Expanded Abstracts, 2015, pp. 1039-1043, Copyright [2015] by Society of Exploration Geophysicists.

fracture extent and symmetry. This could aid to improve the efficiency of an operation, for example, in helping to determine ideal well spacing. Ground-based controlled-source electromagnetics (CSEM) may be a useful tool for imaging the fluid due to its conductive properties compared to the background.

To model the expected response measured by a CSEM system due to the injection of hydraulic fracturing fluid we apply a finite-element forward model that solves Coulomb gauge Maxwell's equations in the frequency domain (Badea et al., 2001). By defining a set of known Electromagnetic (EM) primary potentials ($\mathbf{A}_p$,Ψ_p) with conductivity structure $\sigma_p(\mathbf{r})$, produced by the interaction of the transmitter and subsurface, Maxwell's equations are solved for the response of a secondary set of EM potentials ($\mathbf{A}_s$,Ψ_s) with conductivity structure $\sigma(\mathbf{r})$. The governing Maxwell's equations are given by,

$$\nabla^2 \boldsymbol{A}_s + i\omega\mu_0\sigma(\boldsymbol{r})(\boldsymbol{A}_s + \nabla\psi_s) = -i\omega\mu_0\Delta\sigma(\boldsymbol{r})(\boldsymbol{A}_p + \nabla\psi_p) \qquad (1)$$

$$\nabla \cdot [i\omega\mu_0\sigma(\boldsymbol{r})(\boldsymbol{A}_s + \nabla\psi_s)] = -\nabla \cdot [i\omega\mu_0\Delta\sigma(\boldsymbol{r})(\boldsymbol{A}_p + \nabla\psi_p)] \qquad (2)$$

where $\Delta\sigma(\mathbf{r}) = \sigma(\mathbf{r}) - \sigma_p(\mathbf{r})$ is the difference between the primary conductivity and secondary conductivity, the ω is the frequency, and μ is the magnetic permeability of free space. The secondary set of EM potentials are found at each node by solving the finite-element system of equations using the sparse direct solver PARDISO from Intel MKL (Schenk and Gartner, 2004). The electric field due to the found potentials is then given by $\mathbf{E} = i\omega(\mathbf{A}+\nabla\psi)$ where $\nabla\psi$ can be estimated using, for example, a moving least squares interpolation.

The skin depth of an EM signal is dependent upon the frequency of transmission and the medium through which the signal diffuses. Therefore, a system capable of transmitting a broad band of frequencies is better able to concurrently investigate a range of depths. One such broad band transmission method uses a pseudo-random binary sequence (PRBS) to control the source current (Duncan et al., 1980; Ziolkowski et al., 2011). A PRBS is a random binary sequence that repeats after $2^n - 1$ clock pulses where n is an integer. The Fourier Transform of a PRBS has the form shown in Figure 1 where the maximum value of the FT has been scaled to one and the x-axis has been scaled to the clock frequency (f_c). The FT of a PRBS has the property that the first zero occurs at fc and the amplitude of the FT follows the sinc^2 function. The frequency spacing is given by $f_c/(2^n - 1)$. Thus, a PRBS with a small frequency spacing broadcasts a large number of frequencies at essentially equal amplitudes, especially at lower frequencies. Additionally, the autocorrelation of a PRBS resembles an impulse with a height of $2^n - 1$ at a shift equal to 0 and -1 for shifts greater than $2/f_c$.

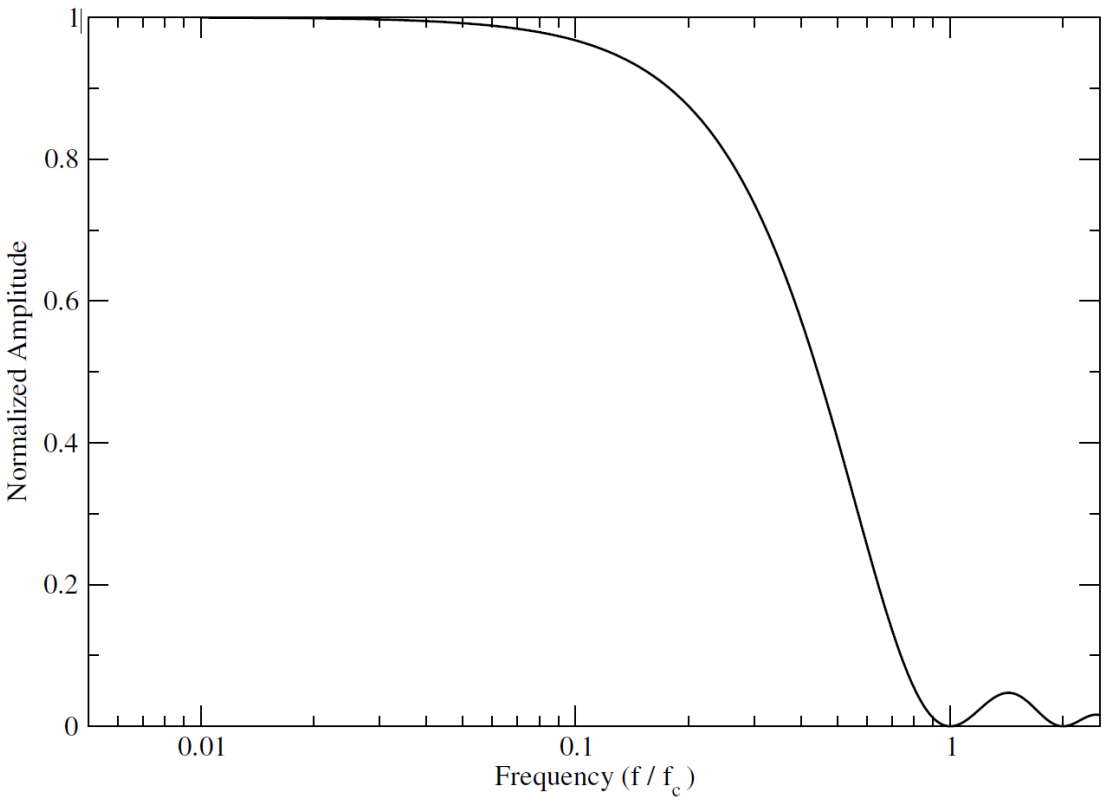

Figure IV-1 Normalized amplitude of the Fourier Transform of a PRBS as a function of relative clock frequency. Reprinted with permission from Hickey et al. (2015b).

Modeling

The following simulation will be compared to stage data occurring near the toe end of an injection well. Figure 2 shows the modeling space representing the stage data area, sliced in the x-z plane. There are two main areas of local refinement. One square volume enclosing the surface of the transmitter/receiver locations and the other at a depth of z = 3150m where the casing occurs. For the following discussion, we model the injection of fluid into a uniform half-space model in which the subsurface is represented using a single conductivity of 0.01 S/m. The vertical z-direction is defined as positive pointing

down into the subsurface and the transmitter, an x-directed 600m long grounded dipole, is positioned at the surface (z = 0) and centered at x = 1400m.

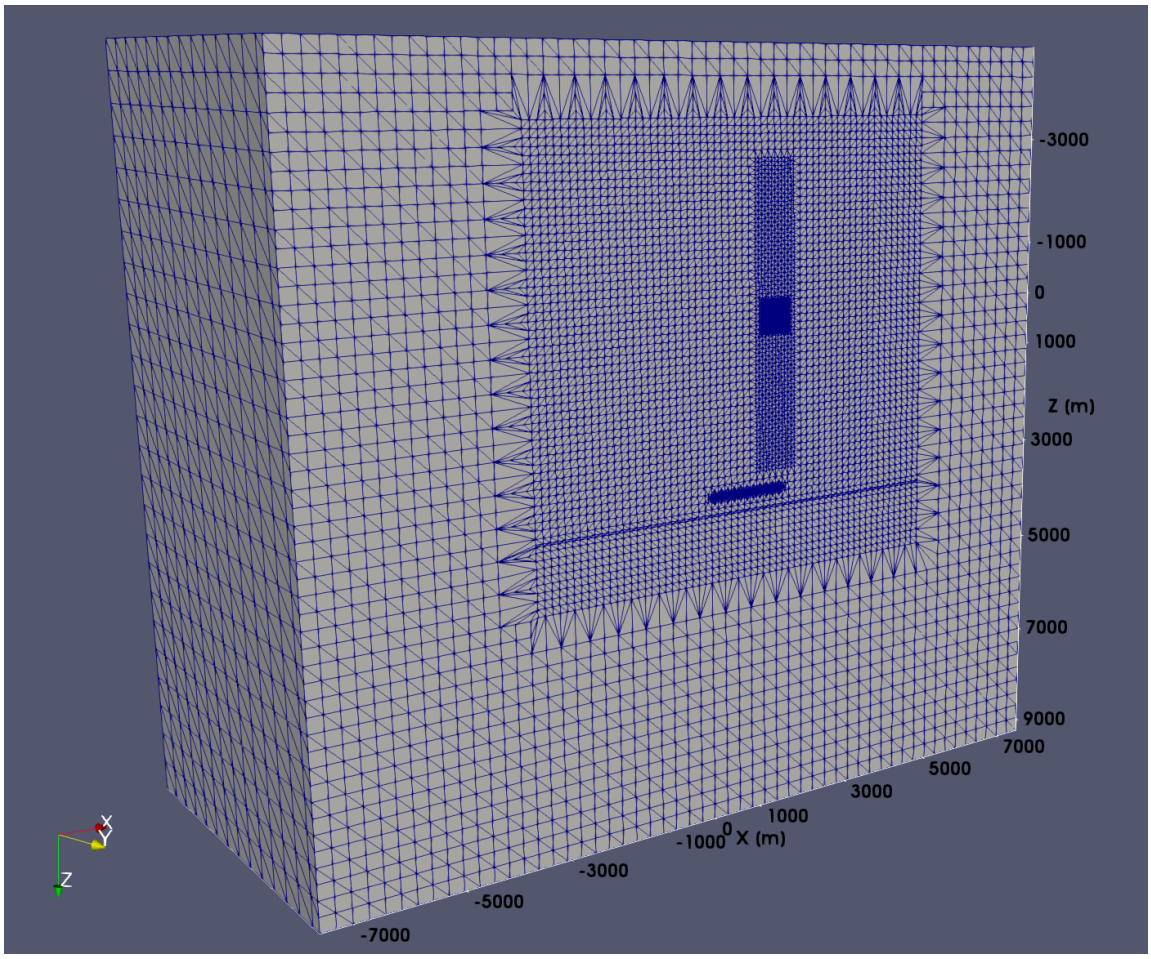

Figure IV-2 Model space showing local refinement for pipe casing and receiver location. Modified with permission from Hickey et al. (2015b).

To estimate the isotropic conductivity in the model space containing the well casing consider Figure 3 which represents a cross section of the pipe where one node in the modeling space is located at each corner of the square. Let the node spacing equal X, the conductivity of the background σ_1, the conductivity of the pipe σ_2, and the conductivity of the injection fluid is σ_3. The outer and inner radius of the pipe is R_2 and

R_1 respectively. Then the conductivity of the entire area is estimated using the area-averaging formula,

$$\sigma = \sigma_1 \frac{X^2 - \frac{\pi R_2^2}{4}}{X^2} + \sigma_2 \frac{\pi\left(R_2^2 - R_1^2\right)}{4X^2} + \sigma_3 \frac{\pi R_1^2}{4X^2} \quad (3)$$

With R_2 = 0.2032 m, R_1 = 0.1905 m, X = 0.546875 m, σ_1 = 0.01 mS, $\sigma_2 = 7\times10^6$ S/m, and σ3 = 1.0 S/m. The average conductivity equals 9.2 x 10^4 S/m

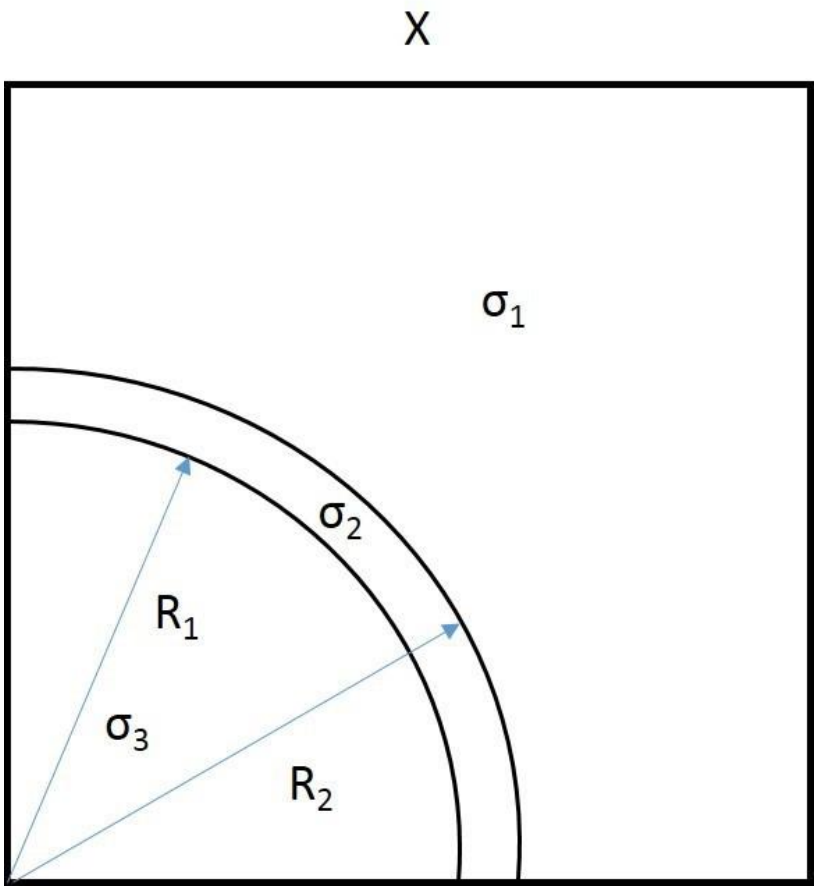

Figure IV-3 Estimating the conductivity for the model space containing the pipe casing. Reprinted with permission from Hickey et al. (2015b).

Fracture Signal versus Background

To compare the strength of the fracture signal vs the background (primary signal), with and without the effect of the casing, we first solve for the response of the pipe by letting the casing define the secondary conductivity $\Delta\sigma$. In Figure 4 the broadside frequency response of the pipe is shown 140 m away from the transmitter for 32 different frequency steps ranging from 0.1Hz to 56Hz. The largest response, with an x-component E field amplitude of about 1.51 $\times 10^{-8}$ V/m, was found at step 21 corresponding to a frequency of about 17.78Hz. Thus, 17.78Hz is used as the transmitter frequency for remainder of the results in this section.

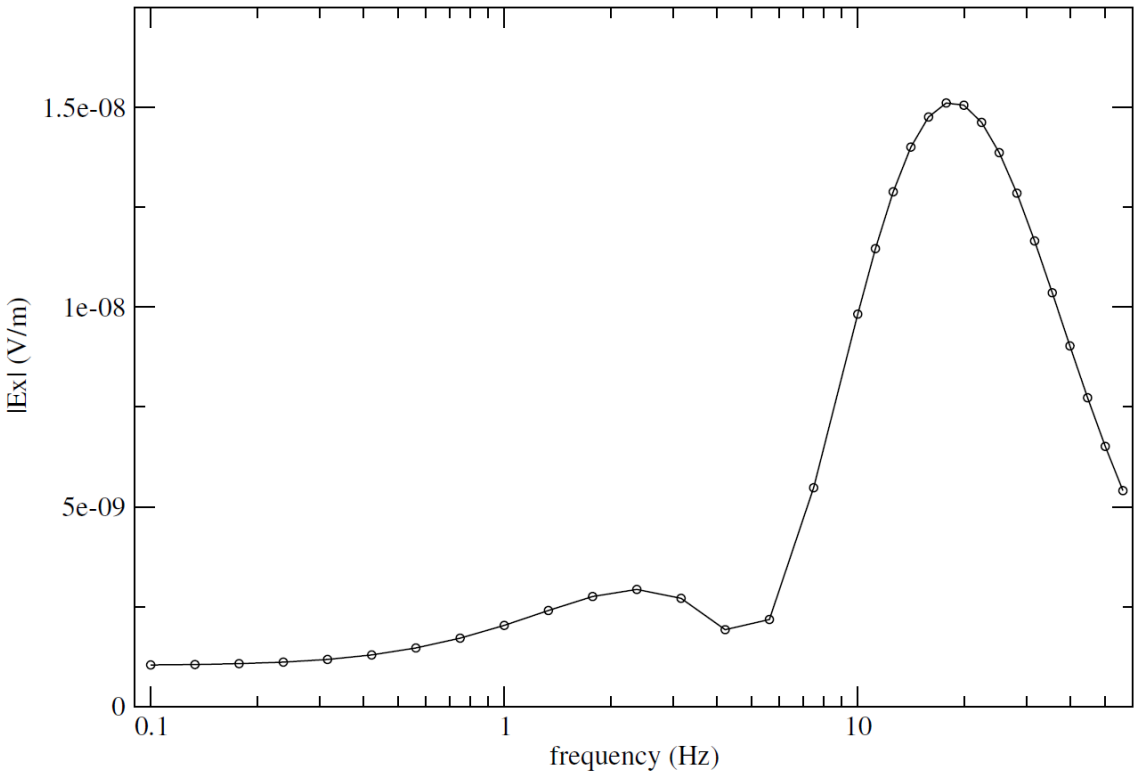

Figure IV-4 Frequency response of the casing. Reprinted with permission from Hickey et al. (2015b).

To simulate the injection of hydraulic fracture fluid the secondary potentials are found for a slab at a depth of 3150 m with a width of 70 m in the x-direction, length of 280 m in the y-direction, a thickness of 35 m, and a conductivity of 1.0 S/m. This represents the full extent of a fracturing stage. The resulting response at the surface is shown in Figure 5 and Figure 6, with and without the effect of the pipe casing, respectively. At this frequency, the casing increases the response of the injection by 2 orders of magnitude.

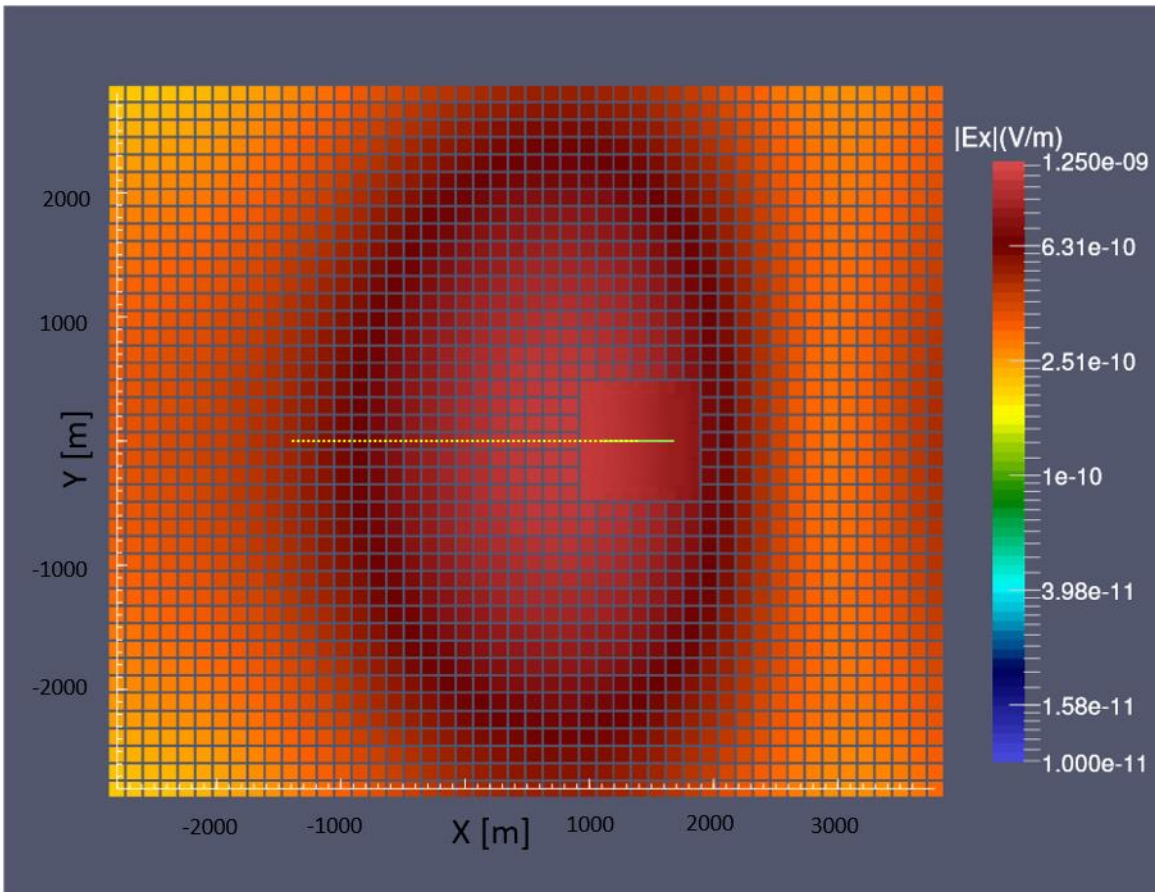

Figure IV-5 E_x amplitude plan view of the secondary response at the surface with casing as primary field. There is a higher node count centered on (1400,0) for the area of interest. The green line is the dipole source at the surface. The dotted yellow line is the spacing at depth. Modified with permission from Hickey et al. (2015b).

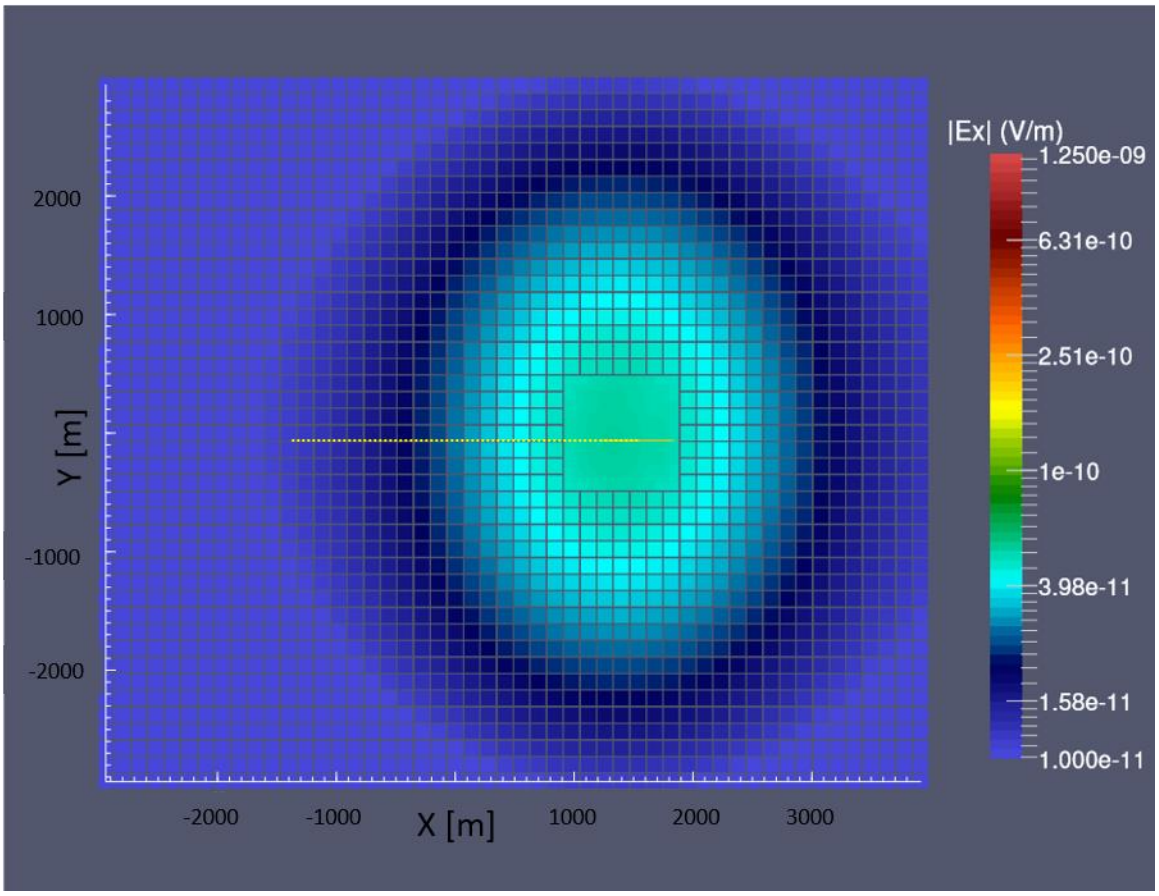

Figure IV-6 E_x amplitude plan view of the secondary response at the surface. There is a higher node count centered on (1400,0) for the area of interest. The green line is the dipole source at the surface. The dotted yellow line is the spacing at depth. Modified with permission from Hickey et al. (2015b).

The fracture versus background ratio is defined as:

$$FvBR = 100\% \left| \frac{Secondary\ Field}{Primary\ Field} \right| \qquad (4)$$

The corresponding FvBR plots are shown in Figure 7 and Figure 8, with and without the effect of the pipe casing, respectively. Note that in Figure 7 the Primary Field is the

summation of the field from the transmitter and the response of the pipe. At the location of our receivers the FvBR with the casing is of order magnitude 10^{-3} to 10^{-4} indicating the need for a monitoring system with -120 dB of signal to noise ratio (SNR) and at least 120 dB of dynamic range.

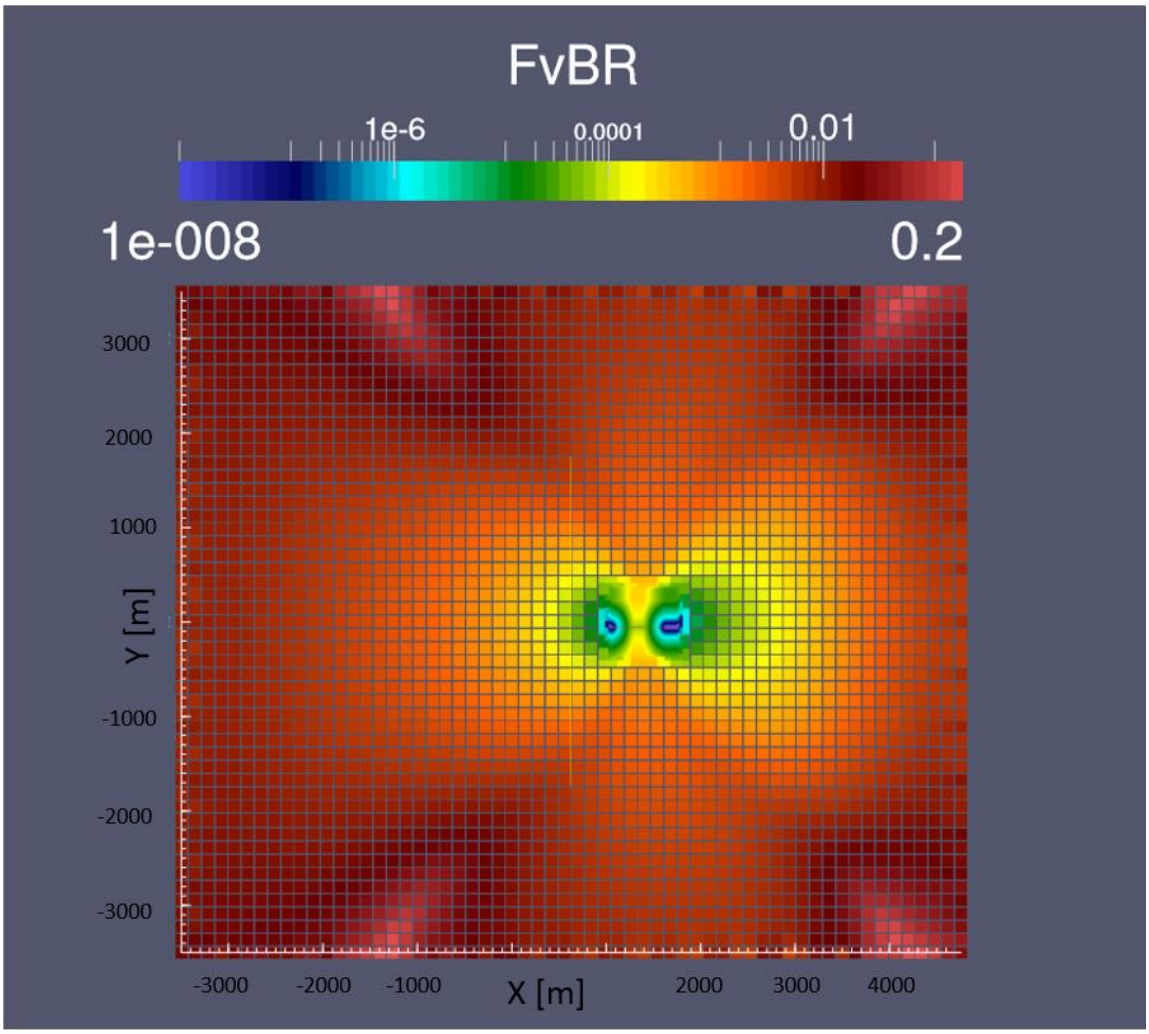

Figure IV-7 Fracture versus background ratio (FvBR) plan view at the surface with casing. Modified with permission from Hickey et al. (2015b).

Recorded versus Modeled Signal

In order to compare our modeled data to recorded data we calculated the normalized data error defined as,

$$NormE = 100\% \left| \frac{Observerved\ Data - Modeled\ Data}{Observed\ Data} \right|. \quad (5)$$

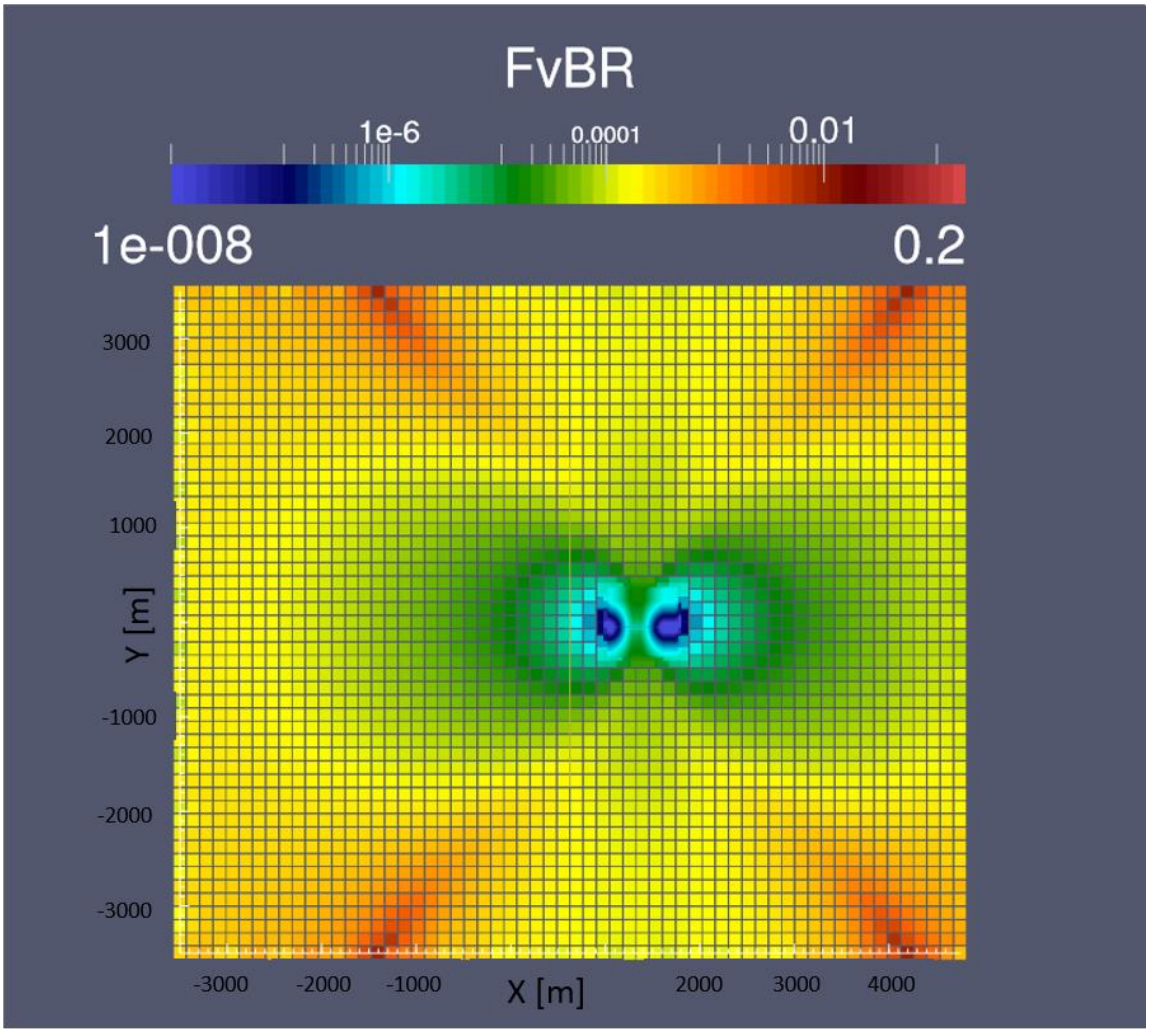

Figure IV-8 Fracture versus background ratio (FvBR) plan view at the surface with no casing. Modified with permission from Hickey et al. (2015b).

The site used for comparison is located in Karnes County, Texas and the transmitter/receiver layout for this location is shown in Figure 9. The transmitter is located directly above the lateral and a 300-meter transmitter line extends from each side of the transmitter along the surface. Receivers approximately 60m long are arranged parallel to the transmitter line. The first set of receivers closest to and on each side of the transmitter line are 45 meters away. The last set of receivers on each side of the transmitter line are located about 200m away. Data were taken prior to the frac to compare values of the total field with modeled data. For these observed data, at each receiver location, the data were stacked and an FFT was performed in order to find both the real and imaginary component of E_x at 17.8Hz and 28.2Hz.

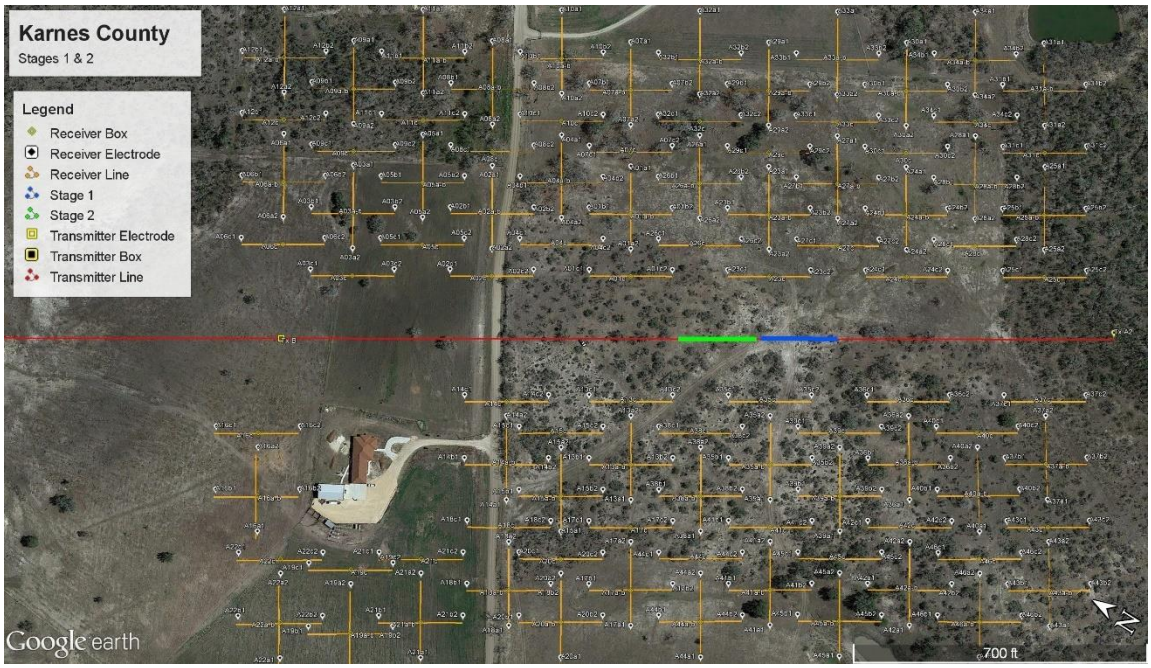

Figure IV-9 Transmitter and receiver layout for Karnes County. Reprinted with permission from Hickey et al. (2015b).

The observed data and modeled data, at each receiver location, were normalized by their respective currents and a frequency differencing (Maaø and Nguyen, 2010; Wirianto et al., 2011) was performed by subtracting the real and imaginary components of E_x at 28.2Hz from their respective values at 17.8Hz. A larger frequency, 28.2 Hz, is chosen with a skin depth above the order of the casing depth in order to simulate an air wave removal (Wirianto et al., 2011). Additionally, the observed data were normalized by antenna length. Then NormE was calculated at each receiver location by comparing the frequency differenced amplitude of E_x with the corresponding value at the closest modeling point. The location and NormE found at each receiver position are plotted in Figure 10 with the transmitter centered at y = 0 and running from 1100m to 1700m along

the x-axis. There is a gap in the lower left quadrant due to a house at the field location. The average NormE for the dataset was 55.8% ± 1.45%. There are a few points with larger NormE values which could be due to the receiver antenna not being perfectly aligned with the transmitter and picking up some of the E_y component. Additionally, the modeling data computes the E-field at a single point, while the real data is an average of about 60m (receiver antenna length) of E-field. A better understanding of the electromagnetic noise in the field will help with decreasing the error. The error can also be decreased by increasing the model complexity to better match the geologic conditions thereby creating a better numerical simulation.

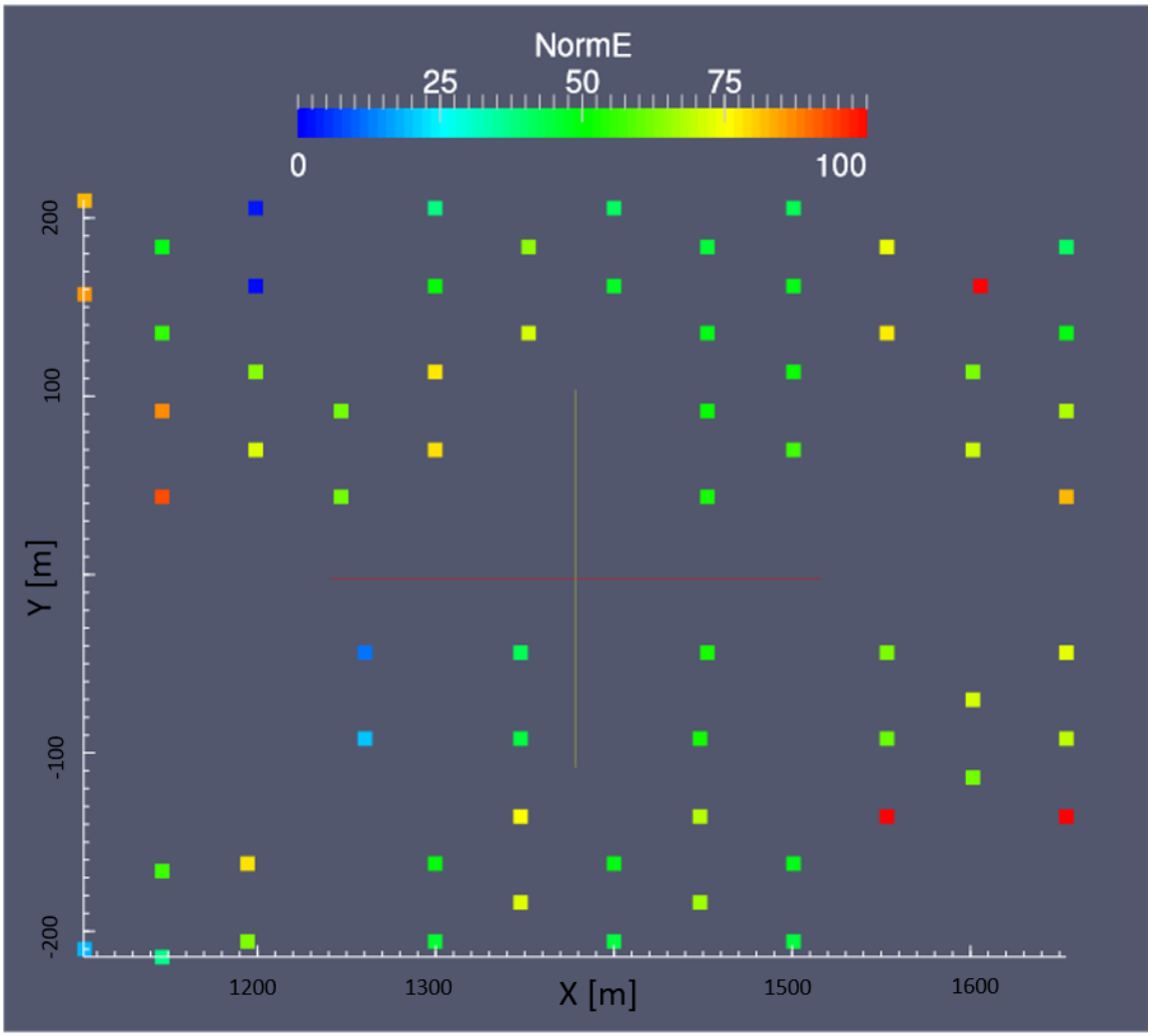

Figure IV-10 NormE values at each receiver location comparing model results versus field results. Modified with permission from Hickey et al. (2015b).

Hydraulic Fracture Monitoring

In the following section data are presented which is taken during one stage of a hydraulic fracturing operation at the Karnes County location shown in Fig 9. A broadband PRBS signal is transmitted and data from each receiver channel is processed to remove the transmitted signal and acquire a frequency dependent secondary response

that we presume to be due to changes in subsurface conductivity. The autocorrelation property of the PRBS signal allows alignment and deconvolution of the transmitted signal with the response measured at the receiver (Ziolkowski et al., 2011). One of the unique aspects of hydraulic fracture monitoring is that the fracturing starts at the known depth of the well casing and is expected to stay within the target formation. Therefore, changes in subsurface conductivities at a specific depth are expected to occur in a small frequency range.

To plot the presumed change in subsurface conductivities in time the data are processed in 64 second time steps. The frequency dependent response at each time step is then summed from 1Hz to 20Hz to represent the response as one value, R(t). Then the cumulative response, $R_c(T)$, at time T is defined as $\sum_{t=0}^{T} R(t)$. Figure 11 shows the labels of the layout used for interpretation. Figure 12 displays the cumulative secondary response at each receiver location at time step 10. Points between each receiver location are represented using a Delaunay 2-D triangulation. The black line, which for discussion assume runs from west to east, is the location of stage 1 with the toe end to the east. Initially, there is a small response towards the upper area near receiver 23c as well as near 35c and 36c. Then, Figure 13 displays the cumulative secondary response at time step 200 at the very end of the frac, representing the total extent of the fluid. In this case the extent of most of the fluid is about 60 meters north of the stage location near receiver 23b and 30 meters south of the stage location near receiver 35c. Additionally there seems to be a larger concentration of fluid to the right of the stage location near the toe

end. This may be due to the geology of the location or that this stage occurred at the end of the lateral.

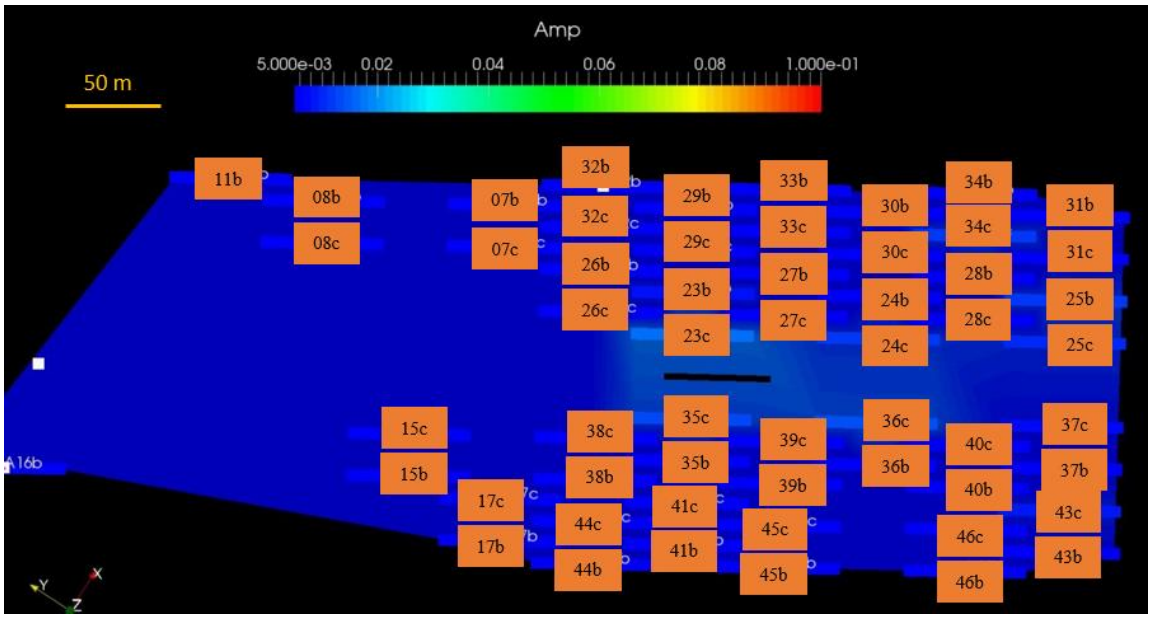

Figure IV-11 Plan view with location labels used for interpretation. Modified with permission from Hickey et al. (2015b).

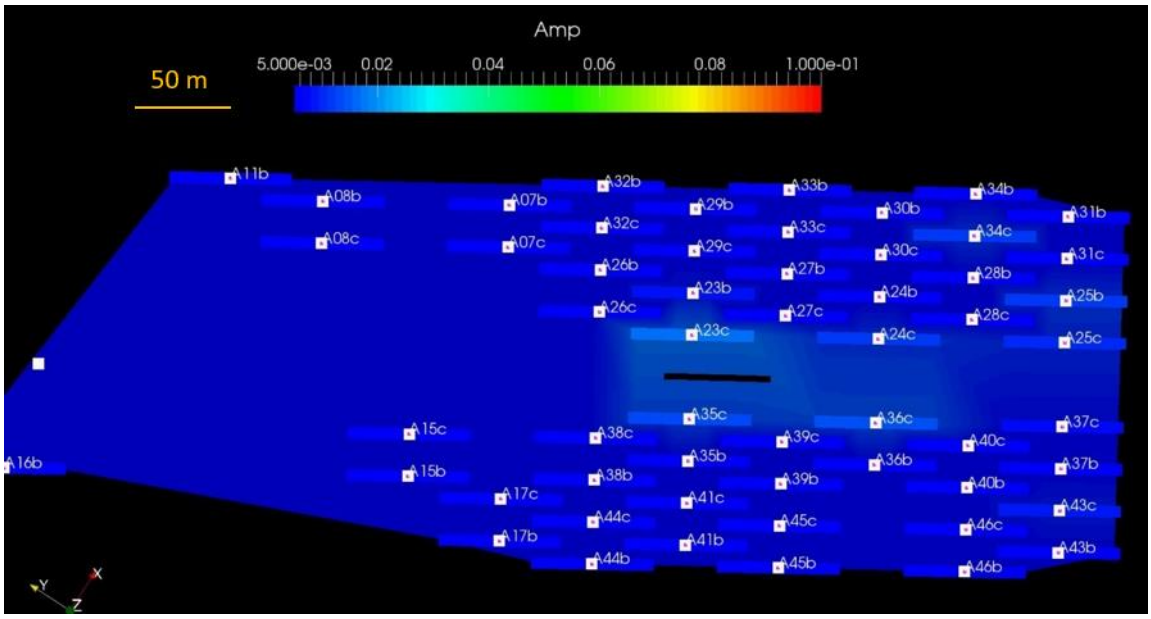

Figure IV-12 Hydraulic fracture monitoring: time step 10. Modified with permission from Hickey et al. (2015b).

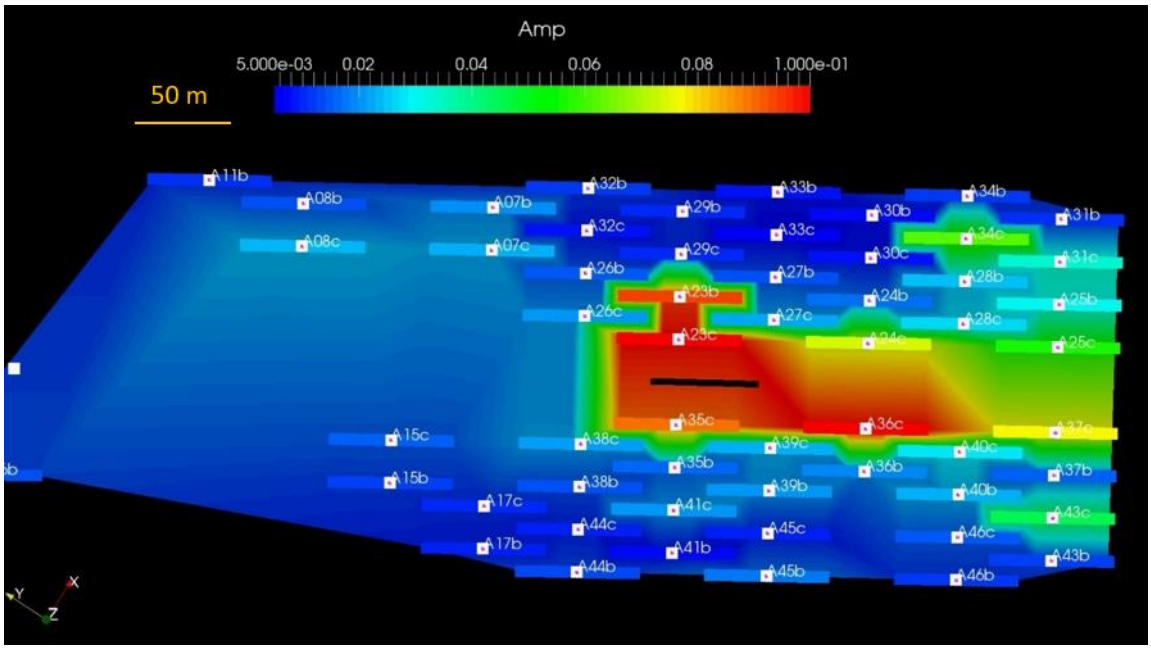

Figure IV-13 Hydraulic fracture monitoring: time step 200. Modified with permission from Hickey et al. (2015b).

Summary

In summary, we have shown that in order to detect the response due to the injection of hydraulic fracturing fluid the FvBR indicates a CSEM system needs -120 dB of signal to noise ratio (SNR) and at least 120 dB of dynamic range. The normalized data error calculation, NormE, has shown that our modeled values for the primary field are within a 55% error of our measured values. Finally, a case study in Karnes County, Texas has explored the possibility of using a ground-based CSEM system to detect changes in the subsurface due to hydraulic fluid injection and measure the extent of the fluid.

CHAPTER V

MONITORING HYDRAULIC FRACTURING FLUID MOVEMENT USING GROUND-BASED ELECTROMAGNETICS, WITH APPLICATIONS TO THE ANADARKO BASIN AND THE DELAWARE BASIN / NW SHELF*

Overview

Hydraulic fracturing provides the petroleum industry with unconventional means for extracting hydrocarbons, but the method can be made more efficient to enable better production by answering some not so simple questions: where did the injection fluid go and how much of the volume was propped? Ground-based controlled source electromagnetics (CSEM) may provide a means to generate, record, and interpret electromagnetic signals responding to temporal changes in the subsurface electrical conductivity, using instruments deployed on the surface. Since the injection of fluid into rock for hydraulic fracturing alters the conductivity of the formation in the vicinity of the wellbore, CSEM is a geophysical technique that is well-suited for monitoring completions. In this paper we show results from two CSEM surveys. The first CSEM survey acquired data from the Anadarko basin during hydraulic fracture operations from a lateral well while the second CSEM survey is based on data obtained during the completions of a vertical well in the Delaware basin/ Northwest shelf. Both of the surveys provided unique challenges. The data interpretations from each survey help to

* Part of this chapter is modified with permission from "Monitoring Hydraulic Fracturing Fluid Movement Using Ground-Based Controlled-Source Electromagnetics (CSEM), With Applications to the Anadarko Basin and the Delaware Basin NW Shelf" by Hickey, M. S., Treviño III, S., & Everett, M. E., 2017. Proceedings of the 5th Unconventional Resources Technology Conference, 2017, pp. 2472-2483, Copyright [2017] by Unconventional Resources Technology Conference (URTeC).

influence future completion strategies by providing valuable information to the well development teams, for example fracture asymmetry, fracture half lengths, and unexpected fracture behavior.

Introduction

Ground-based controlled-source electromagnetics (CSEM) is an emerging geophysical technique that is under development as a means to monitor the movement and extent of injection fluid during hydraulic fracture operations (Hickey et al., 2015; Hickey et al., 2015b). The electromagnetic response of a conductive zone containing fluid to its energization by a surface-deployed CSEM source is dependent upon the electrical conductivity difference between the fluid-rich zone and the background geological formation (Badea et al., 2001). The fact that CSEM is sensitive to the electrical conductivity of the fluid allows properties such as hydraulic fracture half-length and fracture asymmetry to be studied dynamically, provided the signal to noise ratio of the recorded data is sufficient. Additionally, it has been shown that the presence of a steel well casing increases the sensitivity to deep targets (Patzer et al., 2017; Puzyrev et al., 2017). The steel casing acts as a source at target depth due to the inductive coupling to the primary source on the surface. We now present two case studies, the first involving a horizontal well in the Anadarko Basin and the second involving a vertical well in the Delaware basin Northwest shelf.

Modeling

In order to characterize the expected CSEM response of an anomalously conductive target we use 3-D CSEM finite-element forward modeling (Hickey et al., 2015; Hickey et al., 2015b; Badea et al., 2001). The governing Maxwell's equations are solved in the frequency domain for the response of a secondary set of EM potentials ($\mathbf{A}_s$, Ψ_s) with conductivity structure $\sigma_s(r)$, herein representing zones containing frac fluid, by first specifying a set of known electromagnetic (EM) primary potentials ($\mathbf{A}_p$, Ψ_p) as the response to a background conductivity structure $\sigma_p(\mathbf{r})$, i.e. the response produced by the interaction of the transmitted signal with the underlying geologic structure. Analysis of the expected "secondary" response in the presence of the frac fluid aids in survey layout design and interpretation. As an example, consider a modeling domain of dimensions 17.2 km× 17.2 km × 19 km. The model comprises a half-space background conductivity of 0.01 S/m and a conductive target at depth 3080 m with a width of 140 m in the x-direction, 280 m in the y-direction and thickness of 35 m. A 60 A, 600 m long x-directed horizontal dipole is placed at the surface (z = 0.0 m) and centered at the origin. For a receiver also on the surface located at x =140 m and y = 140 m, Figure 1 shows how the magnitude of the x-component of the Electric field changes as target conductivity (measured in S/m) changes. The target at depth is near the toe end of the well. Examples focus on the toe-end because those are the locations where the initial field data are in. The field data are in these locations because the pad is usually the most electromagnetically noisy area of the operation and the toe end is the end furthest away..

Additionally, it can be shown that the frequency at which the Electric field amplitude attains its maximum shifts with target depth.

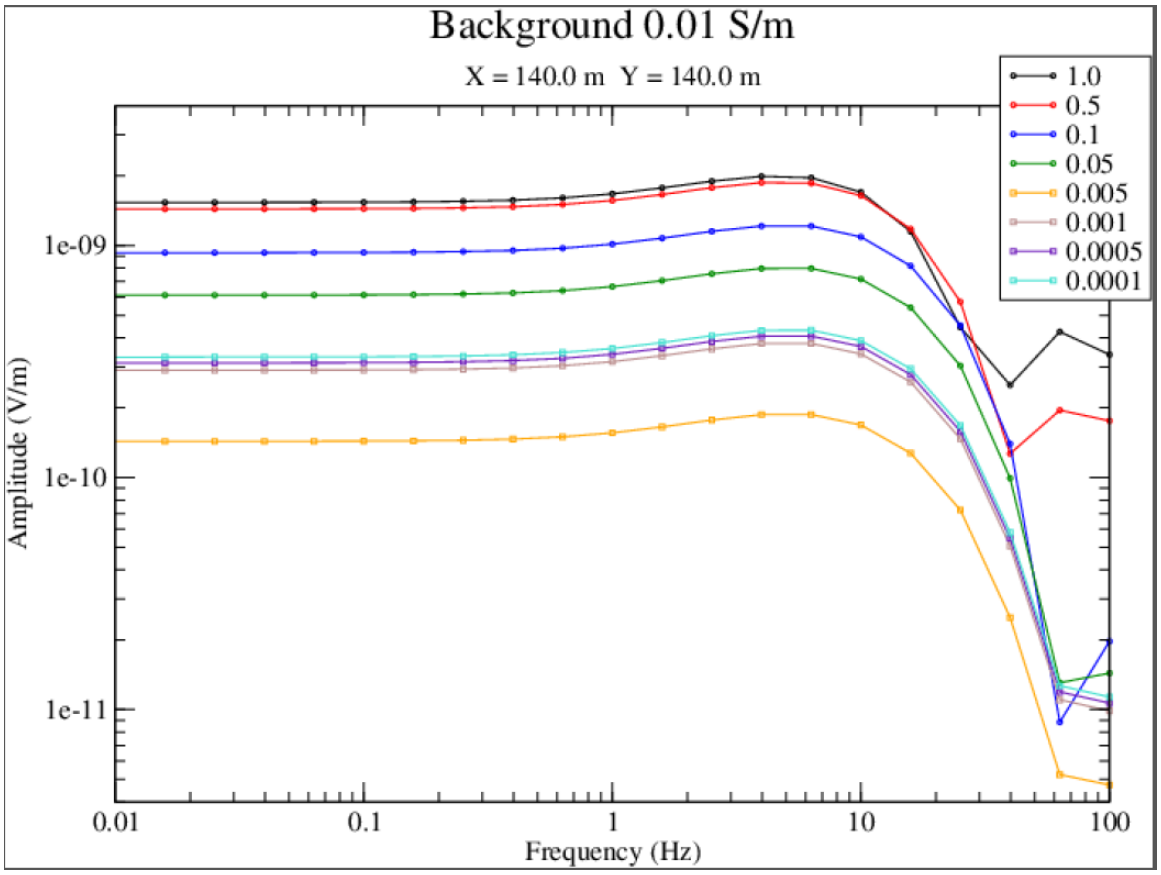

Figure V-1 Frequency response of the amplitude of the x-component of the Electric field as target conductivity [S/m] changes. Reprinted with permission from Hickey et al. (2017).

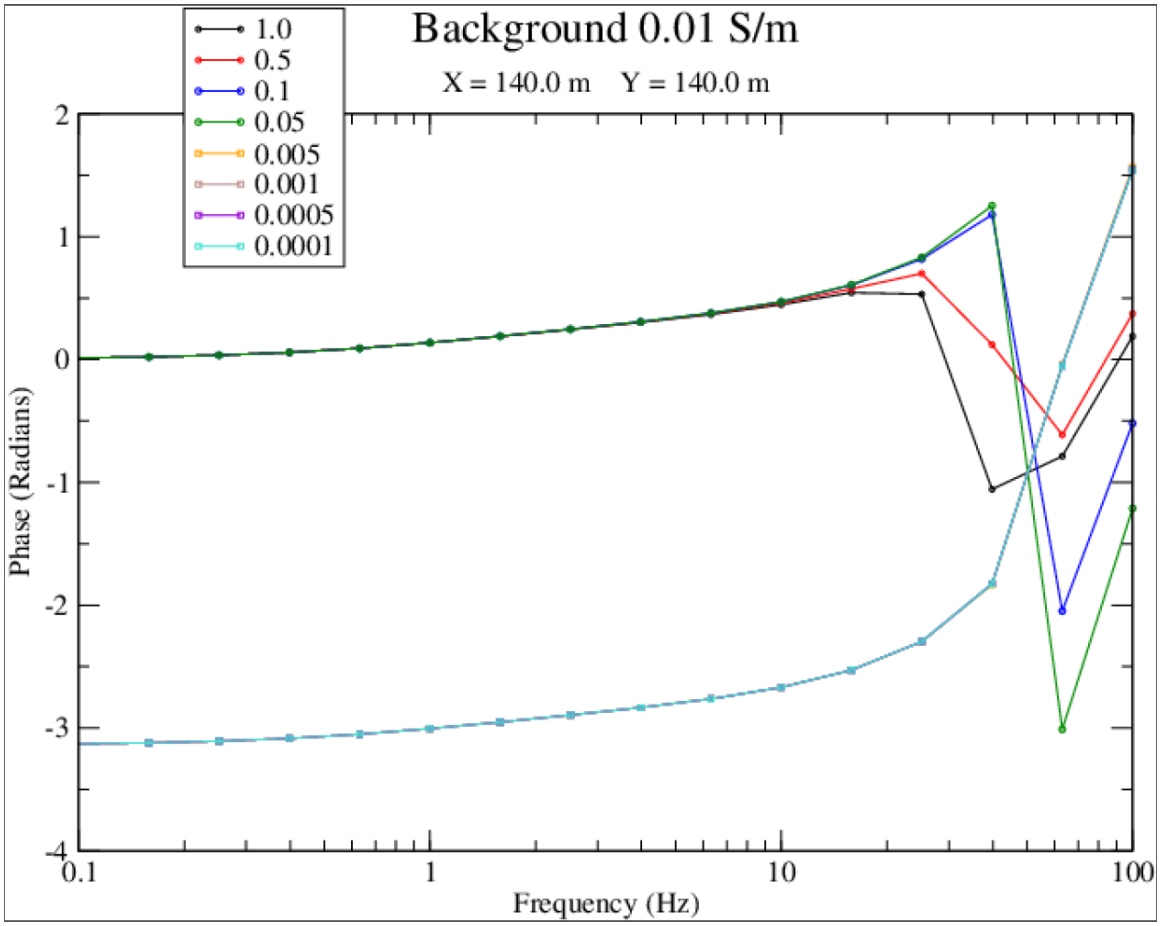

Figure V-2 Frequency response of the phase of the x-component of the Electric field as target conductivity [S/m] changes. Reprinted with permission from Hickey et al. (2017).

Field Methodology and Data Processing

A typical layout of the receiver array and the grounded-dipole transmitter for hydraulic fracture monitoring is displayed in Figures 3 and 4. The transmitter dipole of length 600 m runs parallel to, and lies on the surface directly above, the lateral well. Figure 4 is a close-up of a portion of the layout that shows the electric-dipole receivers, including their electrode pairs and control boxes. Receivers are placed on each side of the lateral with the receiver electrode pairs arranged parallel and perpendicular to the

transmitter line. Each receiver is able to record on multiple channels simultaneously, with the recorded signal from each receiver electrode-pair being treated as a separate datum. Receiver electrode separation distances are typically 30 m.

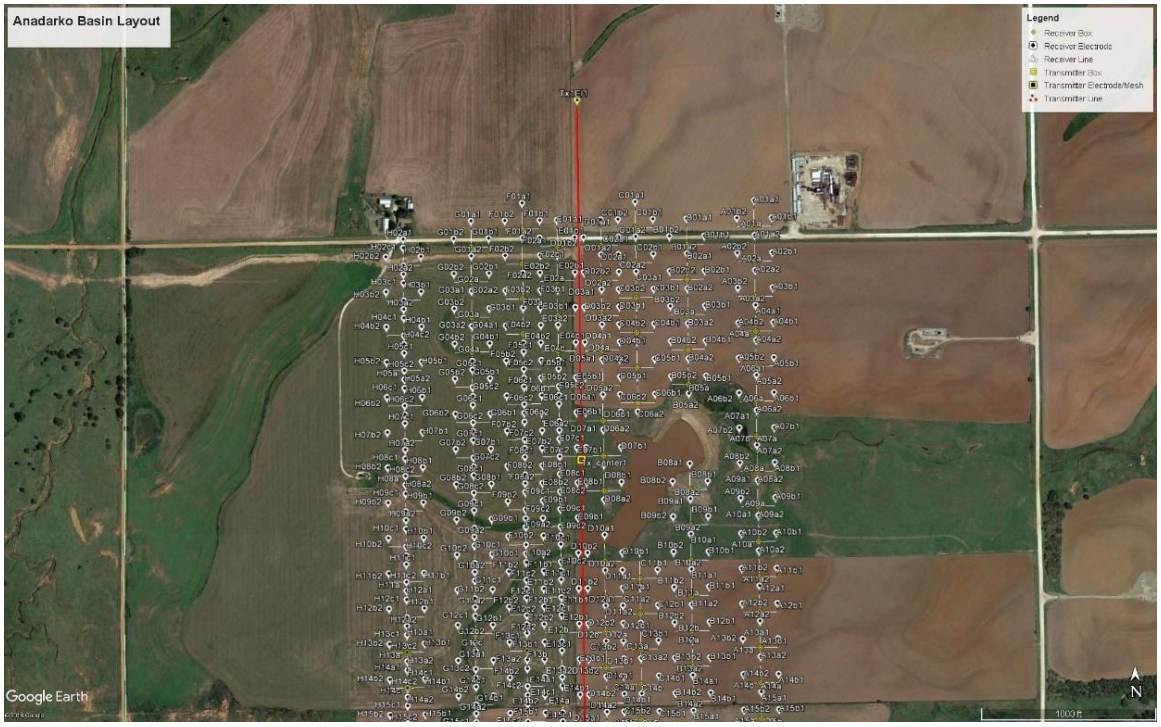

Figure V-3 Figure 2: Anadarko Basin Layout. Receivers are placed symmetrically on each side of the transmitter line. Reprinted with permission from Hickey et al. (2017).

Figure V-4 A zoomed in version to show the perpendicular and parallel components. Reprinted with permission from Hickey et al. (2017).

After electric-field data are collected from a receiver, the dataset is processed, transformed into the frequency domain, and then subtracted from the background, pre-frac response. This results in a signal that is presumed to represent the response due to the fluid injection, assuming that no other changes to subsurface electrical conductivity or systematic variations of the background electromagnetic environment are present. Under this criticial assumption, depending on the amount of fluid being injected and the depth of injection, the amplitude of the response is enhanced over a certain frequency range. The amplitudes from a selected frequency range are summed and the resulting aggregate signal is displayed in plan view for interpretation. A threshold for noise is determined based on the number of frequencies summed and the background noise at the

site location. A signal is considered significant if its peak strength is about 2 orders of magnitude larger than the background pre-frac signal at the same location.

Case Study 1: Anadarko Basin

For the first case study, CSEM data were acquired directly above the toe end of a horizontal wellbore in the Anadarko Basin. In this case the standard layout shown in Figure 3 was used. The results from stage-2 operations, which was the first stage electromagnetically monitored, are presented as contour maps in figures 5 and 6. Figure 5 shows the initial response at the beginning of the fracture operation. Note that each datum displayed is the aggregate response, summed over a selected frequency range, of the transmitter-parallel component of the electric field recorded at the receiver location. The response shown in the areas between receivers is the value interpolated from responses measured at nearby receivers. Initially the largest response appears to the NW of the stage location. Figure 6 shows the fracture-related CSEM response at the final time step, i.e. at the end of the stage operation, where the largest response appears to the SE. From these Stage-2 CSEM results, assuming that the signal arises from subsurface conductivity changes and not other causes, the half-length of the hydraulic fracture can be estimated and, although in this case the largest hydraulic fracture-induced CSEM signals appear on different sides of the well at different times, the azimuth of a line joining them provides important information about the geometry of the fluid injection pathways. The general area and direction of the fracture signals are represented by

ellipses and arrows to enable a comparison with CSEM responses measured during later stages.

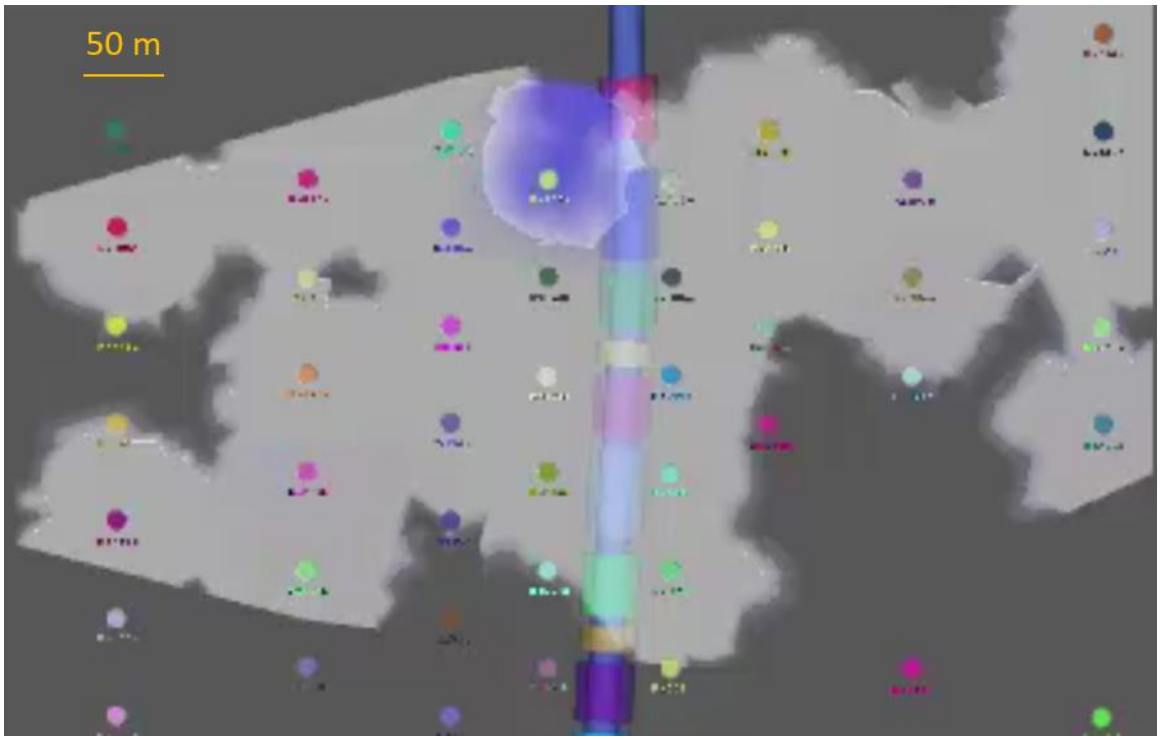

Figure V-5 Plan view of stage 2 relative change in signal at the beginning of the stage. Blue represents signal change from background. Light grey is the background. Dark grey is no data. Modified with permission from Hickey et al. (2017).

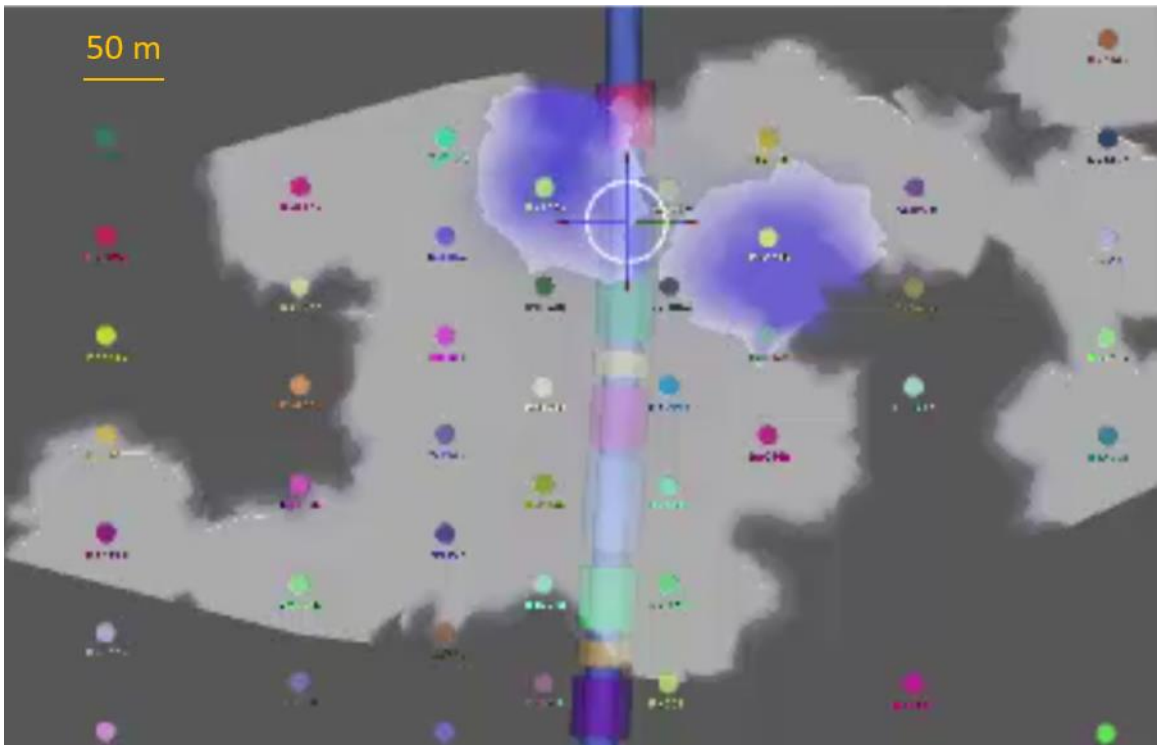

Figure V-6 Plan view of stage 2 relative change in signal at the end of the stage. Blue represents signal change from background. Light grey is the background. Dark grey is no data. Modified with permission from Hickey et al. (2017).

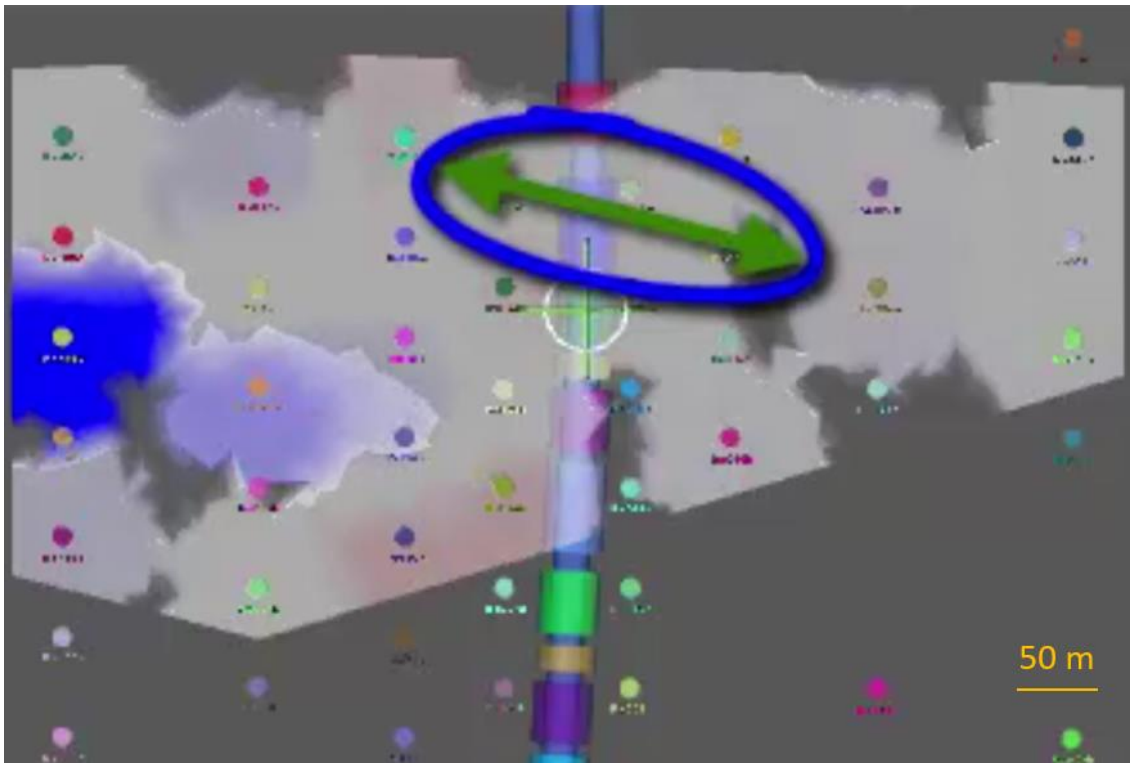

Figure V-7 Plan view of stage 3 relative change in signal at the beginning of the stage. Blue represents signal change from background. Light grey is the background. Dark grey is no data. Stage 2 final extent and azimuth are shown for comparison. Modified with permission from Hickey et al. (2017).

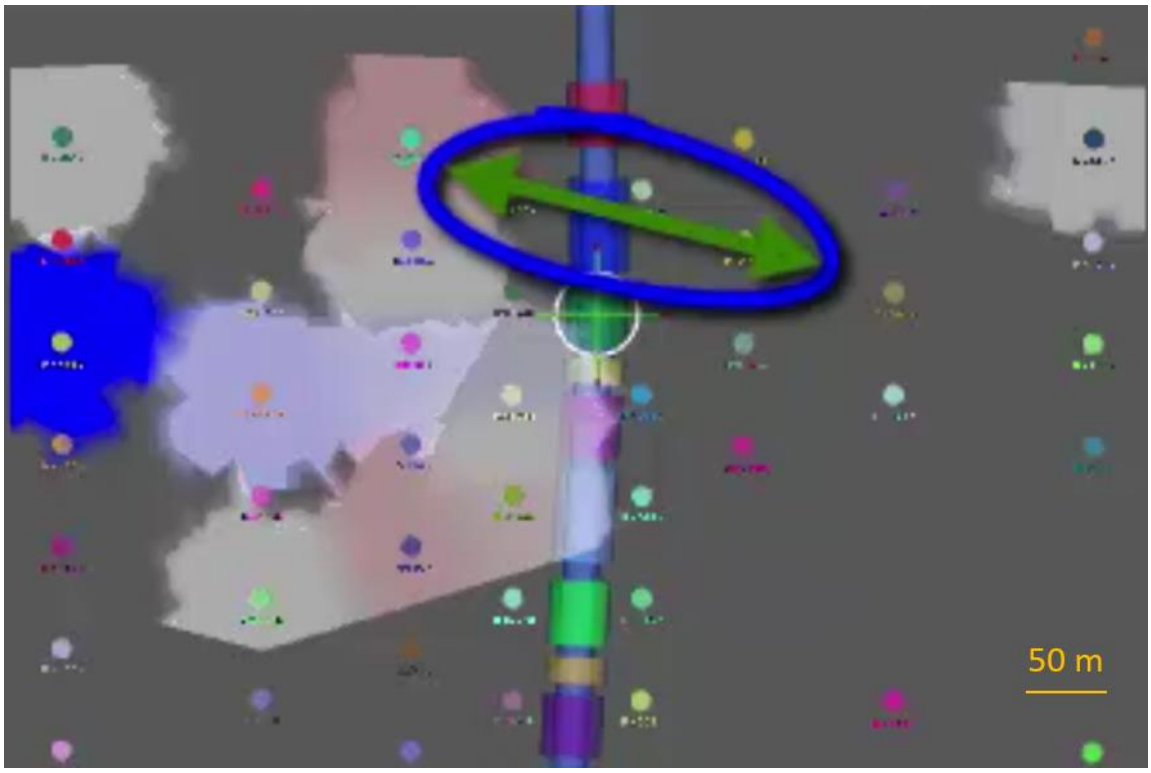

Figure V-8 Plan view of stage 3 relative change in signal at the end of the stage. Blue represents signal change from background. Light grey is the background. Dark grey is no data. Stage 2 final extent and azimuth are shown for comparison. Modified with permission from Hickey et al. (2017).

The CSEM responses from the stage-3 operations are shown in Figures 7 and 8. In this case, the initial signal shown in Figure 7 and the final signal shown in Figure 8 are similar. Contrary to the stage-2 results, there is not a large increase in signal after the initial time step, and the pattern of the CSEM response from this stage is asymmetric about the wellbore. Additionally, the largest CSEM response is found at greater distance from the well than the largest responses observed during the stage-2 operations. Assuming that the changes in CSEM response are caused by changes in subsurface conductivity and not some other cause, the great distance at which the largest CSEM

response occurs indicates that a larger hydraulic fracture half-length was created in this stage relative to the previous one.

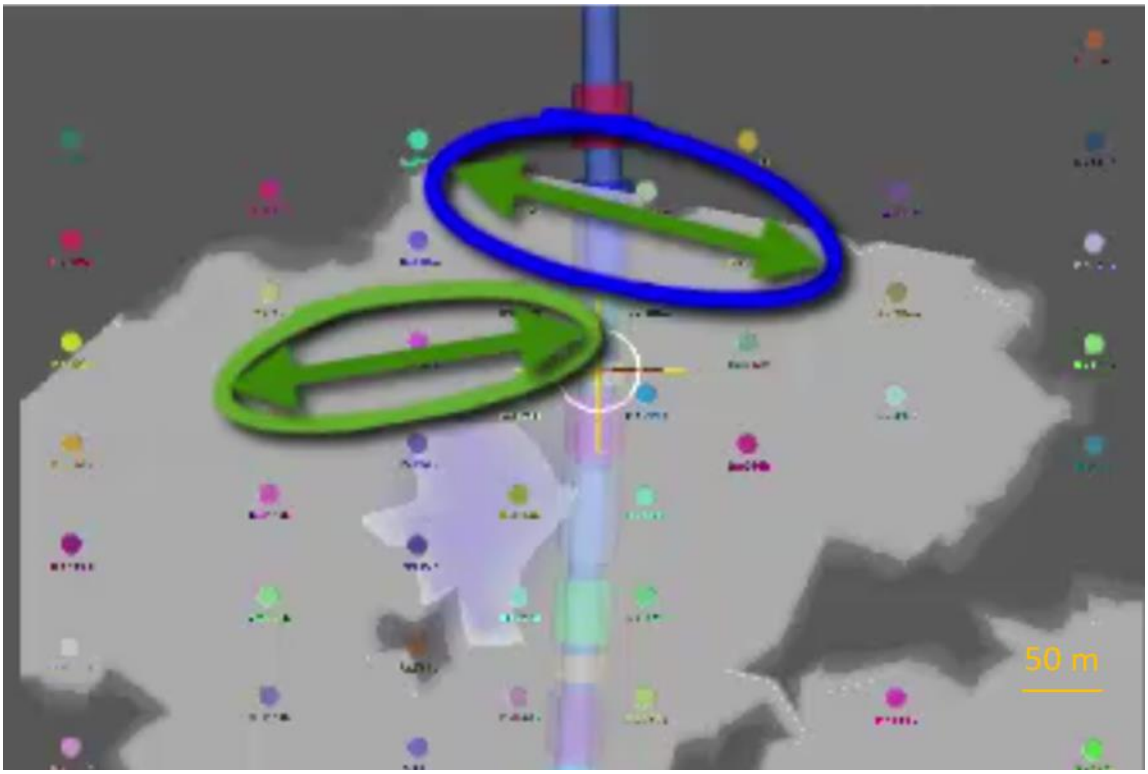

Figure V-9 Plan view of stage 4 relative change in signal at the beginning of the stage. Blue represents signal change from background. Light grey is the background. Dark grey is no data. Stages 2 & 3 final extents and azimuths are shown for comparison. Modified with permission from Hickey et al. (2017).

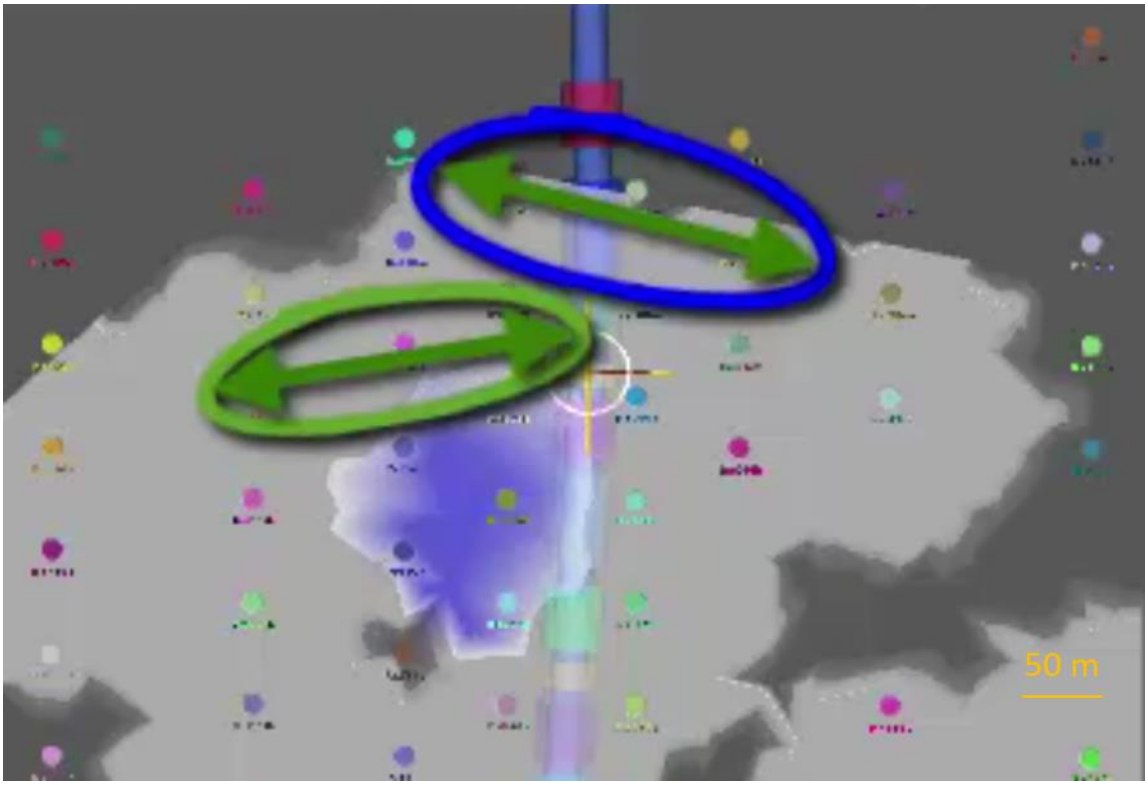

Figure V-10 Plan view of stage 4 relative change in signal at the end of the stage. Blue represents signal change from background. Light grey is the background. Dark grey is no data. Stages 2 and 3 final extents and azimuths are shown for comparison. Modified with permission from Hickey et al. (2017).

The Stage-4 operation is different from previous stages in that it had fewer perforation clusters and was confined to a smaller length along the lateral. The CSEM responses are shown in Figures 9 and 10 with similar results to the stage-3 operation. An appreciable CSEM signal appears on only one side of the wellbore. Additionally, the fracture half-length is similar to that created during the stage-2 operation.

Case Study 2: Delaware Basin / Northwest Shelf

This case study is atypical of our past hydraulic fracture monitoring experience in unconventional settings in that the fluid injection wellbore is vertical. Consequently, the transmitter and receivers are placed on and/or close to the well pad, as shown in Figure 11. The main difficulty from a CSEM monitoring standpoint about this configuration is the large amount of electromagnetic noise that is generated by oilfield infrastructure and associated operations on the pad. Unfortunately, the noise level at some of the receivers proved excessively high and information acquired by these receivers has been removed from the dataset. Fortunately, the data from the remaining receivers are useful. The response at these receivers from hydraulic fracture fluid movement is presumed to manifest as change of CSEM signal over time that is distinguishable from the environmental noise. This assumption requires careful consideration as environmental noise at oilfields is poorly understood at the present time. Another aspect of this case study is the target structure. The target structure in this case is a carbonate with inherent natural fractures. The natural fractures should induce a larger fracture network. For the interpretation of these data, the signal was represented across a large frequency band, with each group of frequencies responding to a different aspect of the fluid movement. Instead of summing across the entire active bandwidth, for each stage we show for the 2D display only the most active frequency bands. Also, since the stages occurred at different depths, the active frequency bands were different at each stage. This is why different stages generate diagnostic CSEM responses over different frequency bands. The results from two stages are now discussed.

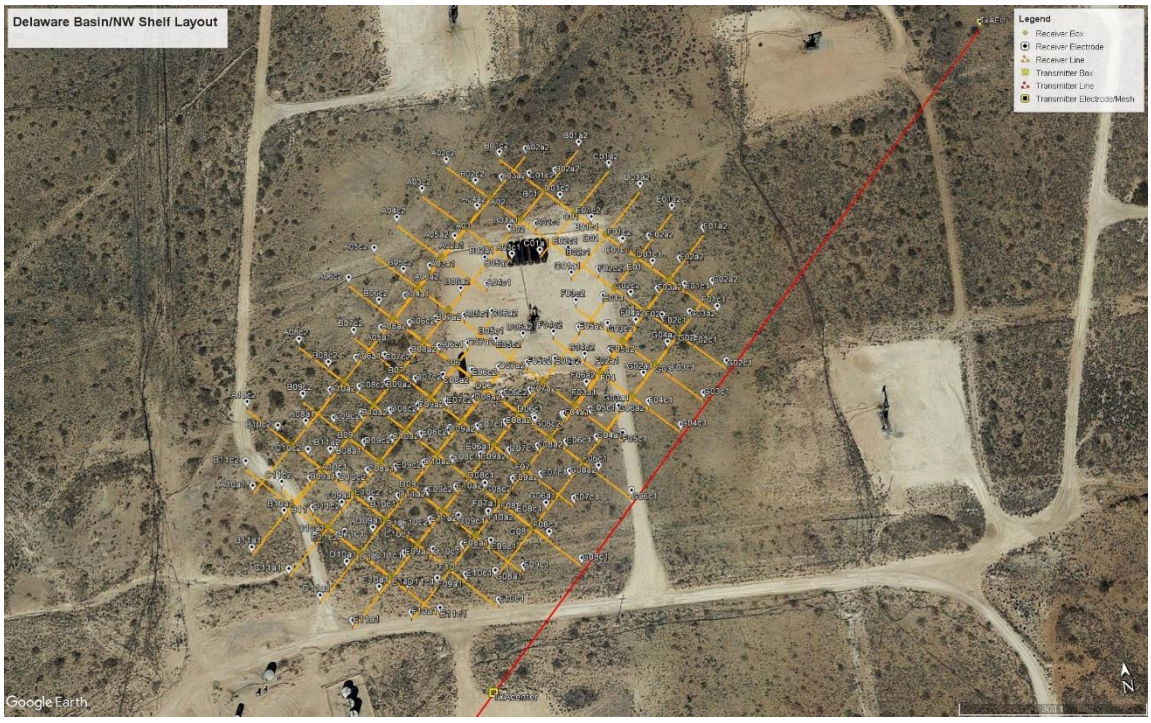

Figure V-11 Delaware Basin / NW Shelf Layout. Reprinted with permission from Hickey et al. (2017).

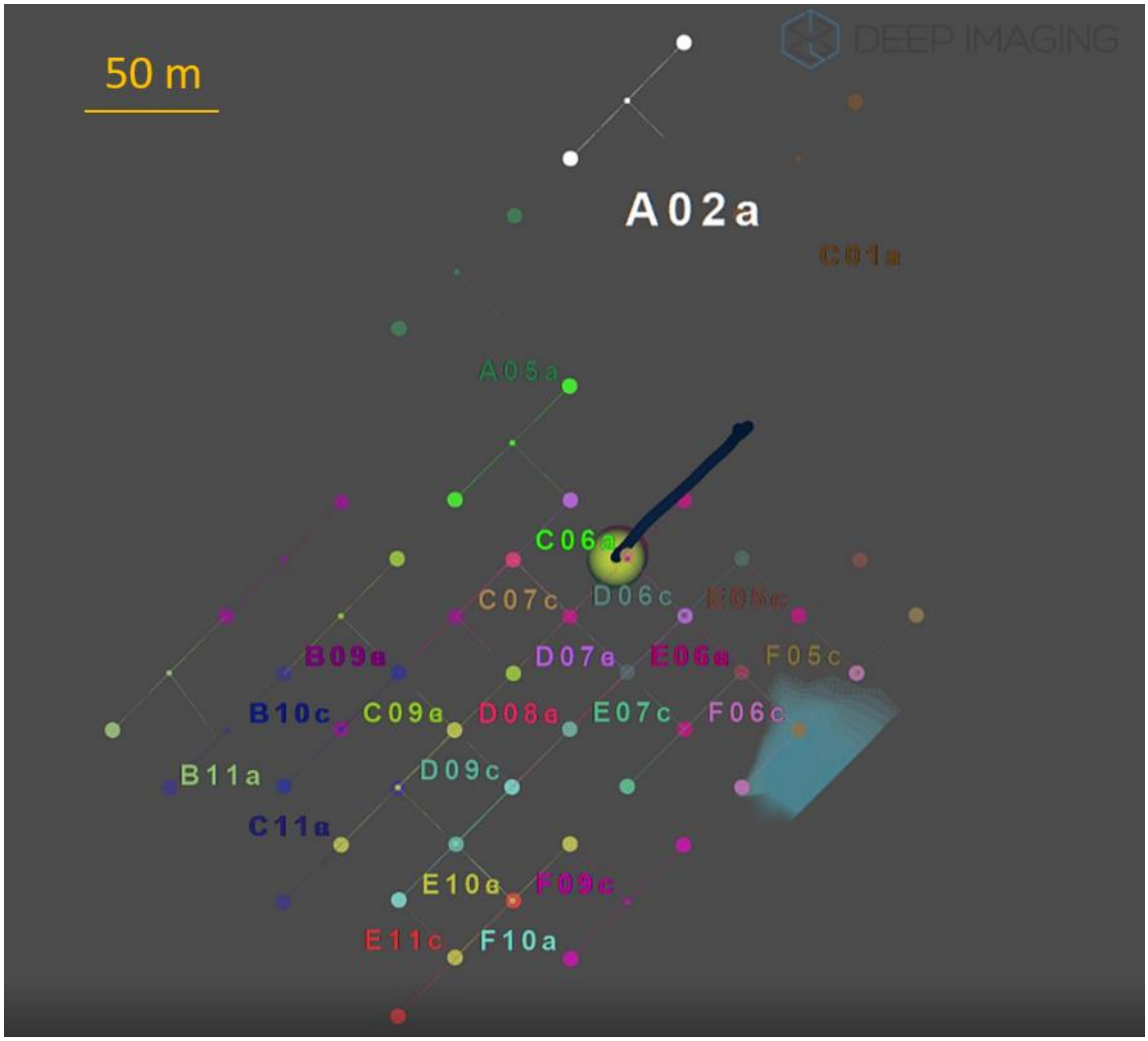

Figure V-12 Plan view of stage 1 relative change in signal before the beginning of the stage. Blue represents signal change from background. Modified with permission from Hickey et al. (2017).

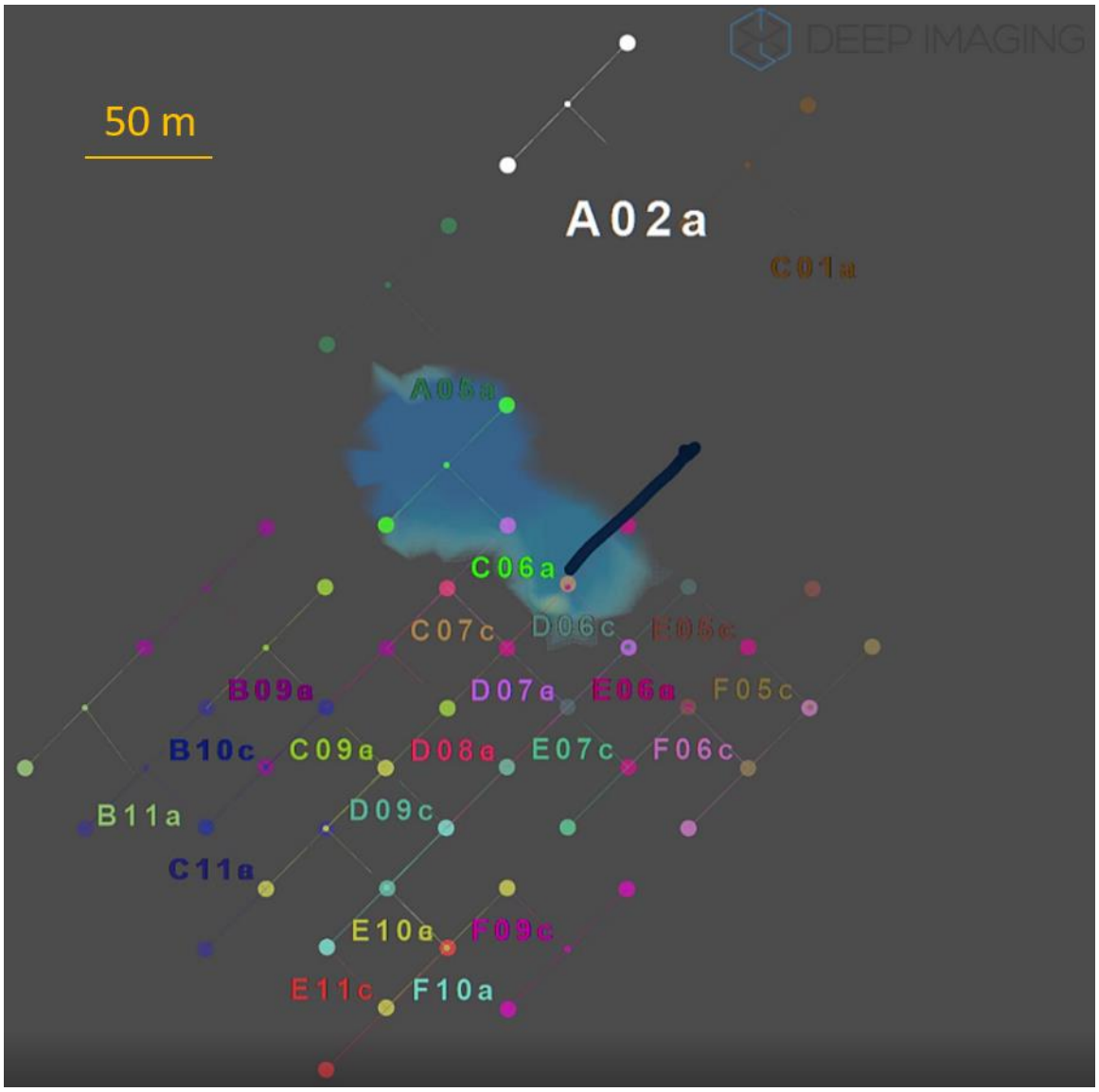

Figure V-13 Plan view of stage 1 relative change in signal at the beginning of the stage. Blue represents signal change from background. Modified with permission from Hickey et al. (2017).

The CSEM signals from stage-1 operations are shown in Figures 12 and 13. The signal amplitudes from the frequency range 29-30 Hz have been summed to produce the aggregate signal shown in the figures. Figure 12 shows the background CSEM response prior to the beginning of the frac operation. The signal at this time is most likely due to

the operations noise from the pad. As shown in figures 13, 14 and 15, as the stage progresses, this signal disappears. Figure 13 shows that the zone of greatest response appears initially to the NW of the wellbore. This direction is aligned against the expected stress-direction pattern that was provided to us by the client. In Figure 14, which corresponds to ~10 minutes from the beginning of the frac operation, the signal builds to the west. The final snapshot in Figure 15 shows the CSEM-response as an indicator of the culminating fluid and proppant distribution, subject to the aforementioned caveat that the response is indicative of changes in subsurface conductivity and not some other cause. Note that the lack of usable receiver data to the NE of the wellbore, and on the pad itself, prevents a reliable interpretation of the progress of injected fluid in that direction.

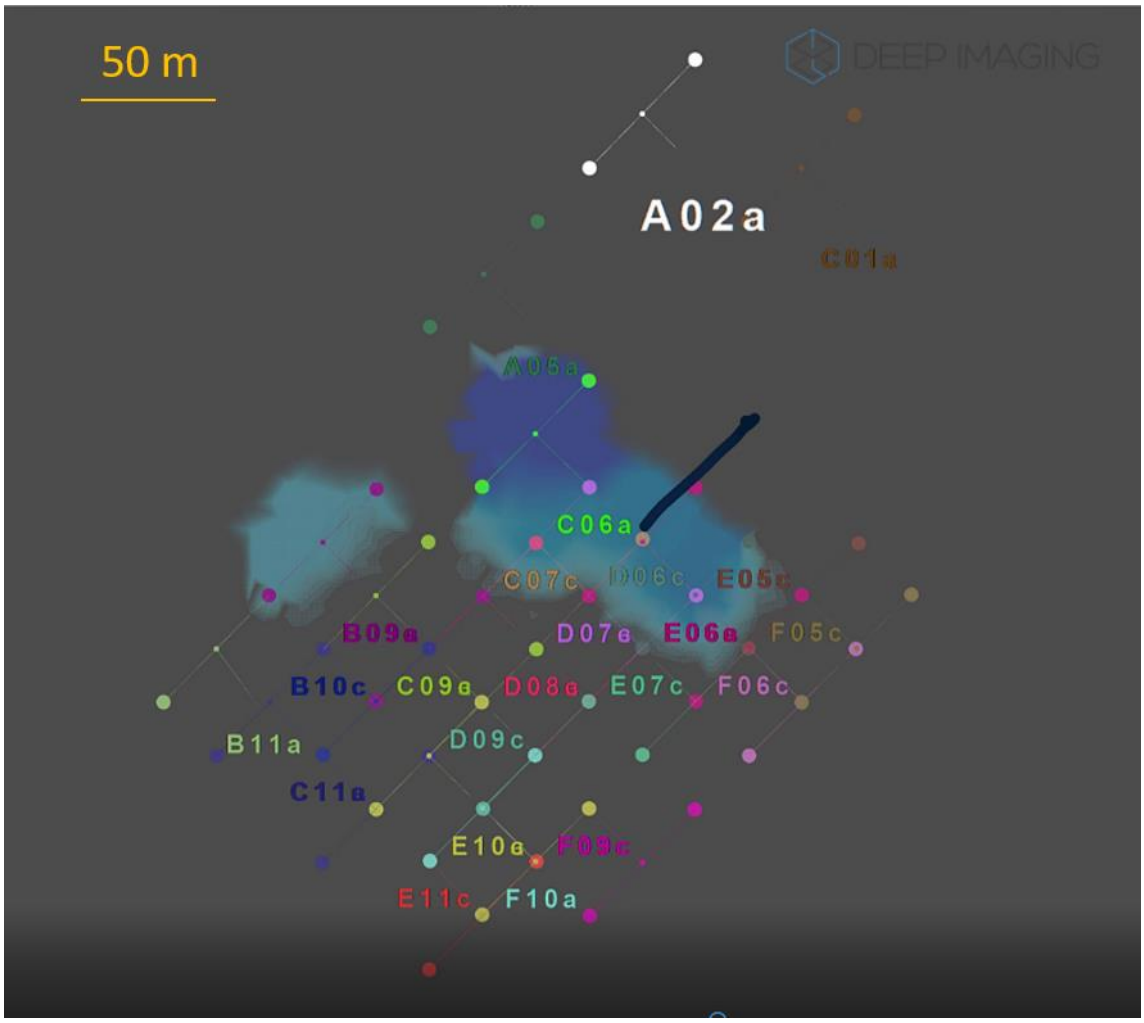

Figure V-14 Plan view of stage 1 relative change in signal at the middle time of the stage. Blue represents signal change from background. Modified with permission from Hickey et al. (2017).

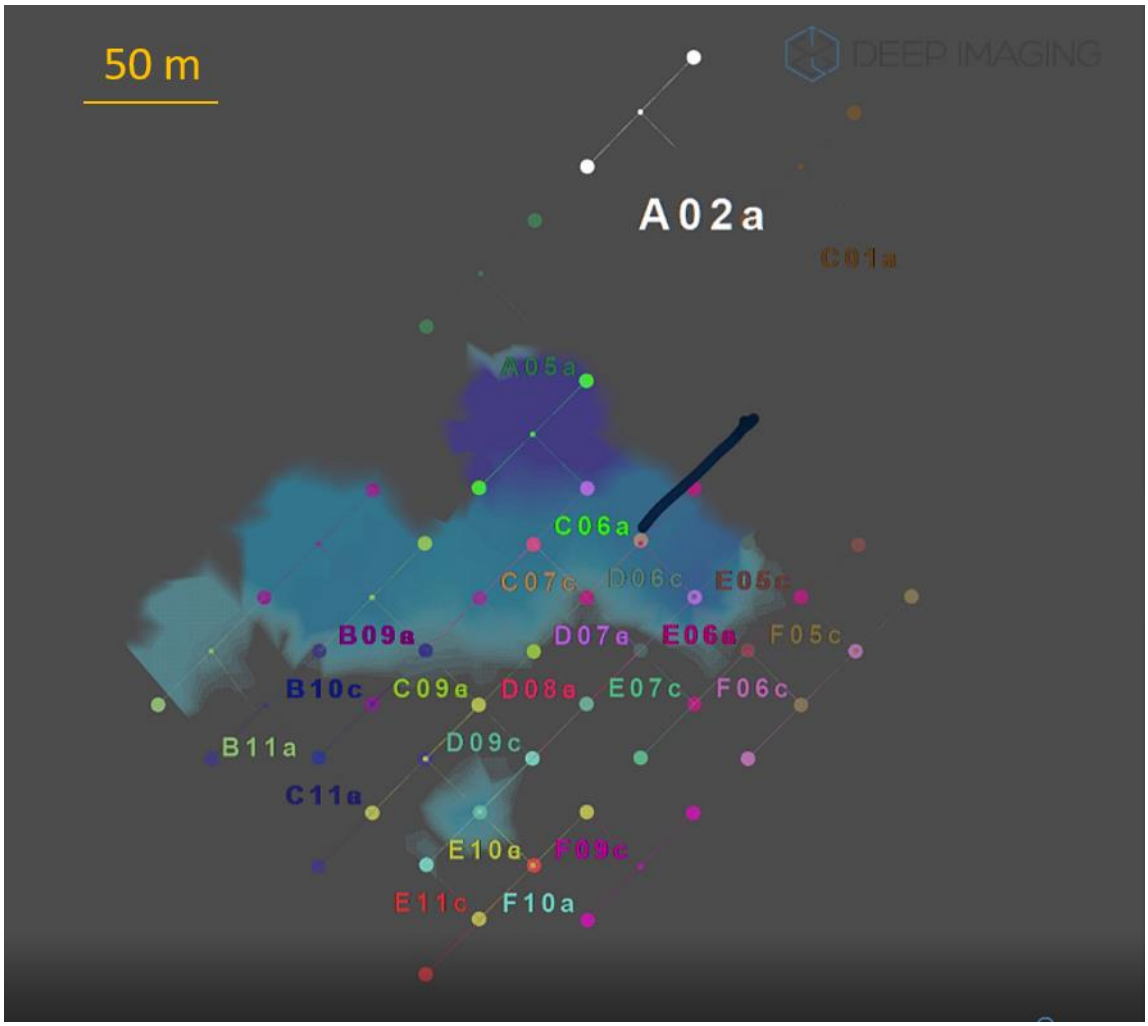

Figure V-15 Plan view of stage 1 relative change in signal at the end of the stage. Blue represents signal change from background. Modified with permission from Hickey et al. (2017).

For the deeper stage-2 operation at this site, CSEM signals were summed in the lower frequency range 11-12 Hz and the results are shown in Figure 16 and 17. For operations at this stage, as in the previous stage, data from some of the receivers located near the pad were removed due to excessive noise levels. Figure 16 shows the regions where the largest CSEM signals are observed before the end of the hydraulic fracture.

Figure 17 shows a post-frac image wherein it is noted the signal has dropped significantly. This result is interpreted as poor proppant placement into the formation around the wellbore.

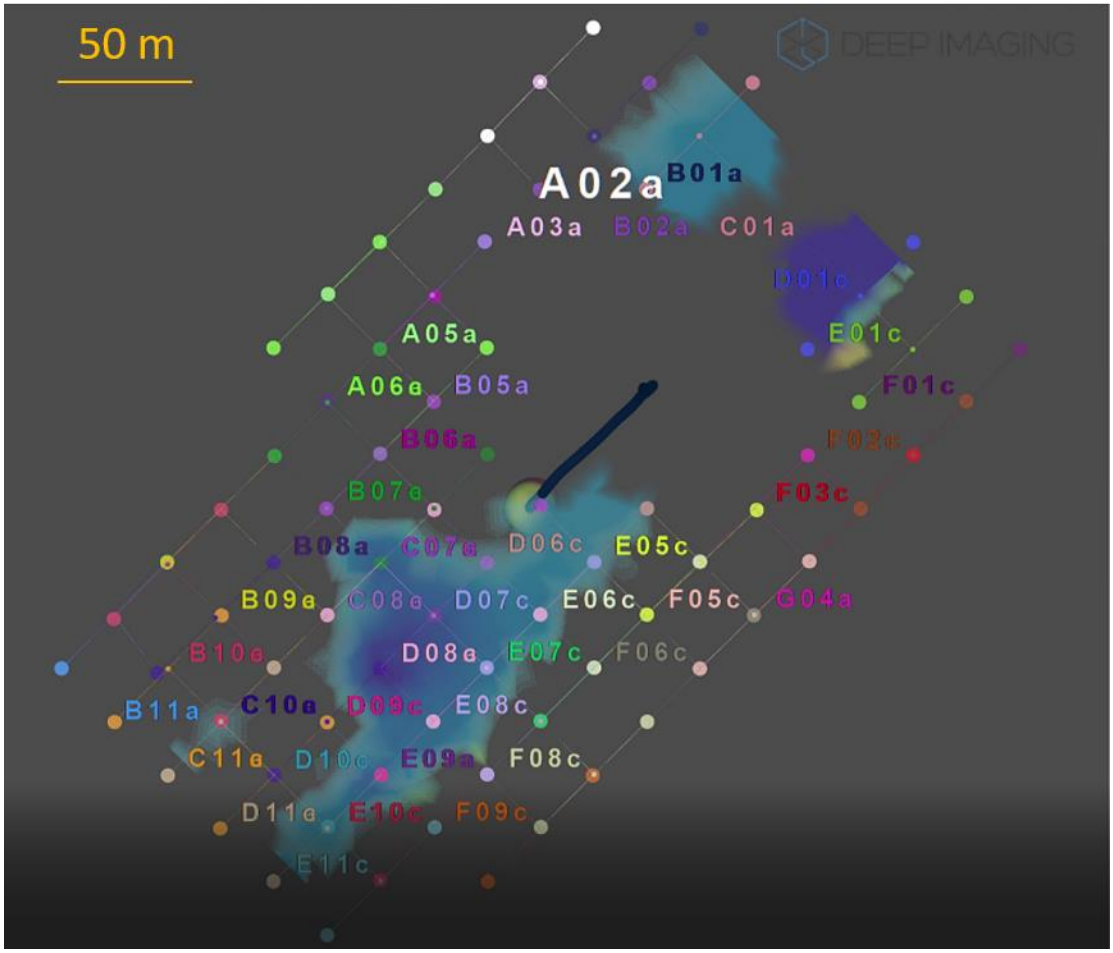

Figure V-16 Plan view of stage 2 relative change in signal at the end of the stage. Blue represents signal change from background. Modified with permission from Hickey et al. (2017).

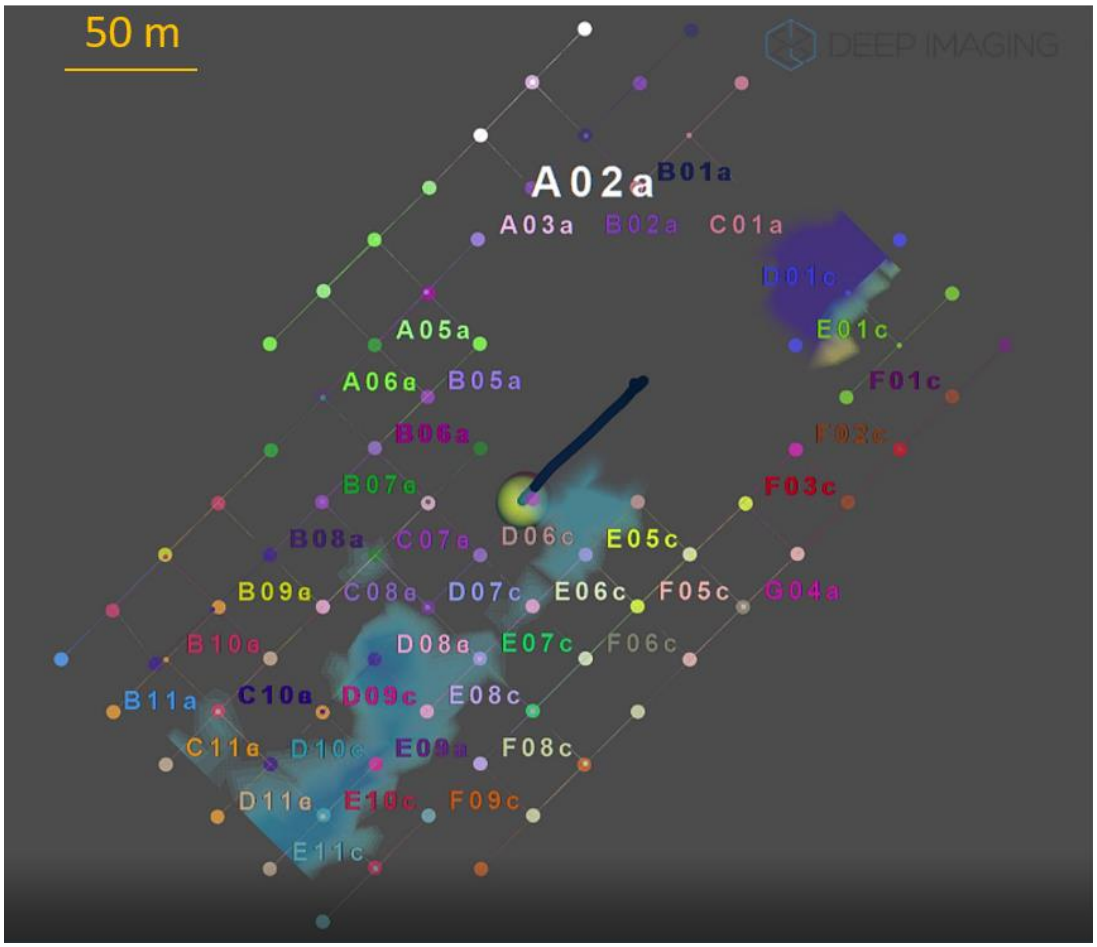

Figure V-17 Plan view of stage 2 relative change in signal at the end of the stage after pumps are turned off. Blue represents signal change from background. Modified with permission from Hickey et al. (2017).

Conclusions

In this paper two case studies are presented that display the potential effectiveness of a CSEM land-based geophysical system when it is used for hydraulic fracture monitoring. A key assumption is made that the observed temporal changes in the CSEM response are caused solely by corresponding changes in subsurface electrical conductivity induced by the movement of conductive fracture fluid. Future work aims to

rigorously test this assumption. In the first case study involving a horizontal wellbore, under this assumption, the CSEM monitoring indicated frac fluid movement, fracture extent and asymmetry, as well as the azimuth of the principal fluid pathways. These properties can enhance future decision-making by the well development team such as well-spacing and repeat fracturing. The second case study, involving a vertical wellbore, introduced new challenges such as environmental electromagnetic noise from the pad-site oilfield activities. Nevertheless, an indication of frac fluid movement, its extent, as well as the quality of proppant placement, were attained. Future modifications to the system to mitigate pad noise will be investigated. For both case studies, the potential of a CSEM land-based geophysical system to monitor the movement of hydraulic fracture fluid were investigated.

CHAPTER VI

CONCLUSIONS

Problem

In the oil and gas industry, hydraulic fracturing operations have experienced highs and lows over the past decade. When oil prices were at a maximum in early 2014, there was little concern about being efficient or cost saving. After prices crashed later that year, those that remained subscribed to a new philosophy of efficiency and optimization. Operators recognize the need to optimize the amount of oil and gas they produce at minimum effort since oil is a commodity and price fluctuations are not related to the quality of the product. This creates a highly competitive industry. Well spacing, stage spacing, pump times and amount of proppant are the major parameters that affect the bottom line of completion operations. Currently, hydraulic fracturing operations follow plans that are designed by completion engineers months before the operation starts. Engineers use modeling software and geologic parameters provided geologists and geophysicists in order to design the best frac plan. The results of their work aren't realized for months or years after a well is completed since production data can't be generated until a significant amount of time has passed. Adding more information about the results of current hydraulic fracturing operations will help refine models which can be used to optimize future projects.

Information about the location of the hydraulic fracturing fluid at depth during a completion operation addresses many of the issues mentioned in the previous paragraph.

For example, being able to answer the question “Where does the fluid go?” helps operators to optimize parameters such as stage spacing, well spacing, and pump times. Visualizations of the fluid at depth can reveal faulty cement jobs or diagnose failure of plugs. In order to monitor hydraulic fracturing fluid at depth, a technique is required that is sensitive to spatial contrasts in electrical conductivity.

Approach

Controlled source electromagnetics (CSEM) is a geophysical method that is well suited to addressing questions and problems associated with optimization of hydraulic fracturing operations. Other methods such as microseismic and distributed acoustic sensing (DAS) provide much useful information but have difficulty measuring fluid content. New equipment must be developed that improves upon existing technologies. Newly available CSEM equipment, for example, allows 50000 samples per second and nanosecond timing of the surface response across the entire oilfield. The sensitivity of new CSEM systems is on the order of 1 x 10-16 V/Am^2.

An appropriate source must be used in order to maximize the CSEM response measured at the surface due to temporal changes of the spatial distribution of electrical conductivity at depth induced by hydraulic fracture operations. Since a more conductive target, relative to the background geological formation prior to operations, is expected after the injection of fluid, a suitable layout is a grounded dipole source deployed on the surface directly above, and in alignment with, the lateral well, with receivers arrayed in predominantly broadside configuration. The grounded dipole is located directly above

the lateral to limit the effect of geometric spreading of the response arising from the subsurface. This geometry has an added benefit of maximizing the coupling of the primary field to the well casing. A strongly-coupled well casing acts as a secondary source and increases the response measured at the surface by up to two orders of magnitude.

A complete description of the source comprises the location of the wire and grounding points, and the signal that is transmitted. Since the hydraulic fracturing fluid is injected at known depth and time, the frequency content of the spectral response should change over time in a roughly predictable fashion. The grounded dipole source should transmit over a broad range of the relevant frequencies. An impulse is the ideal broadband signal, but power dispersion at depth limits the achievable signal-to-noise ratio. Initially a square wave signal was considered, but the protocol quickly changed to a pseudo-random binary (PRN) coded signal, on the advice of Dr. Robert Payton. The PRN sequence allows for controlled transmission of a broadband signal with most of the power concentrated in a discrete set of desirable low frequencies. The PRN transmission also enables small frequency steps, such as 1/64 Hz.

In order to obtain sufficient signal strength at depth such that it can efficiently couple with the well casing, a strong transmitting current must be supplied. The CSEM equipment is laid out off the pad, i,e, the grounded dipole source and the receiver boxes are deployed in the surrounding terrain, generally naturally vegetated areas, pastures and agricultural fields. It is both desired and oftentimes strictly required that the deployment and retrieval of equipment leave no trace. Accordingly, individual grounding rods are

used that are portable enough that they can be manually transported without the necessity of using a large vehicle. Each grounding rod is either 2.4 m or 1.2 m long depending on the surficial geology. The separation between each grounding rod is one rod length. All rods deployed on one end of the dipole source are connected to each other through a special cable that then connects to the single transmitter cable. The number of rods on each end, plus the surficial geology, soil moisture content, along with the transmitter voltage, determine the amplitude of the source current that should be used. Enough rods should be used such that their heat dissipation will be spread over a sufficiently wide area that the moisture content of the soil remains constant. If soil moisture decreases through excessive heating of the ground through the rods, the transmitted source current will decrease, thereby limiting signal penetration.

Configuration of the receivers should also be optimized to best resolve the expected target. The receiver boxes are independent of each other and can be deployed at any location. They record time series of electric field using grounded dipoles. Two 60-m grounded dipoles are connected to each recording box. One dipole is aligned parallel to the transmitter dipole while the other is aligned perpendicular. This arrangement allows recording of two orthogonal horizontal components of electric field.

Due to the conductivity contrast relative to the host formation of the injected fluid that is being monitored using the CSEM technique, it is hoped that the recorded signal at the surface would change over time during the hydraulic fluid injection procedure. A simple data processing workflow is desired. The signals from the transmitter and the receivers are isolated to the time interval of the duration of the

hydraulic fracturing stage that is being monitored. A discrete short-time Fourier transform (DFT) is applied to both signals, with the window defined as the length of the chosen PRN code. The receiver spectral response is divided by the transmitter signal spectrum in order to normalize any variability in the transmitter current. An initial time t_0 is defined for each receiver channel. The change in signal amplitude and phase at each frequency is determined as a function of time t-t_0. The discrete signal amplitudes across the frequency band are summed to increase the SNR. This is possible since the discrete Fourier transform of a PRN signal is a discrete comb of impulse functions of roughly equal amplitudes, with the impulses equally spaced in the frequency domain.

The first field experiment is the monitoring of a single hydraulic fracturing stage in the Eagle Ford shale play of South Texas. Based on previous studies, it was anticipated that the surface CSEM response would be most informative in the far field, so 8 receivers were deployed out to a maximum of 1600 m range from the transmitter while 2 receivers were deployed within 100 m of the stage location at depth projected to the surface. After processing the recorded data, it was found that only the receivers located next to the stage location sensed a measurable change in signal and moreover, only for the time interval that the stage was being completed. The rest of the survey layout designs at this location placed all the receivers within 500 m of the transmitter.

The LandCSEM finite element code developed at Texas A&M University is well-suited for calculating CSEM responses from a complex geology characterized by time-varying conductivity at depth. The unstructured mesh allows for modeling a well casing. To accurately represent the equipment layouts used in the field, the analytic

solution for a grounded dipole source is derived and imported into the LandCSEM code. Due to large differences in length scale and contrasts in conductivity between the casing and the host geological formations, the number of nodes in the mesh, and thereby the computational cost of solving the finite element equations, must be large. The linear system solver at the heart of the finite element analysis must be parallelized in order to speed up operations so that computations of realistic CSEM responses become practical. The parallel direct solver Pardiso was chosen for this task. Since the solver is a direct one, as opposed to an iterative one, it requires memory proportional to the number of nodes. To help with the computational burden, cloud computing is used. Amazon Web Services allows one to access multiple servers that have the necessary memory and CPU resources and then turn them off when they are no longer needed. The time to compute realistic CSEM responses at multiple frequencies is reduced from days to hours with the use of cloud computing.

Results

As mentioned before, the initial field results showed CSEM response changes only close to the location of the hydraulic fracture stage and only during times of pumping. After moving all receiver stations to the stage area, subsequent field results showed the same phenomenon. The diagnostic signal initiates at the stage location and then expands outward. Very few of the operations that have been so far imaged show the classic symmetric bi-wing fracture. Also, at the end of the frac stage, after the pumps are turned off, a relaxation of signal is observed on some operations. This is interpreted to be

caused by poor proppant placement. In particular, the relaxation is thought to be due to fluid moving out of newly-invaded areas as the fractures close up.

To help with the interpretation of surface-based CSEM responses, the LandCSEM code was updated by incorporating the solution for a grounded dipole as the primary field. This was done with the assistance of Dr. Santiago Treviño III. Under my guidance, Dr. Treviño derived the general solution for the grounded dipole source from Ward & Hohmann and programmed it into the LandCSEM finite element code. Initial modeling results showed large affected areas at the surface caused by conductivity changes at depth. The modeling results did not indicate a spatial localization of anomalous responses, as observed in field data; however, the modeling accuracy is limited by mesh resolution, node count and computational costs. The modeling results do show that when the fluid-filled slab at depth expands outward from the lateral well, the secondary response at the surface moves in the same direction. The modeling also shows that the anomalous response at some frequencies is stronger than at other frequencies. The same ideal frequency bands are also observed in the field results. Further investigation using modeling shows that the most responsive frequency band depends on the depth of the well casing and, to a lesser extent, on the surrounding geology. It is clear that further development of numerical simulations is required to adequately model CSEM responses in the complex oilfield environment.

In theory, the grounded dipole source on the surface generates a signal that interacts with the subsurface infrastructure and the surrounding geology. The secondary field due to induction of electric currents in the well casing is perturbed in the presence

of fluid-filled fracture networks. Electric currents circulating in these networks generates an anomalous response that may be observed at the surface by a sufficiently sensitive system at sufficiently low noise levels. The bulk conductivity change of the rock volume following hydraulic injection amounts to <1%, which cannot account for typical signal changes observed at the surface by practical systems. Presumably, the electric current circulating in closed pathways within the fluid-filled fracture networks generates a signal that is much greater. This hypothesis requires further testing by numerical simulations.

Impact

The application of terrestrial CSEM to hydraulic fracture monitoring provides new technology for unconventional resource development. The method, if proven successful, may allow analysts to detect fluid pathways during and after an injection. This work shows that terrestrial CSEM geophysics is not limited to large transmitter-receiver offsets, such as controlled-source magnetotellurics (CSMT), or near-surface studies using portable systems, such as time-domain electromagnetics (TDEM). There is important information in data gathered in the near vicinity of a long-grounded transmitter. If the fluid pathways could be mapped during an operation, operators can make decisions that could potentially provide large cost savings. Time-lapse images that show the migration of fluid at depth due to hydraulic fracturing would provide a new set of data for understanding coupled geomechanical/fluid-flow processes at depth. The response of fluids to a stress field is difficult to model, particularly how fluid injection

changes the stress field in previous stages and how the latter may change the fluid migration of subsequent stages. This is a direction of future research.

Imaging fluid pathways at depth would open new avenues in oilfield technology. Information from CSEM modeling helps to illuminate previously unknown or poorly understood pathways. The CSEM technology remains under continuous improvement. Just as marine CSEM has helped fill in the structure created by 3D seismic, CSEM for hydraulic fracture monitoring complements acoustic measurements such as microseismic and distributed acoustic sensing (DAS).

Future Work

One of the main directions of future work is toward 3D inversion. A three-dimensional inversion, for example using a non-linear conjugate gradient algorithm, would provide a detailed search of model space that could reveal more information about the 3D volume affected by the fluid injection than can be obtained by forward modeling alone. Such a 3D volume, if it could be identified, can be interpreted as the connected fluid flow paths, also known as the effective reservoir volume (ERV). This value is more important to engineers than the stimulated rock volume (SRV) since ERV is the volume that is directly contributing to production. The SRV could include fracturing or stress-effected volumes that do not have connections to high permeability paths.

Another future direction of research is toward real time processing and imaging. Assuming that the field installation allows for data streaming to a central location, data can be automatically processed and imaged using a combination of machine learning and model parameters previously determined by forward modeling and/or inversion. This

will allow operators to gather feedback and make decisions in real time that will save costs and time.

Adapting the mesh generation capacity and formulation of the forward modeling algorithm to include more realistic well casing geometries, at reasonable computational cost, would be a major advancement. This can be done using 1D and 2D finite-element basis functions, rather than 3D basis functions, to represent slender, highly-conductive 3D structures such as steel-cased wellbores. Currently, millions of nodes are required to model multiple wells and fracture stages using 3D finite elements, reducing the discretization of the slender structure by one dimension would only require tens of thousands of nodes. This technique can also be used to represent individual fractures, thereby computing more efficiently the secondary response they generate.

Forward modeling can also be used to determine optimal receiver placement or transmitter design. By replacing the source type that specifies the primary field in the finite element program, or by simply specifying combinations of grounded dipole sources, an optimal layout can be determined. Such layouts should be designed so that they lead to lower logistic costs and better signal to noise ratios.

Since the forward modeling shows less spatial localization of anomalous signals than does the field data, the level of detail in the forward simulations needs to be increased and the noise needs to be much better understood. The EM coupling between the wellbore and the fluid-filled fracture network is also poorly understood since the geometry of the latter is largely unknown.

In summary, I have explored in this dissertation the potential for terrestrial CSEM to become a viable tool for hydraulic fracture monitoring of unconventional reservoirs. I have made some interpretations of fracture imaging from time-lapse observations of CSEM responses in several case studies using recently developed technology. The interpretations are only tentative since they require much additional support from improvements in modeling and noise characterization. The complexities of the oilfield working environment, and the subtlety of the anticipated signals arising from poorly understood coupled fluid-geomechanical processes occurring within the subsurface at depth will always present extreme challenges for robust and definitive interpretation of controlled-source electromagnetic geophysical data.

REFERENCES

Avdeev, D. B. (2005). Three-dimensional electromagnetic modelling and inversion from theory to application. *Surveys in Geophysics, 26*(6), 767-799.

Badea, E. A., Everett, M. E., Newman, G. A., & Biro, O. (2001). Finite-element analysis of controlled-source electromagnetic induction using Coulomb-gauged potentials. *Geophysics, 66*(3), 786-799.

Chave, A. D. (2009). On the electromagnetic fields produced by marine frequency domain controlled sources. *Geophysical Journal International, 179*(3), 1429-1457.

Constable, C. (2016). Earth's electromagnetic environment. *Surveys in Geophysics, 37*(1), 27-45.

Constable, S., & Srnka, L. J. (2007). An introduction to marine controlled-source electromagnetic methods for hydrocarbon exploration. *Geophysics, 72*(2), WA3-WA12.

Duncan, P. M., Hwang, A., Edwards, R. N., Bailey, R. C., & Garland, G. D. (1980). The development and applications of a wide band electromagnetic sounding system using a pseudo-noise source. *Geophysics, 45*(8), 1276-1296.

Edwards, N. (2005). Marine Controlled Source Electromagnetics: Principles, Methodologies, Future Commercial Applications. *Surveys in Geophysics, 26*(6), 675-700.

Everett, M. E. (2005). What do electromagnetic induction responses measure? *The Leading Edge, 24*(2), 154-157.

Everett, M. E., & Meju, M. A. (2005). Near-surface controlled-source electromagnetic induction; background and recent advances. *Hydrogeophysics, 50*, :. (Series) http://www.springer.com/sgw/cda/frontpage/0,11855,4-40515-69-33112474-0,00.html

Fisher, M. K., & Warpinski, N. R. (2012). Hydraulic-fracture-height growth: Real data. *SPE Production & Operations, 27*(01), 8-19.

Freund, R. W., Golub, G. H., & Nachtigal, N. M. (1992). Iterative solution of linear systems. *Acta numerica, 1*, 57-100.

Griffiths, D. J. (1999). Introduction to electrodynamics. Upper Saddle River, N.J.: Prentice Hall.

Haber, E., Ascher, U., Oldenburg, D. W., Shekhtman, R., & Chen, J. (2002). 3-D frequency-domain CSEM inversion using unconstrained optimization. In *SEG Technical Program Expanded Abstracts 2002* (pp. 653-656): Society of Exploration Geophysicists.

Hickey, M. S., Everett, M. E., Helwig, S. L., & Mogilatov, V. S. (2010). The effects of rough terrain on land-based controlled-source electromagnetic exploration using a long horizontal dipole source. In *SEG Technical Program Expanded Abstracts 2010* (pp. 3914-3918): Society of Exploration Geophysicists.

Hickey, M. S., Treviño, S., & Everett, M. (2015). *Monitoring and Imaging the Dynamics and Extent of Hydraulic Fracturing Fluid Movement Using Ground-Based Electromagnetics, With Application to the Eagle Ford Shale*. Paper presented at the Proceedings of the 3rd Unconventional Resources Technology Conference.

Hickey, M. S., Trevino, S., & Everett, M. E. (2017). *Monitoring Hydraulic Fracturing Fluid Movement Using Ground-Based Controlled-Source Electromagnetics (CSEM), With Applications to the Anadarko Basin and the Delaware Basin NW Shelf*. Paper presented at the Proceedings of the 5th Unconventional Resources Technology Conference.

Hickey, M. S., Treviño III, S., & Everett, M. E. (2015). *Monitoring and Imaging the Dynamics and Extent of Hydraulic Fracturing Fluid Movement Using Ground-Based Electromagnetics, with Application to the Eagle Ford Shale.* Paper presented at the Unconventional Resources Technology Conference, San Antonio, Texas, 20-22 July 2015.

Hickey, M. S., Treviño, S., & Everett, M. E. (2015). *Detection and Characterization of the Injection of Hydraulic Fracturing Fluid using Ground-Based Controlled-Source Electromagnetics*. Paper presented at the SEG Technical Program Expanded Abstracts 2015.

Hoversten, G. M., Commer, M., Haber, E., & Schwarzbach, C. (2015). Hydro-frac monitoring using ground time-domain electromagnetics. Geophysical Prospecting, 63(6), 1508-1526.

Jackson, J. D. (1999). Classical electrodynamics. New York: Wiley.

Key, K., & Weiss, C. (2006). Adaptive finite-element modeling using unstructured grids: The 2D magnetotelluric example. *Geophysics*, *71*(6), G291-G299.

Lake, L. W., Fanchi, J. R., Arnold, K., Clegg, J. D., Holstein, E. D., & Warner, H. R. (2007). *Petroleum Engineering Handbook: Reservoir Engineering and Petrophysics* (Vol. 5): Society of Petroleum Engineers.

Maaø, F. A., & Nguyen, A. K. (2010). Enhanced subsurface response for marine CSEM surveying. *Geophysics, 75*(3), A7-A10.

Mackie, R. L., Bennett, B., & Madden, T. R. (1988). Long-period magnetotelluric measurements near the central California coast: a land-locked view of the conductivity structure under the Pacific Ocean. *Geophysical Journal International, 95*(1), 181-194.

Miensopust, M. P. (2017). Application of 3-D Electromagnetic Inversion in Practice: Challenges, Pitfalls and Solution Approaches. *Surveys in Geophysics, 38*(5), 869-933.

Montgomery, C. T., & Smith, M. B. (2010). Hydraulic fracturing: history of an enduring technology. *Journal of Petroleum Technology, 62*(12), 26-40.

Nabighian, M. N. (1988). *Electromagnetic methods in applied geophysics*. Tulsa, Okla.: Society of Exploration Geophysics.

Newman, G. A. (2014). A review of high-performance computational strategies for modeling and imaging of electromagnetic induction data. *Surveys in Geophysics, 35*(1), 85-100.

Pankratov, O. V., & Geraskin, A. I. (2010). On processing of controlled source electromagnetic (CSEM) data. *Geologica acta, 8*(1), 31-49.

Passalacqua, H. (1983). Electromagnetic fields due to a thin resistive layer. *Geophysical Prospecting, 31*(6), 945-976.

Patzer, C., Tietze, K., & Ritter, O. (2017). Steel-cased wells in 3-D controlled source EM modelling. *Geophysical Journal International, 209*(2), 813-826.

Puzyrev, V., Vilamajo, E., Queralt, P., Ledo, J., & Marcuello, A. (2017). Three-dimensional modeling of the casing effect in onshore controlled-source electromagnetic surveys. *Surveys in Geophysics, 38*(2), 527-545.

Sasaki, Y., & Meju, M. A. (2006). A multidimensional horizontal-loop controlled-source electromagnetic inversion method and its use to characterize heterogeneity in aquiferous fractured crystalline rocks. *Geophysical Journal International, 166*(1), 59-66.

Schenk, O., & Gärtner, K. (2004). Solving unsymmetric sparse systems of linear equations with PARDISO. *Future Generation Computer Systems, 20*(3), 475-487.

Sinha, A. K. (1968). Electromagnetic fields of an oscillating magnetic dipole over an anisotropic earth. *Geophysics, 33*(2), 346-353.

Stalnaker, J. L., Everett, M. E., Benavides, A., & Pierce, C. J. (2006). Mutual induction and the effect of host conductivity on the EM induction response of buried plate targets using 3-D finite-element analysis. *IEEE Transactions on Geoscience and Remote Sensing, 44*(2), 251-259.

Streich, R. (2016). Controlled-source electromagnetic approaches for hydrocarbon exploration and monitoring on land. *Surveys in Geophysics, 37*(1), 47-80.

Tabbara, M., Blacker, T., & Belytschko, T. (1994). Finite element derivative recovery by moving least square interpolants. *Computer Methods in Applied Mechanics and Engineering, 117*(1-2), 211-223.

Thiel, S. (2017). Electromagnetic monitoring of hydraulic fracturing: Relationship to permeability, seismicity, and stress. *Surveys in Geophysics, 38*(5), 1133-1169.

Tietze, K., Ritter, O., Patzer, C., Veeken, P., & Dillen, M. (2019). Repeatability of land-based controlled-source electromagnetic measurements in industrialised areas and including vertical electric fields. *Geophysical Journal International*. https://doi.org/10.1093/gji/ggz225

Um, E. S., Commer, M., Newman, G. A., & Hoversten, G. M. (2015). Finite element modelling of transient electromagnetic fields near steel-cased wells. Geophysical Journal International, 202(2), 901-913.

Ward, S. H., & Hohmann, G. W. (1988). Electromagnetic theory for geophysical applications. In *Electromagnetic Methods in Applied Geophysics: Voume 1, Theory* (pp. 130-311): Society of Exploration Geophysicists.

Wirianto, M., Mulder, W. A., & Slob, E. C. (2011). Exploiting the airwave for time-lapse reservoir monitoring with CSEM on land. *Geophysics, 76*(3), A15-A19.

Ziolkowski, A., Wright, D., & Mattsson, J. (2011). Comparison of pseudo-random binary sequence and square-wave transient controlled-source electromagnetic data over the Peon gas discovery, Norway. *Geophysical Prospecting, 59*(6), 1114-1131.

APPENDIX A

PSEUDO-RANDOM BINARY SEQUENCES

The depth of penetration and the secondary response due to excitation of the subsurface by an electromagnetic source depends on the frequency of the transmitted current waveform. A wide band of frequencies provides information about a range of depths. There are multiple approaches to generate multi-frequency, or broadband, source waveforms. Some of these approaches include frequency sweeping, square wave transmission, and impulse transmission. Another method involves transmission of a pseudo-random binary sequence (PRBS) (Duncan et al., 1980; Ziolkowski et al., 2011). A PRBS is a binary time sequence generated by a deterministic algorithm that exhibits statistical behavior similar to a truly random sequence. PRBS geophysical applications involve the use of spectral analysis to produce a broadband frequency spectrum that is characterized by a nearly-constant amplitude at each frequency inside the band. A PRBS time sequence can be tuned to increase the frequency density at lower frequencies during deep exploration, or to extend the frequency content to higher frequencies for shallow exploration.

A PRBS is a time sequence of N binary samples where the base-2 exponent n (see equation 1, below) defines the order of the sequence. The sample values alternate between two levels, for example -1 and 1, at pseudo-random multiples of a basic time interval Δt. In order to obtain the entire source spectrum without aliasing, the sampling rate of recorded data must be greater than or equal to $1/\Delta t$ (Ziolkowski et al., 2011).

Two parameters are important in applications of PRBS to geophysical exploration: the time interval Δt, and the number of samples, N. These parameters determine the required clock frequency f_c of an acquisition system. The Fourier transform (FT) of a PRBS has the property that a first zero, or null, in the amplitude spectrum occurs at f_c, as given by equation (2) below. The amplitude thereafter follows a $\text{sinc}^2(f)$ function. Since the first null in the frequency domain is at the "critical frequency" f_c, the frequency band of exploration should be constrained to lower frequencies $f < f_c$. The number of samples N determines how much information, in bits, is contained within the PRBS time sequence. The more information the PRBS contains, the more frequency steps can be extracted from the amplitude spectrum.

$$N = 2^n - 1 \quad (1)$$

$$f_c = \frac{N}{\Delta t} \quad (2)$$

Advancements in electronic timing precision allows for geophysical sources to use larger time intervals Δt while maintaining high accuracy. Faster electronic switching of the source at high currents and voltage allows geophysicists to increase the number of samples, and concomitantly the amount of information contained in the signal, in a given amount of time. These advancements allow for a longer-time, highly-accurate PRBS that is characterized by a large number of samples. A subsample of a 64-second, 8191-bit PRBS is shown in figure 1. Its corresponding Fourier amplitude spectrum is shown in figure 2. Notice that the amplitude spectrum is relatively flat at low frequencies, before falling off rapidly at the critical frequency f_c.

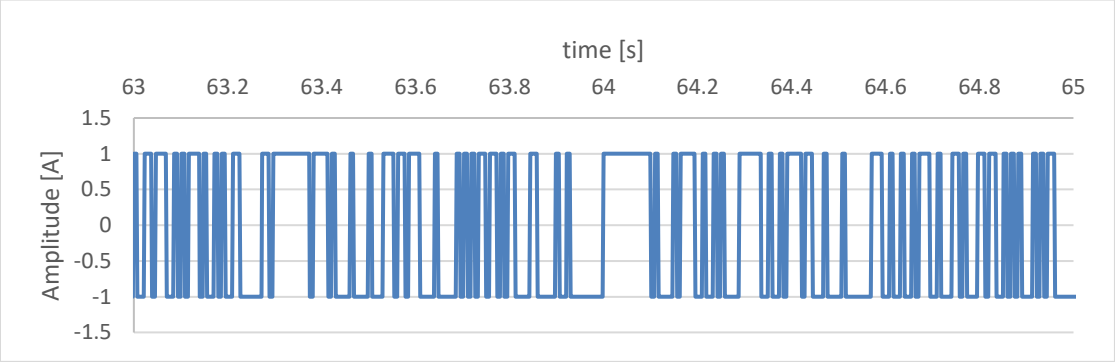

Figure A-1 A 2-s-long subsample of a $\Delta t = 64$ second, N = 8191 bit PRBS code. The min and max values of the binary sequence are -1 and 1, respectively.

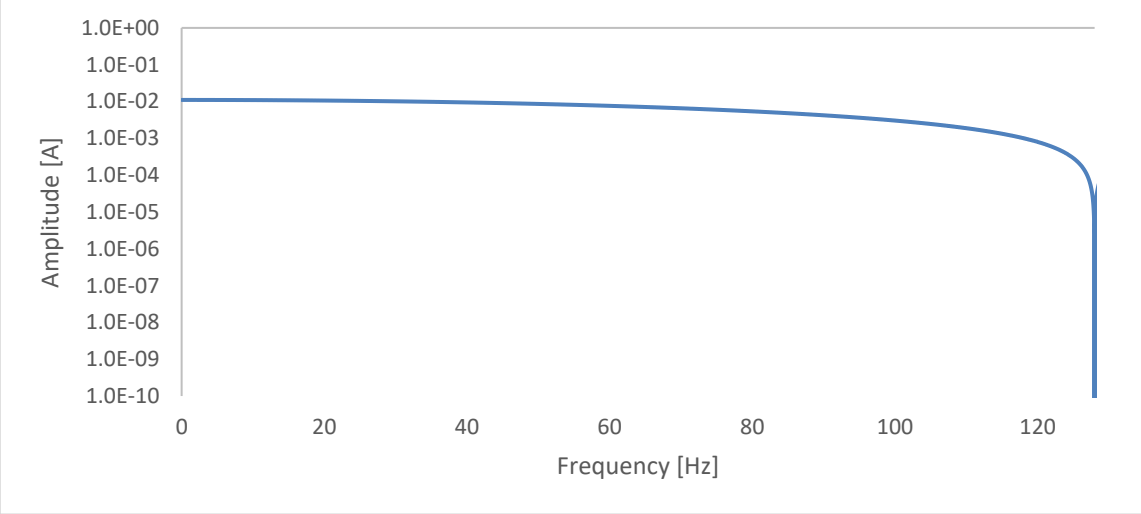

Figure A-2 Frequency spectrum of the PRBS code shown in the previous figure 1.

In order to extract the complete frequency content of a PRBS, one must take a Fourier transform of the entire sequence. Only a 2-s-long code subsample is shown in figure 1. The shown sequence has a cutoff frequency f_c =127.98 Hz. The frequency band used for exploration and interpretation should be kept below f_c, due to the amplitude drop-off at higher frequencies. Since the grounded-dipole system used to transmit the

signal also generates direct and inductive couplings to the earth, the actual transmitted signal is not a “pure” PRBS. Instead, a typical signal transmitted by a practical source, along with its amplitude spectrum, is shown in figure 2. This signal may be recorded by placing a Hall probe sensor on the transmitter line.

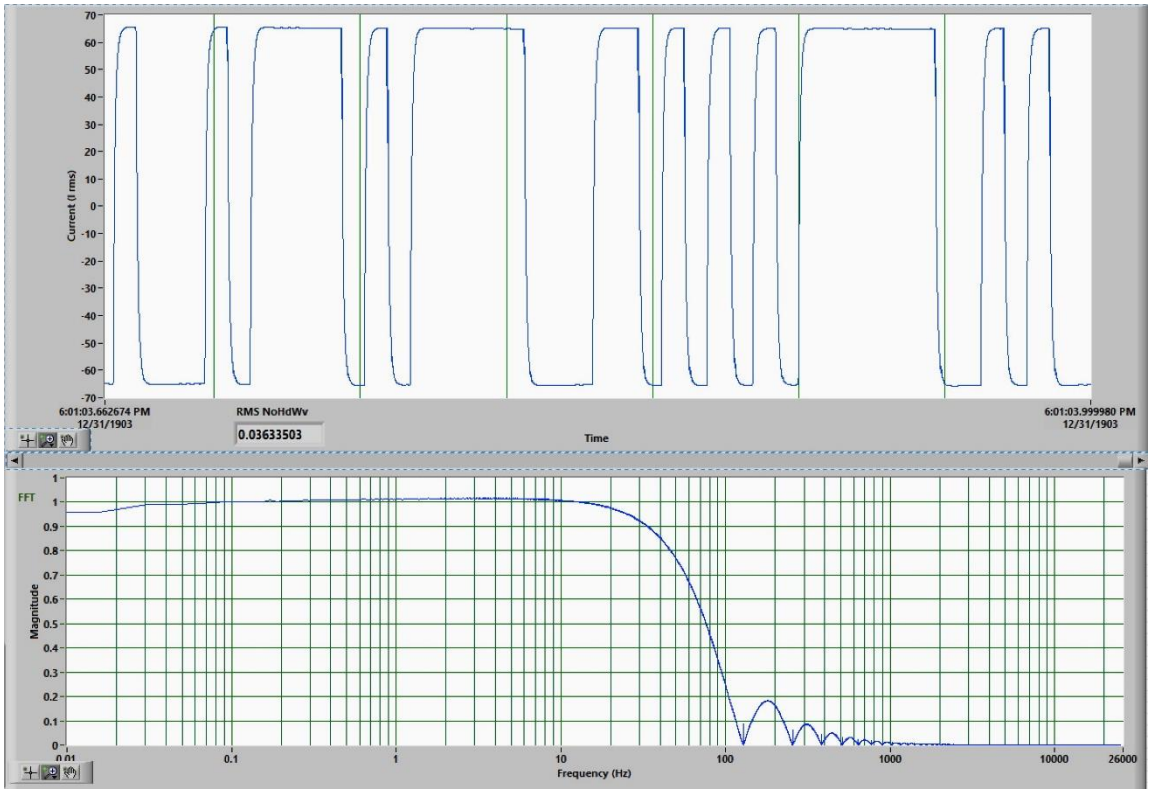

Figure A-3 Top: Sample of a time-domain recording of a 64 s PRBS signal. Bottom: Spectral amplitude plot of the signal**.**

APPENDIX B

HYDRAULIC FRACTURE HALF-LENGTH

During a hydraulic fracture operation, operators attempt to create a multitude of interconnected fluid pathways within a rock volume around the lateral wellbore. The success of a fracture operation depends on the generation of interconnectivity of fractures within this volume. However, metrics used for success or failure of an operation are sometimes poorly defined. One such metric is *fracture half-length*, i.e. the distance that the fracture network extends from the perforations of the lateral wellbore. The fracture half-length metric is supposed to represent the characteristic scale length of the entire network of fractures; it is not indicative of the length of any individual fracture within the network.

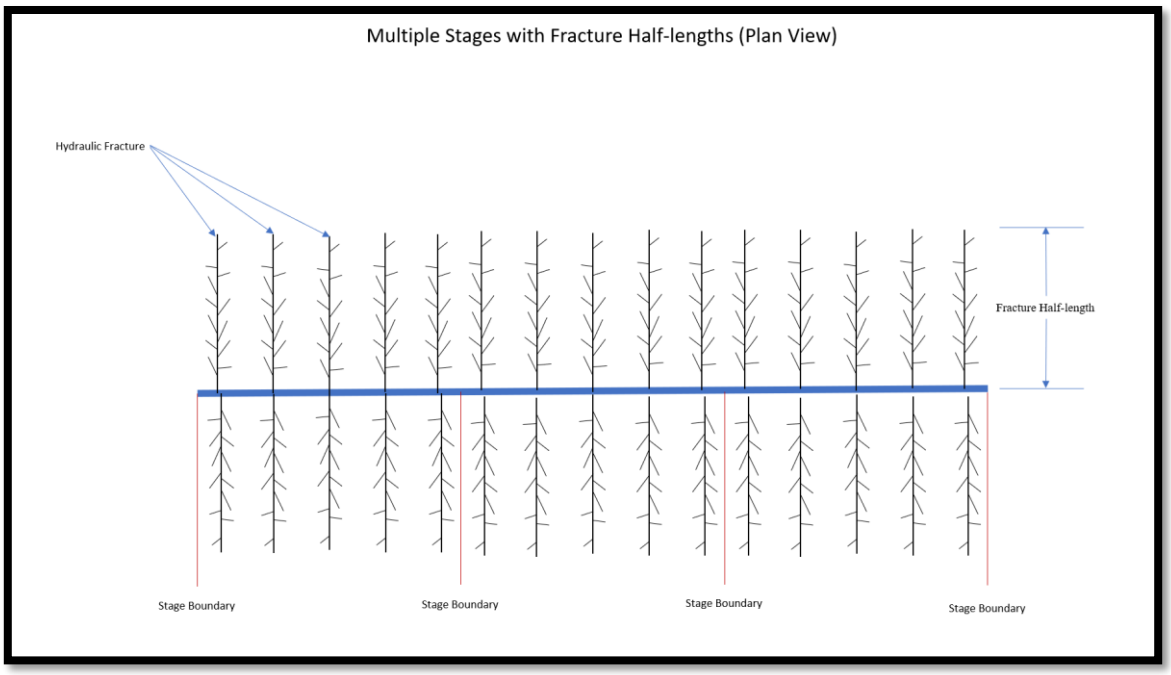

Figure B-4 Plan view of lateral wellbore (in blue) showing multiple stages (sections of wellbore between stage boundaries) with fracture networks originating from perf clusters at the wellbore**.**

The hydraulic fracture network originates from holes perforated into the steel casing. Groups of such holes are referred to as "perf clusters". Operators pump fluid out of a section of the lateral wellbore that contains one or more perf clusters. Each of the sections that are subjected to pumping is referred to as a stage. A plan view representation of fracture networks emanating from perf clusters associated with a contiguous series of stages on a lateral wellbore is shown in figure 1.

CSEM monitoring records the response to electromagnetic induction within the geological formation, wellbore, and fluid at depth. The diffusion of the signal generated

at wellbore depth to the surface is inherently a smoothing process, with Earth acting as a low-pass filter. Thus, the recorded voltage due to an enhancement of the conductivity of an individual fluid-filled fracture is not detectable. However, the response of a network of fractures, like those shown in figures 2 and 3 below, could be detectable. A fracture network, to generate a CSEM response, should form closed, conductive pathways, i.e. loops (Figure 4). Since the fractures in figure 3 form closed loops, this network will most likely produce a larger inductive response compared to the fracture network in figure 1. If measurable, the CSEM response due to the fracture network could be interpreted in terms of its location and half-length.

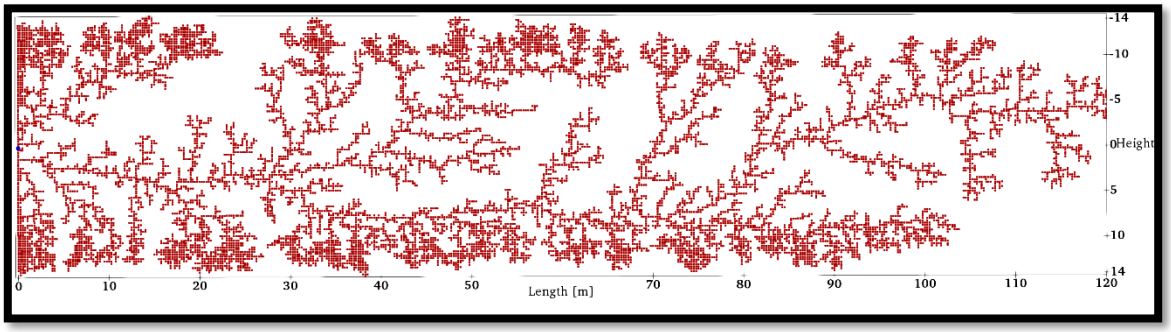

Figure B-5 Representation of a 2D slice of a 3D dendritic fracture network. This network was generated with a damped random walk algorithm

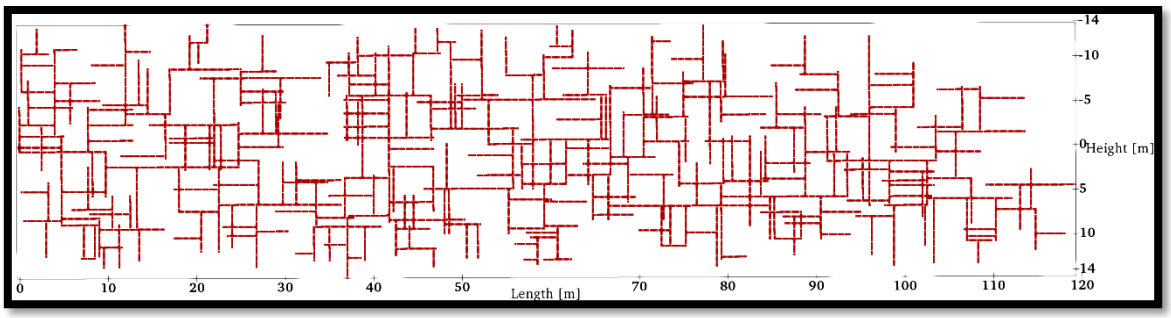

Figure B-6 Representation of a 2D slice of a 3D orthogonal fracture network based on Fisher (2012). This network was generated with a constrained random walk algorithm

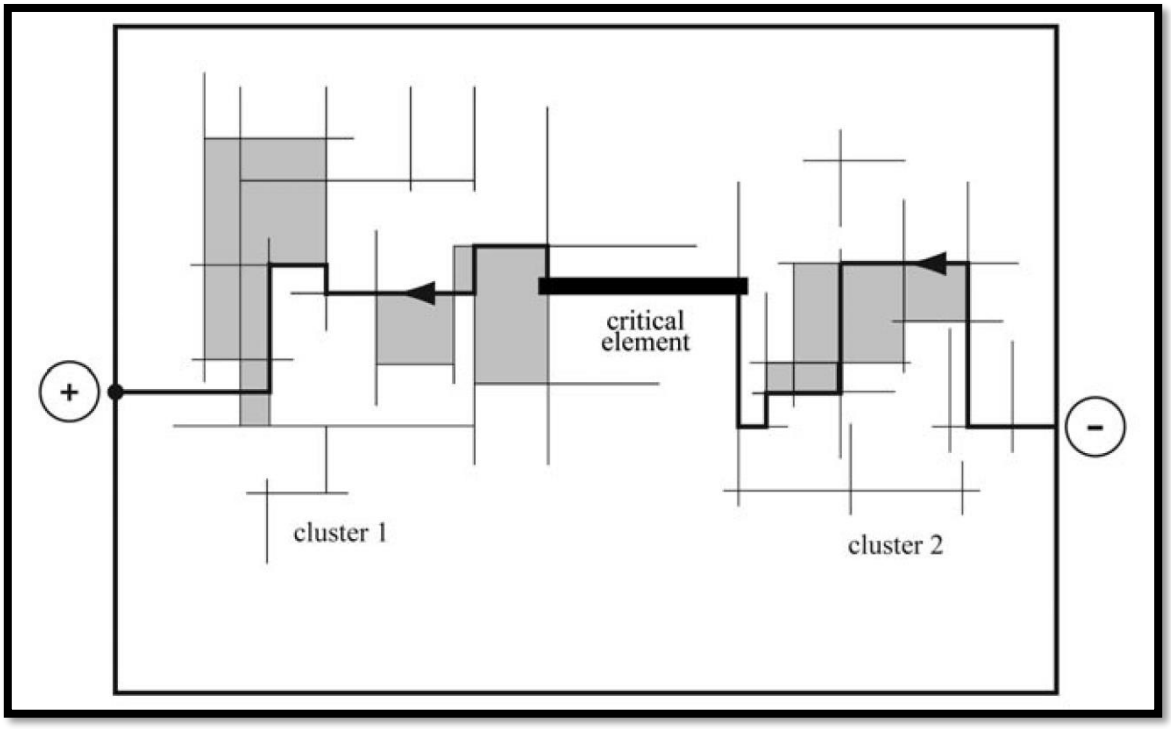

Figure B-7 Inductive response comes from closed loops formed by interconnected fractures, not from the requirement of a through-going percolation path. Thus, the presence of the connection marked "critical element" has little effect on the inductive response. Reprinted with permission from Everett (2005).

APPENDIX C

MITIGATION OF AMBIENT EM NOISE IN LAND-BASED OILFIELD OPERATIONS

A CSEM survey is highly susceptible to ambient electromagnetic noise, which is largely impulsive in nature, and may be of high amplitude. This is especially the case during oil field operations due to the presence of heavy machinery and infrastructure. Ambient EM noise is difficult to assess since it is highly site specific, and also can vary from day to day. By contrast, the marine environment is electromagnetically quiet even in shallow water when compared to the terrestrial environment. Few studies have been made on noise and repeatability error in the oil field on land, whereas the number of marine noise studies is much larger (Tietze et al 2019). Ambient noise may be assigned into different categories based on the source of the noise and how it affects recorded CSEM signals. Noise mitigation, in this study, should take into account that CSEM monitoring records differences in the subsurface response over time. A windowed Fourier transform can be used on time-domain monitoring data to examine changes in frequency content of the noise spectrum over time.

A noise source may be classified as consistent background noise if its statistical properties are constant over the area and duration of a survey. An example of a source of this type is a motor that runs at a constant or near-constant speed during the entire data acquisition interval. Since CSEM monitoring data are differences in subsurface response

over time, the subtraction of a signal recorded at initial time t_0 from a response recorded at some later time $t > t_0$ should largely mitigate noise of this class.

Eddy currents induced by the transmitted primary field in steel infrastructure is a source of signal-generated noise that is always present while the transmitter is operating. This type of noise couples nonlinearly into the geological signal and cannot be filtered out of an instantaneous response. However, signal-generated noise can be largely mitigated by a subtraction of two responses recorded at different times.

Another noise type that is frequently observed during CSEM monitoring of oilfield operations can be described as a cross-field effect. Cross-field noise affects all, or most, receivers across the entire survey area. The noise may be confined to specific frequencies or frequency bands. Cross-field noise may also be evident over only a portion of the entire acquisition interval. Therefore, cross-field noise cannot be completely removed by subtraction of a response with the signal recorded at initial time t_0. The origin of this type of noise is unknown, but it may be attenuated using a statistical multi-step method, as discussed below.

Consider a dataset **d** that is measured at multiple receiver locations, across multiple frequencies *f*, and within each of several time windows each of width Δt. Moreover, suppose the frequency content of the noise is variable over time. For each receiver location and time window, normalize onto [-1,+1] the amplitude of each frequency bin. Now compare amplitudes across all locations for each time and frequency combination. For example, for time step t_n and frequency f_m, this gives k arrays of size

(number of time windows x number of frequency bins) where k is the number of receiver locations.

Localized responses at different locations are sought that exhibit the same amplitude variations over the designated time window. Detrending of the various receiver responses using a simple mean would identify similar values, but outliers due to spikes at certain receiver locations serve to bias the mean. A robust detrending algorithm using the trimmed mean (Pankratov & Geraskin, 2010) helps to alleviate the bias. Applying only a percentage of the detrended mean lowers the chance of removing signal along with the noise. The data can be subjected to this procedure multiple times since attenuating one anomaly may reveal another. However, too many passes through this algorithm could attenuate signal based on noise that is not present across the entire survey area. Caution should be used when applying this method if the noise does not span the entire survey area since noise could be introduced to receiver locations that didn't initially exhibit the cross-field effect.

Note that the cross-field filter will attenuate signals, perhaps including those of interest from the subsurface, that are in the form of a broad-scale anomaly. This filter therefore should be used only on signal that doesn't correlate in time and location with the pump data. For example, the filter could be used during times at which nothing is being changed in the subsurface. Further studies are required to fully understand the nature and origin of the cross-field effect and to better distinguish cross-field noise from broad-scale signals of interest arising from subsurface spatiotemporal variations in electrical conductivity.

Additional noise can be generated by spatially-localized broadband sources such as water pumps that produce non-stationary time-variable electromagnetic fields. Machinery of this type not only generates a 60 Hz main signal while operating, but also produces randomly occurring impulsive signals. If the noise is bursty in time, but relatively quiet conditions prevail otherwise, the affected CSEM monitoring data can be discarded. The resulting gaps, if small, may be filled by temporal interpolation. If the noise bursts are too closely spaced however, the entire signal might be badly compromised and its entirety should be discarded.

One of the most significant noise sources in the oilfield is the electromagnetic noise from powerlines. This could be a 60 Hz or 50 Hz signal, depending on geographical region, plus harmonics. Since the observed CSEM data are converted into the frequency domain, a simple noise mitigation technique for powerlines is to discard frequency components over a narrow bandwidth centered at 50/60 Hz. However, powerlines do not generate a simple spike in the noise spectrum at the powerline frequency. It is important to enhance frequency resolution so that narrowband powerline harmonics may be more clearly isolated from the rest of the spectrum. In order to obtain better frequency isolation of powerline harmonics, the time-domain data should be stacked. Stacking helps to produce a sharper peak in the noise spectrum at the powerline frequency, although the response from the subsurface targets of interest will be averaged over the number of time steps used in the stack. This might degrade the temporal resolution of the anomalous subsurface response. The concern is alleviated if the temporal change in subsurface response is longer than the averaging window.

APPENDIX D

DEVELOPMENT OF SECONDARY POTENTIAL EQUATIONS

The formulation for electromagnetic induction in the earth starts with Maxwell's equations:

$$\nabla \cdot \boldsymbol{E} = \frac{1}{\varepsilon}\rho \tag{1}$$

$$\nabla \cdot \boldsymbol{H} = 0 \tag{2}$$

$$\nabla \times \boldsymbol{E} = -\mu \frac{\delta \boldsymbol{H}}{\delta t} \tag{3}$$

$$\nabla \times \boldsymbol{H} = \boldsymbol{J} + \varepsilon \frac{\delta \boldsymbol{E}}{\delta t} \tag{4}$$

where $\boldsymbol{E}$ is the electric field, $\boldsymbol{H}$ is the magnetic field, ρ is the charge density, ε is the electric permittivity, and $\boldsymbol{J}$ is the current density. Other constraints are as follows:

$$\boldsymbol{B} = \mu \boldsymbol{H} \tag{5}$$

$$\boldsymbol{J} = \sigma \boldsymbol{E} \tag{6}$$

where $\boldsymbol{B}$ is magnetic induction, μ is magnetic permeability, and σ is electrical conductivity. More in-depth study and derivations can be found in many well-respected texts (Griffiths, 1999; Jackson, 1999). The magnetic permeability for a material is given as:

$$\mu = \mu_r \mu_0 \tag{7}$$

where μ_0 is the permeability of free space and μ_r is the relative permeability. In most geologic material, the relative permeability is close to 1; therefore, to simplify the equations, the following assumption is made:

$$\mu = \mu_0 \tag{8}$$

where $\mu_0 \approx 4\pi \times 10^{-7}$. This then gives the following:

$$\boldsymbol{B} = \mu_0 \boldsymbol{H} \tag{9}$$

Assuming a time dependence of $e^{-i\omega t}$ and substituting in equation (6) into equation (4), we can rewrite equations (3) and (4) as:

$$\nabla \times \boldsymbol{E} = i\omega\mu_0 \boldsymbol{H} \tag{10}$$

$$\nabla \times \boldsymbol{H} = \boldsymbol{J_S} + \sigma \boldsymbol{E} \tag{11}$$

Where J has divided into a known source term $\boldsymbol{J_S}$ and the ohmic conduction term $\sigma \boldsymbol{E}$ represents the induced currents in the earth. The displacement current term goes away due to a quasi-static approximation. In order to more easily solve equations (10) and

(11), we express the EM field ($\boldsymbol{E}$, $\boldsymbol{H}$) in terms of a magnetic vector potential $\boldsymbol{A}$ and an electric scalar potential φ defined by the equations:

$$\boldsymbol{B} \equiv \nabla \times \boldsymbol{A} \tag{12}$$

$$\boldsymbol{E} \equiv i\omega \boldsymbol{A} - \nabla\varphi \tag{13}$$

Writing equation (11) in terms of the EM potentials creates the curl-curl equation:

$$\nabla \times \nabla \times \boldsymbol{A} = \mu_0 \boldsymbol{J}_S + \mu_0 \sigma (i\omega \boldsymbol{A} - \nabla\varphi) \tag{14}$$

In order to help with symmetry in solving these equations, we introduce the reduced scalar potential $\varphi \equiv i\omega\psi$, and incorporate the term $-\nabla(\nabla \cdot A)$ to the left side of equation (14) resulting in

$$\nabla \times \nabla \times \boldsymbol{A} - \nabla(\nabla \cdot \boldsymbol{A}) - i\omega\mu_0\sigma(\boldsymbol{A} + \nabla\psi) = \mu_0 \boldsymbol{J}_S \tag{15}$$

We can add the term $-\nabla(\nabla \cdot A)$ because it doesn't change the equation as long as the Coloumb gauge, $\nabla \cdot \boldsymbol{A} = 0$, is satisfied

Applying the identity $\nabla \times \nabla \times \boldsymbol{A} - \nabla(\nabla \cdot \boldsymbol{A}) = -\nabla^2 \boldsymbol{A}$ to equation (15) results in

$$\nabla^2 \boldsymbol{A} + i\omega\mu_0\sigma(\boldsymbol{A} + \nabla\psi) = -\mu_0 \boldsymbol{J}_S \tag{16}$$

Equation (16) is equivalent to a vector Helmholtz equation. The auxiliary equation

$$\nabla \cdot [i\omega\mu_0\sigma(\boldsymbol{A} + \nabla\psi)] = -\mu_0\boldsymbol{J}_S \tag{17}$$

must be solved simultaneously with the Helmholtz equation. The equations for the primary field response:

$$\nabla^2\boldsymbol{A}_P + i\omega\mu_0\sigma(\boldsymbol{A}_P + \nabla\psi_P) = -\mu_0\boldsymbol{J}_S \tag{18}$$

$$\nabla \cdot [i\omega\mu_0\sigma(\boldsymbol{A}_P + \nabla\psi_P)] = \nabla \cdot [-\mu_0\boldsymbol{J}_S] \tag{19}$$

Are equal to the equations for the secondary field response:

$$\nabla^2(\boldsymbol{A}_P + \boldsymbol{A}_S) + i\omega\mu_0\sigma\big((\boldsymbol{A_P} + \boldsymbol{A_S}) + (\nabla\psi_P + \nabla\psi_S) = -\mu_0\boldsymbol{J}_S \tag{20}$$

$$\nabla \cdot [i\omega\mu_0\sigma\big((\boldsymbol{A}_P + \boldsymbol{A}_S) + (\nabla\psi_P + \nabla\psi_S)\big] = \nabla \cdot [-\mu_0\boldsymbol{J}_S]. \tag{21}$$

The known primary EM potentials ($\boldsymbol{A_P}, \psi_P$) consist of an analytical expression of the source. The secondary EM potentials are defined as $\boldsymbol{A} \equiv \boldsymbol{A}_P + \boldsymbol{A}_S$ and $\psi \equiv \psi_P + \psi_S$. $\Delta\sigma \equiv \sigma - \sigma_P$ is the conductivity difference of the total conductivity, $\sigma(\boldsymbol{r})$, and the background conductivity, $\sigma_P(\boldsymbol{r})$, used in calculating the primary field. The governing equations of the system become:

$$\boldsymbol{\nabla}^2\boldsymbol{A}_S + i\omega\mu_0\sigma(\boldsymbol{r})(\boldsymbol{A}_S + \boldsymbol{\nabla}\psi_S) = -i\omega\mu_0\Delta\sigma(\boldsymbol{A}_P + \boldsymbol{\nabla}\psi_P) = -\mu_0\Delta\sigma\boldsymbol{E}_P \tag{22}$$

$$i\omega\mu_0\boldsymbol{\nabla} \cdot [\,\sigma(\boldsymbol{r})(\boldsymbol{A}_S + \boldsymbol{\nabla}\psi_S)] = -\nabla \cdot [i\omega\mu_0\Delta\sigma(\boldsymbol{A}_P + \boldsymbol{\nabla}\psi_P)] = -\boldsymbol{\nabla} \cdot \mu_0\Delta\sigma\boldsymbol{E}_P \tag{23}$$

Having the right-hand side as the primary electric field instead of the Coulomb gauge potentials allows for easier computations. This is found by using equation (13).